Non-contrast Magnetic Resonance Angiography and Computational Fluid Dynamic Analysis of Renal Artery for Renovascular Hypertension

Weisheng Zhang
BSc (Medical Imaging and Nuclear Medicine)
MSc (Medical Imaging and Nuclear Medicine)

A thesis of The Faculty of Medicine and Health Sciences, Macquarie University, submitted in fulfilment of the requirements for the degree of Doctor of Philosophy.

Supervisor

Professor Yi Qian

Partner Supervisor (Fudan University)

Professor Jiang Lin

September 2015

MACQUARIE University
SYDNEY·AUSTRALIA

Faculty of Medicine and Health Sciences

Summary

Renovascular hypertension is caused by renal artery stenosis (RAS). The relationship among RAS, hypertension, and renal function varies from patient to patient is difficult to assess, but the severity of association increases risks for patient. An accurate, reliable and non-invasive method to evaluate severity and hemodynamics of RAS is mandatory.

MRA is a well-known method in the angiographic illustration of RAS in current clinical application. However, there exists limitation in its application, especially lack of capability in blood pressure measurement. On the other hand, the technology of patient-specific computational fluid dynamics (CFD) is another novel technology to enable quantitatively estimate vascular hemodynamics. To date, there is no report to determine the RAS vascular hemodynamics using CFD.

The objective of this study is to establish a non-invasive methodology for morphological and hemodynamic assessment of RAS. The hypothesis is that there exists an internal relationship between hemodynamic change and morphological transformation of renal arteries. Thus, evaluating the hemodynamic change of different grade stenotic renal arteries can reflect on the morphologic status. Non-contrast MRA was used in this thesis to assess the morphologic status of renal arteries and CFD was used to calculate the hemodynamic parameters of various stenoses.

Newly developed non-contrast MRA technique, named steady-state free precession (SSFP) was investigated and assessed as an accurate method in visualization of renal artery. The

results of CFD simulation demonstrated its potential ability for understanding the relationship between hemodynamics and morphology of renal artery stenosis. The application of CFD technology on modified renal artery stenosis improved prediction of the hemodynamics of renal artery after simulated percutaneous renal angioplasty and stenting.

It was found that CFD simulation can provide useful information for patient stratification and strategy for further treatment decision, and it may also be able to support the clinical practice for intervention treatment of renal artery stenosis.

Declaration of Originality

I hereby declare that this thesis is my original work, as supported by chapters published in various peer reviewed journals, except where acknowledgement has been made below and where due reference is stated otherwise. To the best of my knowledge, this thesis does not contain material that has been accepted for the award for any other degree or diploma at a university or any other tertiary institution. All the models included in this thesis were created and Ethics Committee approvals have been obtained at both Faculty of Medicine and Health Sciences (Reference No.: 5201300448), Macquarie University, and Shanghai Zhongshan Hospital (Approval No.: B2012-095), Fudan University.

I give consent for the thesis to be made available for photocopying and loan if accepted for the award of the degree.

Weisheng Zhang

September 2015

Acknowledgements

First and foremost, I would like to express my deep sincere gratitude to my supervisors, Professor Yi Qian, Professor Jiang Lin and Professor Albert Avolio. They have been always supportive and inspiring on both academic and a personal level in my doctorate candidate period.

I appreciate Professor Mengsu Zeng for agreeing me with a long-time unique opportunity to experience high degree research, culture and life style in Australia. And his suggestions and guidance helped me in all the time of research.

Thanks must be given to Peng Lv, my brother apprentice, whose hard work for data collection, intelligence, and resourcefulness made a real difference in the creation of my thesis.

And thanks to Post-Doctors Jinlong Liu, Yu Zhang, Changjoon Lee, and David I. Verrelli are required. Their kind support for Computational Fluid Dynamics both technically and academically made my research progressing timely and successively.

I am heartily grateful to Kaavya Karunanithi, whose English language support played a key role for the preparation of my papers and this thesis. Happy coffee breaks would be my deepest memory.

In addition, I would like to thank all my best friends in Professor Qian's research group and Australian School of Advanced Medicine, Macquarie University: Liuen Liang, Dashu

Li, Fengping Zhu, Yuka Sen, Peng Hu, Masakazu Higurashi, Nahoko Uemiya, and Ehsaan Askari. The happy time we shared will be memorized eventually.

Most of all, I am grateful to my wonderful wife, Xia Ding, without whom I would not have embarked upon my doctorate candidate in both Fudan University and Macquarie University. Your loving support definitely means a lot to me. Furthermore, thanks with my deepest love must be given to my cute baby boy, Haoyi Zhang. You are the impetus for me to finish my doctorate thesis.

Deepest appreciation goes to my grandparents, my parents and my sister for their loves, endless support and belief in me to achieve my many ambitions. Your contribution and blessing are far too great for words.

On a final note, I dedicate this thesis to my grandfather who passed away in last century. His impact and contribution to my life in my childhood something that I will always treasure and hold in the deepest regard.

Journal Publications

1. **Weisheng Zhang**, Yi Qian, Jiang Lin, Peng Lv, Kaavya Karunanithi, Mengsu Zeng. Hemodynamic Analysis of Renal Artery Stenosis Using Computational Fluid Dynamics Technology Based on Unenhanced Steady-State Free Precession Magnetic Resonance Angiography: Preliminary Results. The International Journal of Cardiovascular Imaging, 2014, 30(2):367-375. (IF=2.322)

2. **Weisheng Zhang**, Jiang Lin, Shaowu Wang, Peng Lv, Lili Wang, Hao Liu, Caizhong Chen, Mengsu Zeng. Unenhanced Respiratory-gated MR Angiography of Renal Artery in Hypertensive Patients Using True Fast Imaging with Steady State Precession Technique Compared with Contrast-enhanced MR Angiography. Journal of Computer Assisted Tomography, 2014, 38(5):700-704. (IF=1.602)

3. Shaowu Wang, **Weisheng Zhang***（**corresponding author**）, Shengbo Na, Lina Zhang, Zhijin Lang. Langerhans Cell Histiocytosis of the Clavicle: A Case Report and Review of the Literature. Medicine® (Baltimore), 2014, 93(20):e117. (IF=4.867)

4. Peng lv, Jiang Lin, **Weisheng Zhang**, Jialu Hu. Computed Tomography Findings of Kommerell Diverticulum. Canadian Association of Radiologists Journal, 2014, 65(4): 321-326. (IF=0.584)

5. Guangzhi Wang, Wei Zhang, Zhuting Fang, Wen Zhang, Minjie Yang, Guowei Yang, Shuo Li, Lian Zhu, Lili Wang, **Weisheng Zhang**, Rong Liu, Sheng Qian, Jianhua Wang, Xudong Qu. Arsenic Trioxide: Marked Suppression of Tumor Metastasis Potential by

Inhibiting the Transcription Factor Twist in Vivo and in Vitro. Journal of Cancer Research and Clinical Oncology, 2014, 140(7): 1125-1136. (IF=3.009)

6. Jun Du, Kun Li, **Weisheng Zhang***（**corresponding author**）, Shaowu Wang, Qingwei Song, Ailian Liu, Yanwei Miao, Zhijin Lang, Lina Zhang, Minting Zheng. Intravoxel Incoherent Motion MR Imaging: Comparison of Diffusion and Perfusion Characteristics for Differential Diagnosis of Soft Tissue Tumors. Medicine® (Baltimore), Medicine® (Baltimore), 2015, 94(25):e1028. (IF=5.723)

Thesis Outline

In this section, a brief overview of each chapter and its content is provided, including brief description, aims and methodologies.

Chapter 1. Introduction and Literature Review

This chapter provides background for this thesis by reviewing related published literature, and presents a brief overview for the anatomy and physiology concept of renal artery diseases and hemodynamics. This chapter includes discussion of renal artery disease, morphological analysis, clinical treatment, and research objectives and thesis outline.

Chapter 2. Non-Contrast MR Angiography Techniques used for Renal Artery Imaging

This section outlines an overview of the non-contrast magnetic resonance angiography techniques with theories, advantages and disadvantages, and clinical applications for renal artery imaging.

Chapter 3. Non-Contrast Respiratory-Gated MR Angiography of Renal Artery in Hypertensive Patients using True Fast Imaging with Steady-State Precession Technique Compared with Contrast-Enhanced MR Angiography

This study involves the idealized non-contrast MR angiography (MRA) technique named TrueFISP. This state-of-the-art non-contrast MRA method is compared with contrast-enhanced MRA for diagnosis of renal artery stenosis in hypertensive patients.

Chapter 4. Hemodynamic Computational Fluid Dynamic Techniques and Their Application in Renal Artery

This chapter provides the techniques of computational fluid dynamics, including blood flow model, processing, convergence criteria, post-processing and its application in renal artery hemodynamics analyzing.

Chapter 5. Hemodynamic Analysis of Renal Artery Stenosis using Computational Fluid Dynamics Technology Based on Non-Contrast Steady-State Free Precession MR Angiography

This chapter reports the study on hemodynamics of stenotic renal artery. The image data used in this study are acquired using non-contrast MR angiography technique. Then patient-specific models are virtually manipulated. Pressure difference (PD), velocity and mass flow rate (MFR) at various renal artery stenotic grades are analyzed. The simulation results are compared with clinical data measured using Doppler ultrasound.

Chapter 6. Analysis of Various Virtual Angioplasty Operation of Renal Artery Stenosis in Hypertension using MR Angiography-Based Computational Fluid Dynamics Technology

Hemodynamics of renal artery after simulated angioplasty will be discussed in this chapter. A hypertensive patient performed non-contrast MRA is diagnosed with right RAS of 70%. In this study, a series of idealized typical stent models are designed using Pro-Engineer software to modify stent treated branch arteries, then the idealized model are connected with the patient-specific artery to form various situations of virtual endovascular treatment. Hemodynamic simulations under the conditions of various virtual endovascular treatments were analyzed in this chapter.

Chapter 7. Conclusions and Future Works

This chapter provides an overview of the objective and findings of this thesis regarding non-contrast MRA and CFD analysis of renal artery in renovascular hypertension. Overall, it was found that the combination of non-contrast MRA with CFD was the first of its kind attempt to utilize completely noninvasive methods for comprehensive evaluation of renal artery stenosis. CFD can provide useful information regarding hypertensive patient stratification and strategy in further treatment. Finally, future directions and necessary considerations are suggested.

List of Figures

List of Tables

List of Abbreviations

ASL	Arterial spin labeling
BB	Black blood
BC	Boundary condition
CFD	Computational fluid dynamics
CT	Computed tomography
DSA	Digital subtraction angiography
D-US	Doppler ultrasound
ECM	Extracellular matrix
ECs	Endothelial cells
eGFR	Estimated glomerular filtration rate
EL	Energy loss
FMD	Fibromuscular dysplasia
FSE	Fast spin echo
FSI	Fluid-solid interaction
FVM	Finite volume method
GPU	Graphic processing units
LSA	Low shear stress area
MRA	Magnetic resonance angiography
MWSS	Maximum wall shear stress
NO	Nitric oxide
NSF	Nephro-genic systemic fibrosis

OSI	Oscillatory shear index
PC MRA	Phase-contrast MRA
PD	Pressure difference
PIV	Particle image velocimetry
RAS	Renal artery stenosis
Re	Reynolds number
RF	Radiofrequency
SNR	Signal-to-noise ratio
SSFP	Steady-state free precession
TOF MRA	Time of flight MRA
TrueFISP	True fast imaging with steady-state precession
VSMC	Vascular smooth muscle cells
WSS	Wall shear stress
WSSG	Wall shear stress gradient

Chapter 1

Introduction and Literature Review

Summary

This chapter provides background for this thesis by reviewing related published literature, and presents a brief overview for the anatomy and physiology concept of renal artery diseases and hemodynamics. This chapter includes discussion of renal artery disease, morphological analysis, clinical treatment, and research objectives and thesis outline.

1.1 Introduction

Renovascular hypertension is caused by renal artery stenosis (RAS) in approximately 1-5% of hypertensive patients (1, 2). The kidney responds to a decrease in blood flow by activating the renin-angiotensin-aldosterone system which increases blood pressure and can result in severe and/or refractory hypertension (3). The relationships between RAS, hypertension, and renal function vary from patient to patient and are difficult to assess, but co-occurrence increase the patient's risk. Renal vascular diseases, encompassing atherosclerotic arterial lesions, fibromuscular dysplasia and Takayasu arteritis, may lead to RAS. Furthermore, 40–50% of patients with occlusive disease of the lower extremities and 15–30% of patients with coronary artery disease have recognizable RAS (4). And in patients with end-stage renal disease, the prevalence of RAS is 10–22% (5, 6). An accurate, reliable and non-invasive method to evaluate severity and hemodynamics of RAS is mandatory (7, 8).

The functional aspect of RAS, such as renal artery flow, can be assessed using digital subtraction angiography (DSA), ultrasound (US), nuclear medicine, and MR angiography (MRA). Currently, DSA technique has been widely recognized as a gold standard for imaging renal arteries. However, due to its invasive nature, a decreasing proportion of DSA are being used in clinical diagnosis of RAS. The blood flow in renal arteries can be noninvasively assessed by US techniques and nuclear medicine, but they are generally unable to illustrate the actual location and the exact stenotic grade of RAS (9-12).

MRA is well suited for both the angiographic illustration of RAS and for assessment of its impact on renal artery flow using contrast-enhanced and phase-contrast (PC) techniques.

Currently, as the common contrast agents containing gadolinium have been linked to a condition called nephro-genic systemic fibrosis (NSF) that can occur in patients with renal insufficiency (13-15), non-contrast MRA without using contrast agents is highly desired as an alternative for patients at risk of developing NSF. Velocity-encoded PC MRA can depict blood flow rates (16); and the flow waveform may have a diagnostic value. Some groups (17, 18) have observed that the flow waveform in the renal artery changes with the extent of the stenosis. However, the vessel depiction quality of PC MRA for RAS is strongly influenced by the choice of velocity encoding (ranging 40-80 cm/s), resulting in decreased peak velocity or flow measurements. Other limitations of PC MRA were longer imaging duration (8-20 min), low spatial resolution, intravascular signal loss, flow artifacts, and difficulty in imaging small vessels and severe stenosis (16, 18-20). A newly developed non-contrast MRA technique, named steady-state free precession (SSFP), comes from the preparation of the imaging volume with a spatially selective inversion pulse, resulting in the suppression of stationary tissue and venous blood, allowing an excellent depiction of renal arteries with high contrast, and it has been accepted as an accurate method in visualization of renal arteries (21-24). However, no hemodynamic information could be provided by SSFP MRA.

From the above discussion, we can see that all of currently available medical imaging techniques could not generally and efficiently provide all the morphological and hemodynamic parameters of the renal arteries in an economic, non-traumatic and one-off way. For overall evaluation of hemodynamics of renal artery, it may be necessary for researchers to develop a novel method from modern computing and engineering imaging.

Nevertheless, it is seen that, patient-specific computational fluid dynamics (CFD) technology, based on either MR or CT images, is one of the novel and efficient technologies to quantitatively estimate hemodynamic conditions. It has been successfully applied in different aspects of the cardiovascular system: intracranial and carotid artery (25-27), heart disease and coronary artery (28-30), aortic artery (31, 32), and pulmonary artery (33). Although the computational method described herein has been introduced to quantitatively characterize the hemodynamic conditions under simulated resting pulsatile flow conditions in an idealized model of an abdominal aorta (34) and thereby estimate the differential pressure at the model of renal artery stenosis based only on structural and flow images, to date there have been no reports to determine the hemodynamic conditions of in vivo RAS with this technology.

In this thesis, the combination of non-contrast MRA and CFD techniques for evaluation of the morphological and hemodynamic parameters of the renal artery were assessed by manipulating patient-specific models. Especially, hemodynamic changes in the renal artery for renovascular hypertension, such as pressure difference (PD), velocity and mass flow rate (MFR), were non-traumatically analyzed for the first time in clinic using CFD method based on non-contrast SSFP MRA images.

1.2 Renovascular Hypertension

1.2.1 Classification of hypertension

Generally, hypertension can be classified into two main branches: primary hypertension and secondary hypertension. Primary hypertension is high blood pressure that has no apparent cause. Renovascular hypertension is the most common cause of secondary hypertension.

The suggested classification used in this thesis is developed following an assessment of the systems used in the United States and in Europe. The diagnosis of hypertension should be based on multiple blood pressure measurements taken on several separate occasions as shown in Table 1:

Table 1. Classification and follow-up of blood pressure levels in adults

Diagnostic category*	Systolic (mmHg)	Diastolic (mmHg)	Follow up
Normal	<120	<80	Recheck in 2 years (or earlier as guided by patient's absolute cardiovascular risk)
High-normal	120-139	80-89	Recheck in 1 year (or earlier as guided by patient's absolute cardiovascular risk)
Grade 1 (mild) hypertension	140-159	90-99	Confirm within 2 months
Grade 2 (moderate) hypertension	160-179	100-109	Reassess or refer within 1 month
Grade 3 (severe) hypertension	≧180	≧110	Reassess or refer within 1–7 days as necessary
Isolated systolic hypertension	≧140	<90	As for category corresponding to systolic BP
Isolated systolic hypertension with widened pulse pressure	≧160	≦70	As for grade 3 hypertension
Hypertensive urgency	>180	>120	(Without target organ damage)
Hypertensive emergency	>180	>120	(Target organ damage)

* When a patient's systolic and diastolic blood pressure levels fall into different categories, the higher diagnostic category and recommended action(s) apply.

1.2.2 Renovascular hypertension

Renovascular hypertension is high blood pressure due to narrowing or blockage of the arteries that carry blood to the kidneys.

1.2.2.1 Causes

Renovascular hypertension is high blood pressure caused by renal artery disease. Normally, the kidneys regulate body fluid and blood pressure, as well as regulate blood chemistry and remove organic waste. Proper kidney function is disrupted, however, when the arteries that provide blood to the kidneys become narrowed, a condition called renal artery stenosis. When stenosis results in reduced blood-flow, the kidney compensates by producing hormones that activate the renin-angiotensin-aldosterone system and increase blood pressure. This response is a healthy one under normal circumstances. But when the reduction in blood-flow is due to stenosis, blood pressure is increased unnecessarily. Renovascular hypertension caused by renal artery stenosis is refractory to control with medication.

The most common cause of renal artery stenosis is a blockage in the arteries due to high cholesterol. This problem occurs when a sticky, fatty substance called plaque builds up on the inner lining of the arteries. Risk factors for atherosclerosis include: high blood pressure, smoking, diabetes, high cholesterol, heavy alcohol use, cocaine abuse and increasing age.

Fibromuscular dysplasia is another cause of renal artery stenosis. It is often seen in women under age 50. It tends to run in families. The condition is caused by abnormal growth of

cells in the walls of the arteries leading to the kidneys. This also leads to narrowing or blockage of these arteries.

1.2.2.2 Signs and symptoms

The kidneys play an important role in regulating blood pressure by secreting a hormone called renin. If the renal arteries are narrowed or blocked, the kidneys cannot work effectively to control blood pressure. Persistent or severe high blood pressure is a common symptom of renal artery stenosis.

Symptoms of renovascular hypertension include:

1) High blood pressure at a young age,
2) High blood pressure that suddenly gets worse or is hard to control,
3) Kidney function suddenly decreases,
4) Narrowing of other arteries in the body, such as to the legs, the brain, the eyes and elsewhere,
5) Sudden pulmonary edema.

If it becomes a dangerous form called malignant hypertension, symptoms may include: bad headache, nausea or vomiting, confusion, changes in vision or nosebleeds.

The health care clinician may hear a "whooshing" noise, called a bruit, when placing a stethoscope over your belly area.

1.2.2.3 Laboratory examination and medical imaging

The following blood tests may be done for laboratory examination: cholesterol level, renin and aldosterone levels, B-type natriuretic peptide, creatinine, potassium and creatinine clearance.

Medical imaging may be performed to check if renal artery stenosis exists including:

1) Angiotensin converting enzyme (ACE) inhibition renography,
2) Doppler ultrasound of the renal arteries,
3) Computed tomography angiography (CTA),
4) Magnetic resonance angiography (MRA),
5) Renal artery angiography.

1.3 Renal Artery Disease

1.3.1 Vasculature of renal artery

Renal arteries normally arise from the sides of the abdominal aorta, immediately below the superior mesenteric artery, and supply the kidneys with blood. Each is directed across the crus of the diaphragm, so as to form nearly a right angle with the aorta. Renal arteries carry up to a third of total cardiac output blood flow to the kidneys. The whole vasculature of the aorta and its branches is shown in Figure 1.

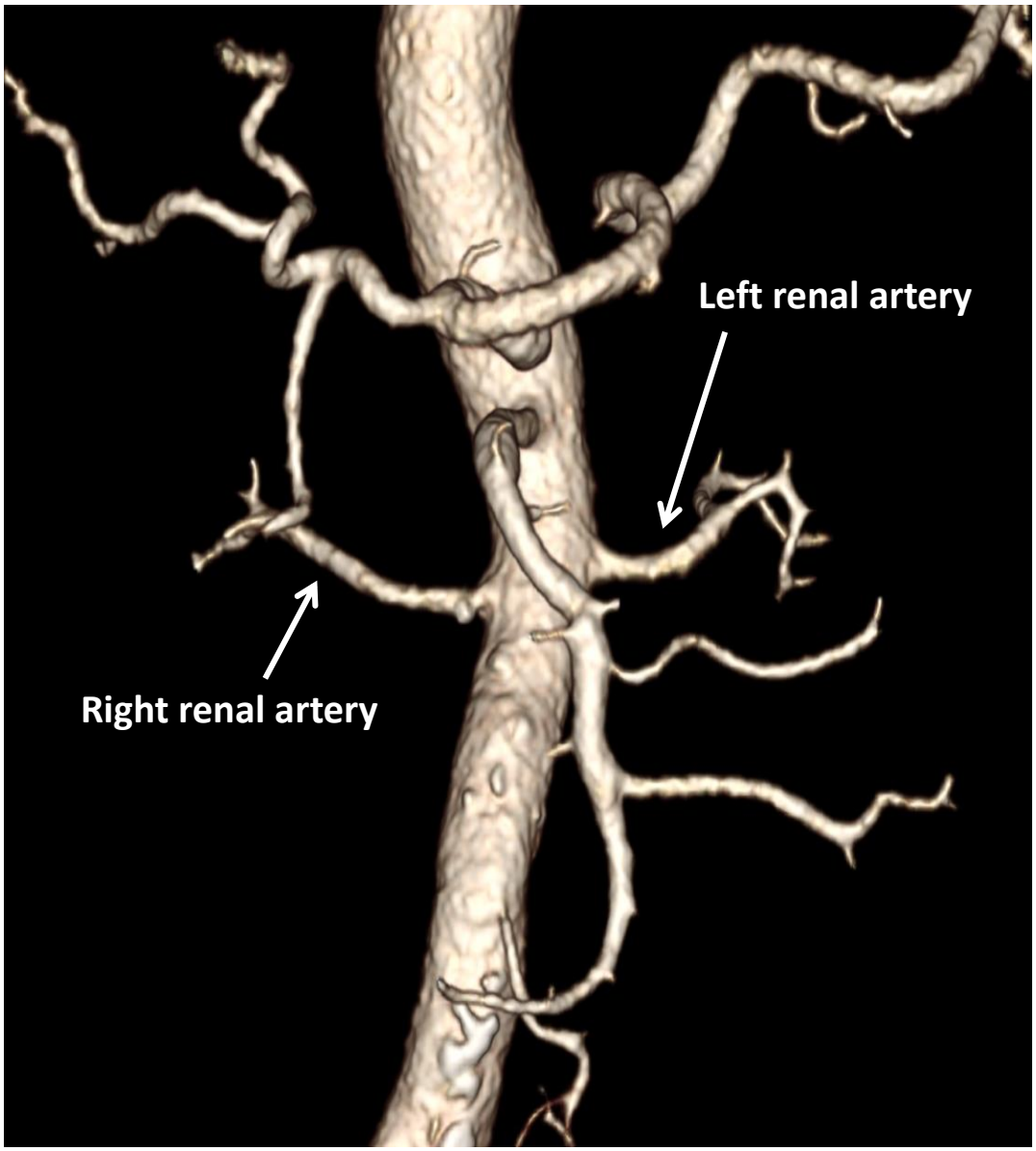

Figure 1. CTA Vasculature of renal artery

The renal artery has a radius of approximately 2.5 mm (35). The measured mean diameter can differ depending on the imaging method used. For example, the diameter was found to be 5.04 ± 0.74 mm using ultrasound, but 5.68 ± 1.19 mm using angiography (36).

Due to the position of the aorta, the inferior vena cava, and the kidneys in the body, the right renal artery is normally longer than the left renal artery. The right passes behind the inferior vena cava, the right renal vein, the head of the pancreas, and the descending part of the duodenum. The right is somewhat lower than the left; it lies behind the left renal vein, the body of the pancreas and the splenic vein, and is crossed by the inferior mesenteric vein. Before reaching the hilum of the kidney, each artery divides into four or five branches; the greater number of these (anterior branches) lie between the renal vein and ureter, the vein being in front, the ureter behind, but one or more branches (posterior branches) are usually situated behind the ureter.

Variant anatomy is common (Figure 2). One or two accessory renal arteries are frequently found, especially on the left side since they usually arise from the aorta, and may come off above (more common) or below the main artery. Instead of entering the kidney at the hilum, they usually pierce the upper or lower part of the organ. The arterial supply of the kidneys is variable and there may be one or more renal arteries supplying each kidney. Supernumerary renal arteries (two or more arteries to a single kidney) are the most common renovascular anomaly, with occurrence ranging from 25% to 40% of kidneys. Early branching exists in 10% of the population.

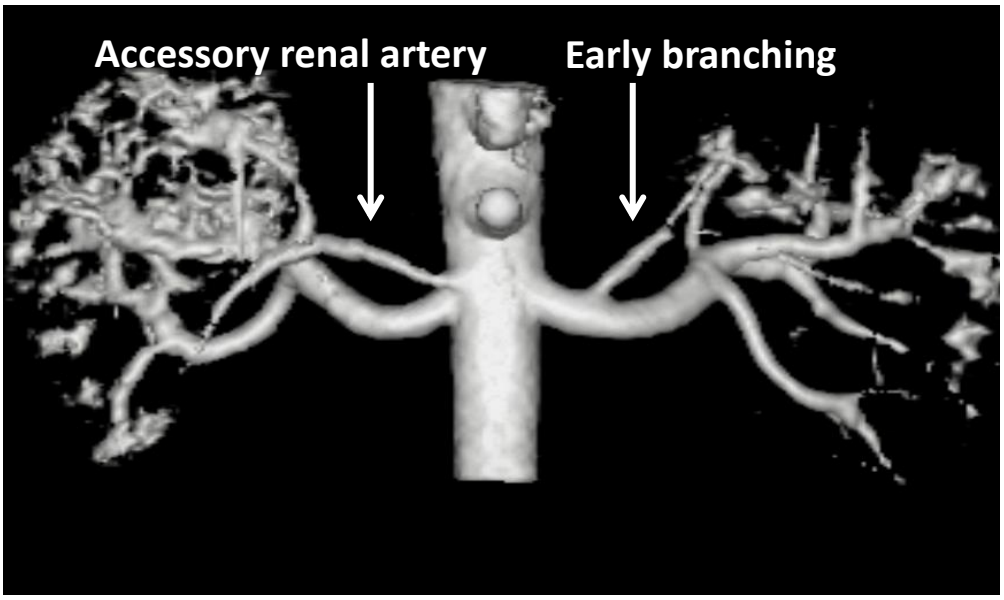

Figure 2. One patient with left renal artery manifesting early branching and right accessory renal artery (MRA image)

1.3.2 Renal artery disease

Renal artery disease is disease of the arteries that supply blood to the kidneys. Atherosclerotic renal artery disease is the most common form of this condition, accounting for more than 80 percent of all renal artery disease (37). The balance is generally caused by fibromuscular dysplasia, a congenital disorder that causes thickening of the artery walls without plaque build-up.

Like the atherosclerosis that affects the arteries of the legs (peripheral artery disease), renal artery disease is caused by a buildup of plaque in the arteries that lead to the kidneys. Plaque is made up of fats and cholesterol, and as it accumulates in the renal arteries, it causes the arteries to stiffen and narrow, which blocks the flow of blood to the kidneys. Total or partial obstructions (blockages) in the renal arteries can cause poorly controlled high blood pressure, congestive heart failure, and kidney failure.

1.3.3 Treatment options for RAS

High blood pressure caused by narrowing of renal arteries is often hard to control. One or more treatments are needed to help control blood pressure. There are many types available including lifestyle changes. Further treatment depends on what causes the narrowing of the kidney arteries.

Renal angioplasty treatment (37-39): A procedure called angioplasty with stenting may be recommended. A small catheter – a long, thin tube – carrying a tiny balloon is inserted through a small puncture in the groin and guided by X-ray to the renal artery. When the

catheter is guided to the narrowed part of the artery, the balloon is inflated. As it expands, it compresses the plaque against the artery walls, re-opening the vessel for blood to flow through. Once the artery is open, the physician may insert a stent at the site to keep the artery open and support the arterial wall. In carefully selected patients, renal angioplasty improves blood pressure and kidney function with minimal risk. It can be done as an outpatient procedure or with only an overnight stay, does not require general anesthesia and has a short recovery time.

Surgical treatment (7, 40): With the development of new and improved types of stents, angioplasty with stenting is the preferred treatment for renal artery disease. However, in some certain cases, surgical treatment will be necessary to restore blood flow to the kidney and preserve kidney function. Surgical treatments for renal artery disease include:

1) endarterectomy, during which a vascular surgeon removes the diseased inner lining of the artery and the plaque deposits.

2) bypass procedure, which involves using a segment from another artery or vein to construct a detour around the blocked area of the renal artery. The most commonly used technique creates a bypass from the abdominal aorta (the large artery in the abdomen) to the kidney using a segment from the saphenous vein in the leg or the hypogastric artery from the abdomen.

There is no single best treatment for renal artery disease. The treatment that is best for a particular will depend on the severity of the disease, the location of the blockages in the arteries, symptoms, overall health, and many other factors.

1.4 Research Objectives

To date, investigations into relationships between clinical information and morphological and hemodynamic analysis of renal arteries confirmed that mechanisms of RAS formation and potential risk factors are not firmly clear and understood.

As mentioned above, the objective of this study is to establish a completely non-traumatic methodology for morphological and hemodynamic assessment of RAS. The hypothesis is that there must be a close relationship and dependence between hemodynamic change and morphological transformation of renal arteries. Thus, evaluating the hemodynamic change of different grade stenosis of renal arteries can reflect on the morphologic status.

Non-contrast MRA was used in this thesis to assess the morphologic status of renal arteries and CFD was used to calculate the hemodynamic parameters of different stenoses. These enabled investigation into possible correlation between morphologic and hemodynamic changes. The non-contrast MRA methods for imaging renal arteries are discussed in Chapter 2, and, especially, TrueFISP MRA technique is evaluated in Chapter 3. Furthermore, CFD techniques are investigated in Chapter 4. Chapter 5 describes a preliminary study on the hemodynamic analysis of stenotic renal arteries using CFD. In addition, one biomedical method has been used with CFD to design renal artery stenting angiography as described in Chapter 6.

The thesis outline is as follows:

Chapter 1. Introduction and literature review

Chapter 2. Non-contrast MR angiography techniques used for renal artery imaging

Chapter 3. Non-contrast respiratory-gated MR angiography of renal artery in hypertensive patients using true fast imaging with steady-state precession technique compared with contrast-enhanced MR angiography

Chapter 4. Hemodynamic CFD techniques and their application in renal artery

Chapter 5. Hemodynamic analysis of renal artery stenosis using computational fluid dynamics technology based on non-contrast steady-state free precession MR angiography

Chapter 6. Analysis of various simulated angioplasty of renal artery stenosis in hypertension using MR angiography-based computational fluid dynamics technology

Chapter 7. Conclusions and future directions

Chapter 2

Non-Contrast MR Angiography Techniques used for Renal Artery Imaging

Summary

This section outlines an overview of the non-contrast magnetic resonance angiography techniques with theories, advantages and disadvantages, and clinical applications for renal artery imaging.

2.1 Introduction

Renal artery conditions should be monitored for hypertensive patients in routine clinical treatment. An accurate and non-invasive method to evaluate severity of RAS is mandatory. Magnetic resonance angiography (MRA) may be one of the best approaches for detecting renal artery conditions.

According to the application of contrast agent, MRA techniques can be divided into two types: contrast enhanced MRA and non-contrast MRA. Severe complications, such as gadolinium-induced nephrogenic systemic fibrosis, can be avoided when non-contrast MRA techniques are used. Along with the two conventional non-contrast MRA techniques, namely time-of-flight (TOF) and phase-contrast (PC) MRA, several novel techniques have been developed, including electrocardiograph-gated fast spin echo (ECG-G-FSE), steady-state free precession (SSFP), arterial spin labeling (ASL), and black-blood (BB) MRA. Appropriate use of these techniques can allow accurate diagnosis of RAS without using contrast materials. Common arterial and venous applications of non-contrast MRA for steno-occlusive and aneurysmal diseases are shown in Table 2.

Table 2. Common application of non-contrast MRA

Arterial application	Venous application
Carotid and cerebrovascular system	Pelvic congestion
Abdominal and thoracic aorta	Iliac vein (May Thurner syndrome)
Pulmonary	Pelvic deep venous thrombosis
Renal	Mesenteric thrombosis
Mesenteric	Portal thrombosis
Celiac	
Iliac	
Lower extremity	
Transplant planning and follow up	

2.2 Indications and Limitations for Non-Contrast MRA

The estimated glomerular filtration rate (eGFR) is a better determinant of renal function than serum creatinine levels (41). Gadolinium should be cautiously used in patients with an eGFR of less than 30 mL/min/1.73 m^2, including dialysis patients (41). Therefore, non-contrast MRA is suitable for these patients as well as patients who may develop allergic reactions to contrast materials. To avoid unnecessary contrast use, it is also appropriate for young or essentially healthy people who undergo a medical check-up. No exposure to radiation or contrast materials allows repeated examinations suitable for screening and follow-up studies. Furthermore, MRA can easily depict calcified vessels and vessels close to bones.

One of the limitations of non-contrast MRA is the long acquisition times relative to those of contrast–enhanced MRA or CT angiography. However, these times have been reduced with recently developed fast acquisition techniques, such as parallel imaging. Second, disadvantage of non-contrast MR angiography is that the imaging range is limited, although multi-coil systems have already been developed to overcome the problem (13). Another limitation is that imaging or understanding imaging findings are difficult because of the imaging techniques and possible artifacts.

2.3 Non-Contrast Magnetic Resonance Angiography Techniques

2.3.1 TOF MRA

Among of all MRA methods, TOF is the most commonly used non-contrast MRA technique. TOF exploits the inflow effect of blood protons using flow-compensated 2D or 3D gradient-echo sequences (42). Unsaturated blood protons flowing into the imaging section or slab have greater signal intensities than do the in-plane or in-slab background stationary protons saturated by repeated radiofrequency excitations with a short repetition time (42). To identify arteries or veins, the pre-saturation pulse is tracked on the upstream side of the imaging section or slab to nullify inflowing signals from the opposite direction (42). For the lower extremities, systolic gating is usually used to enhance the inflow effect and reduce ghost artifacts (42).

Advantages and Disadvantages: The main advantage of TOF MRA is the ease and robustness of imaging and interpretation of images, because the technique has been used for a long time and most radiologists and radiologic technologists are familiar with it. The main limitation is the long acquisition time, especially for 3D TOF. 2D TOF is also time-consuming because the imaging direction must be perpendicular to the vessels to detect the inflow (42). One of the major disadvantages of this technique is the signal loss of in-plane flow due to the saturation effect, particularly in 2D TOF (42). Signal loss also occurs in vessels with complex or turbulent flow, due to intra-voxel dephasing (42), and can result in overestimation of the severity of stenosis, such as in the carotid bifurcation (43). Signal loss due to susceptibility artifacts can also be found because of the nature of

gradient-echo sequence. In addition, TOF angiography cannot depict vessels in which flow is in the opposite direction, because of the saturation bands applied to prevent their contamination.

Clinical Applications: 3D TOF MRA still remains an important method for evaluating intracranial arteries (42). At the same time, 2D TOF angiography is utilized for a wider range of applications, such as in neck arteries and peripheral vessels. However, the diagnostic accuracy of 2D TOF angiography for peripheral arterial disease is generally lower than that of contrast-enhanced MRA.

2.3.2 PC MRA

PC MRA works by detecting a phase shift caused by blood flowing through a magnetic field gradient using bipolar or flow-compensated pulses (42, 44-46). 2D or 3D flow-uncompensated acquisition and flow-compensated acquisitions in three directions are necessary to produce angiographic images by subtraction (42, 46). The velocity-encoding factor, which affects the maximum velocity to be properly displayed, should be carefully preselected (42, 44, 45).

Advantages and Disadvantages: PC MRA, particularly for 3D acquisition, is time-consuming (42, 46, 47). One of the advantages is the independence of flow direction (46). The image acquisition time for 2D imaging can be shorter than TOF MRA because images in planes parallel can be obtained without severe saturation effects (48). Additionally, the PC technique offers excellent background signal suppression (42, 46, 47). One of the disadvantages is the loss of signal in vessels with turbulent flow because of intra-voxel dephasing (47), which can overestimate the degree of stenosis. Furthermore, PC MRA is susceptible to motion because of the characteristics of subtraction. Another limitation is that imaging and image interpretation are often difficult due to the image quality depending on the velocity-encoding factor preselected by the imager.

Clinical Applications: In the last century, before the introduction of the novel non-contrast MRA techniques, PC MRA was widely used for vessels when TOF MRA was not suitable for imaging, including the cerebral and portal veins, renal arteries, and peripheral arteries (48). Nevertheless, conventional PC MRA is routinely used only for the

cerebral veins, because of long acquisition times and image interpretation difficulty (44). Hemodynamics rather than morphologic evaluation has recently become more available with cine 2D PC MRA. Flow direction and flow velocity of vascular diseases such as stenosis, aneurysm, and arteriovenous malformation can be acquired (49-51). The cine 3D PC MRA technique is time-resolved, and is improved by using the VIPR (vastly under-sampled isotropic projection reconstruction) technique (52). It can provide 3D hemodynamic flow information (4D flow) for various vascular diseases, such as velocity, wall shear stress, and pressure difference, with the aid of visualization tools that include 3D streamlines and particle traces (53-57).

2.3.3 ECG-G-FSE MRA

ECG-G-FSE MRA, also called NATIVE SPACE (sampling perfection with application of optimized contrasts using different flip angle evolutions), TRANCE (triggered angiography non-contrast-enhanced), FBI (fresh blood imaging), Delta Flow, and Flow Prep, employs the flow void effect of fast arterial flow during systole (42, 58). It produces bright-blood angiography, with background signals suppressed by subtracting systolic images, in which the signals from arteries with fast flow could not be displayed, from a diastolic image in which signals with slow flow remain at high intensity on T2-weighted images (42, 59). Before data acquisition, additional preparatory steps are necessary to determine the correct timing of systole and diastole using cine 2D MRA or 2D ECG-G-FSE MRA (59, 60). To produce good quality images, reduction of data sampling duration is needed for maximizing the differences in signals between systole and diastole, reducing the T2-weighted effect and motion-related artifacts (42). It can be achieved by partial-Fourier techniques such as half-Fourier acquisition single-shot turbo spin echo (HASTE), rapid acquisition with relaxation enhancement (RARE), single-shot FSE (SSFSE), single-shot turbo spin echo (SSTSE), and fast asymmetric spin echo (FASE) and parallel imaging techniques (42, 59, 60). Three-dimensional sequences with each partition acquired in a single shot are typically used. ECG gated data are usually acquired every two or three R-R intervals to allow sufficient T1 recovery. After the readout direction is set, the phase-encoding direction parallel to the vessels is recommended (42). In arteries with slow flow, flow-spoiling gradient pulses are used in the readout direction to increase the flow-dephasing effect during systole (42).

Advantages and Disadvantages: Each image acquisition time of ECG-G-FSE MRA is relatively short. Images can be acquired in planes parallel to the vessels and the total image acquisition time is shorter than with TOF MRA (42). Another advantage is the sensitivity of the technique to peripheral slow flow, which allows displaying of thin vessels (42). One of the disadvantages is the complexity of imaging. In particular, inappropriate trigger timing results in poor image quality (42, 59). Another disadvantage is the poor detection of vessels because of differences in flow velocities, such as in regions distal to a stenosis and in collateral vessels (42). ECG-G-FSE MRA is sensitive to motion because of the nature of subtraction (59).

Clinical Applications: ECG-G-FSE MRA is suitable for evaluating peripheral arteries because of its sensitivity to slow flow (59). Thinner vessels such as collaterals and runoff vessels can also be depicted (59, 61). However, the application for renal arteries is difficult because these arteries are perpendicular to the readout direction (42). 3D high-spatial-resolution FSE sequences have advantages with the recent development of a variable flip angle with spatially nonselective radiofrequency (RF) refocusing pulses such as SPACE, VISTA, and Cube (61). This can dramatically reduce the data sampling time because of reduced echo spacing, and it can provide more detailed angiography of distal arteries (61). As an advanced technique, ECG-G-FSE MRA can be used for non-contrast MR DSA by obtaining multiple acquisitions during systole, allowing visual hemodynamic evaluation of pulse-wave transmission in arteries.

2.3.4 SSFP MRA

SSFP MRA, also known as TrueFISP (fast imaging with steady-state precession), FIESTA (fast imaging employing steady state acquisition), Balanced FFE (fast field echo), and TrueSSFP, is a gradient-echo based sequence that maintains steady-state longitudinal and transverse magnetization by applying a series of equidistant radiofrequency pulses (62-64). The images do not rely on an inflow effect (42, 62, 63). 3D acquisition is used to produce angiographic images with a high signal-to-noise ratio (SNR).

Advantages and Disadvantages: The major advantages of SSFP MRA are short acquisition time and high SNR (63, 64). Furthermore, SSFP MRA with 3D acquisition is relatively independent of flow direction because of fully flow compensated analysis in all three directions (42, 63, 65). However, the inflow effects partly affect image quality. One of the disadvantages of the technique is its susceptibility to field heterogeneities (42, 63). Therefore, additional preparatory pulses to suppress background signals are necessary to selectively show arteries; and post-processing is needed to remove additional background signals.

Clinical Applications: SSFP MRA is utilized for the aorta, particularly with ECG gating in the thoracic aorta (66, 67). The technique is also used with respiratory triggering for renal artery stenosis. Furthermore, it is now feasible to perform whole-heart coronary MR angiography with ECG gating, which allows noninvasive detection of coronary artery stenosis with high sensitivity and moderate specificity using 1.5-T imagers (68, 69).

2.3.5 ASL MRA

ASL MRA is increasingly used as a qualitative perfusion contrast technique to detect changes in cerebral blood flow (70). In addition, ASL is used to produce angiographic images in combination with SSFP or ECG-G-FSE MRA, also known as spatial labeling inversion pulse (TimeSLIP), NATIVE TrueFISP, and inflow inversion recovery (IFIR) (42). Three different approaches can be used with this technique. The simplest approach is to apply a slab-selective IR pulse to the image plane (63). Combining with an appropriate inversion time, the background signals are substantially suppressed, while inflowing blood from outside the slab provides high signal intensity. Another approach is applying a slab-selective IR pulse upstream in the imaging plane (42). Subtracting images could be obtained with the upstream IR pulse, in which inflowing blood from the suppressed area with low signal intensity and images obtained without the IR pulse showing bright-blood angiograms. The third approach is to use nonselective and slab-selective IR pulses (42, 71). The nonselective IR pulse inverts the magnetization of the entire imaging field. In contrast, the slab-selective IR pulse applied immediately afterward upstream from the target vessels displays flowing blood from the suppressed background with high signal intensity.

Advantages and Disadvantages: The advantages of ASL techniques with SSFP MRA are a high signal-to-noise ratio and sufficient suppression of background area. However, the acquisition time is generally longer than SSFP MRA. Another disadvantage is the likelihood of overestimating stenosis due to severe signal loss of the distal part of the stenotic vessel (65).

Clinical Applications: ASL with SSFP MRA is often used with a slab-selective IR pulse to the image plane for imaging renal arteries, commonly with ECG or respiratory gating. Wyttenbach et al reported that this sequence provided high sensitivity (95%–100%), high specificity (93%–95%), and a high negative predictive value (99%–100%) for the detection of high-grade renal artery stenoses (65). SSFP angiography with ASL can also be used for portal veins (72) and head and neck arteries (73). Images of the hepatic vein and inferior vena cava can also be obtained through using another slab-selective IR pulse (74). Finally, ASL with SSFP MRA and nonselective and slab-selective IR pulses allows angiography of the abdominal visceral arteries such as the hepatic artery (75). Last but not less important, it was recently reported that the ASL technique can be used to produce MR DSA images, which provide valuable hemodynamic information (76). These images can be obtained with multiple data acquisitions with different delay times (76).

2.3.6 BB imaging

Although BB imaging, also called dark-blood, is not used to produce angiographic images, it can be used to evaluate vessels, including intraluminal or mural abnormalities, because detection of the flowing blood is suppressed. The most common approach is using FSE sequence with double IR pulses and ECG gating (77, 78). This involves applying a nonselective IR pulse followed immediately by a section-selective IR pulse (78). Data are acquired during diastole when the signals from inflowing blood cannot be displayed after the inversion time.

Advantages and Disadvantages: One of the disadvantages of BB imaging with double IR pulses is the relatively long acquisition time due to ECG gating (78). Although images can be improved by partial Fourier (78) and multi-section acquisition (79), conventional BB imaging cannot produce angiographic images.

Clinical Applications: BB imaging can be used to evaluate intraluminal and mural abnormalities, including plaque (43, 77), dissection (78), and thrombus. Morphologic evaluation of carotid plaque is important because vulnerable plaque and intra-plaque hemorrhage are associated with subsequent ischemic attacks (43, 77). BB imaging can help to differentiate recent hemorrhage and the lipid-rich necrotic core from fibrous tissue (43, 77). Currently, some novel black-blood imaging techniques have been described. One is the modified rotating k-space reconstruction scheme known as PROPELLER (periodically rotated overlapping parallel lines with enhanced reconstruction), BLADE (rotating bladelike k-space covering), MultiVane, and JET. These correct in-plane motion

displacement of flowing blood by oversampling the center data of k space. They can be used to screen carotid plaque because they can provide multi-section images with a relatively short acquisition time without ECG gating (80). Another new technique uses a 3D high-spatial-resolution FSE sequence in combination with a variable flip angle and spatially nonselective RF refocusing pulses with the names SPACE, VISTA, and Cube (81). This approach increases the number of echoes in each excitation because of reduced echo spacing (81). Moreover, high-spatial-resolution 3D BB imaging can be acquired because of flowing blood dephased and blood signals suppressed without ECG gating (81). This technique can be used to evaluate vessel walls from different angles and can even produce angiographic images by inverting the display intensity.

2.4 Conclusions

Generally, non-contrast MRA techniques provide alternative methods to imaging vessels of different body parts without using contrast materials. TOF MRA is the main technique for evaluating intracranial arteries. PC MRA, including 4D, is increasingly used for physiologic evaluation rather than morphologic evaluation. ECG-G-FSE MRA can show peripheral arteries in more detail. SSFP MRA with or without ASL can provide high-resolution images of the aorta, renal arteries, and coronary arteries. BB imaging is used to evaluate vessel walls and intravascular abnormalities including dissection, plaque, and thrombi. In conclusion, SSFP MRA may be a better method for imaging renal arteries than other techniques. Non-contrast MRA can avoid the potentially severe adverse effects associated with contrast materials, such as nephrogenic systematic fibrosis. We believe that there is a bright future for non-contrast MRA imaging of renal arteries, along with the technique’s further development.

Chapter 3

Non-Contrast Respiratory-Gated MR Angiography of Renal Artery in Hypertensive Patients using True Fast Imaging with Steady-State Precession Technique Compared with Contrast-Enhanced MR Angiography

Published as

Weisheng Zhang, Jiang Lin, Shaowu Wang, Peng Lv, Lili Wang, Hao Liu, Caizhong Chen, Mengsu Zeng. Unenhanced respiratory-gated magnetic resonance angiography (MRA) of renal artery in hypertensive patients using true fast imaging with steady-state precession technique compared with contrast-enhanced MRA. Journal of Computer Assisted Tomography, 2014, 38(5):700-704. (IF=1.602).

Summary

This study involves the idealized non-contrast MR angiography (MRA) technique named TrueFISP. This state-of-the-art non-contrast MRA method is compared with contrast-enhanced MRA for diagnosis of renal artery stenosis in hypertensive patients.

3.1 Introduction

Renovascular hypertension exists in approximately 5% of hypertensive patients (1, 2). Renal vascular disease is a complex entity, encompassing atherosclerotic arterial lesions and fibromuscular dysplasia (FD), leading to high renal and cardiovascular risk. It is known that 40– 50% of patients with occlusive disease of the lower extremities and 15–30% of patients with coronary artery disease have recognizable RAS (4). Reports of end-stage renal disease indicate RAS prevalence of 10–22% (5, 6).

Owing to the improvements of scanning techniques, studies appropriate for the diagnosis of renal artery stenosis are digital subtraction angiography (DSA), ultrasound (US), computed tomography angiography (CTA), and magnetic resonance angiography (MRA). To date, DSA technique has been widely recognized as a gold standard for imaging renal artery. However, there has been a decreasing tendency to use DSA in clinical imaging of RAS due to its invasive nature. Intravenous DSA is no longer recommended, and intra-arterial DSA is reserved for pre-revascularization planning. Currently, US is the most widely used imaging method for initial investigation and can provide the measurement of flow velocities. But the field of view is often limited to the acoustic window and the diagnosis is highly dependent on operators. Increased radiation exposure and potential nephrotoxicity of iodinated contrast agents are the major disadvantages of CTA; CT examinations should, therefore, be ordered judiciously in patients with impaired renal function. Contrast-enhanced MRA (CE-MRA) can be the gold standard for evaluating renal vasculature because it enables high spatial and temporal resolution with extremely

fast imaging times (82-84). However, recently, the use of injected contrast media has come under scrutiny because the common contrast agents containing gadolinium have been linked to a condition called Nephrogenic Systemic Fibrosis (NSF) that can occur in patients with renal insufficiency (13-15). As a result, use of gadolinium should be avoided in patients with known risks for developing NSF unless the diagnostic information cannot be obtained with a non-contrast enhanced MR. To date, non-contrast MRA without using any contrast agent is highly desired as an alternative for patients at risk of developing NSF.

Various non-contrast MRA techniques have undergone a substantial development and are effectively used for visualization of coronary artery (85, 86), renal artery (13, 22-24, 65, 87-89), and lower extremity arteries (87). Respiratory-gated "True fast imaging with steady-state precession" (TrueFISP) was a recently developed optimized technique and enabled visualization of the renal arteries with high contrast and high spatial resolution, by using a slab-selective inversion pre-pulse to suppress the renal parenchymal signal and renal venous signal, without use of contrast agents. The purpose of our study was to investigate the accuracy of TrueFISP MRA for detecting renal artery stenosis in comparison with CE-MRA.

3.2 Materials and Methods

3.2.1 Patients

From July 2012 through to July 2013, 22 consecutive patients (16 male, 6 female; age range, 24-72 years; mean age ± standard deviation, 46.4 years ± 11.9) who had

hypertension and who were suspected of having RAS on the basis of clinical history, physical examination results, or Duplex US findings were prospectively enrolled in the study. The study was approved by the institutional ethics committee of Shanghai Zhongshan Hospital of Fudan University (Shanghai, China) and granted by the Macquarie University Human Research Ethics Committee (HREC (Medical Sciences)). Both non-contrast respiratory-gated TrueFISP MRA and CE-MRA were performed during one imaging session. All 22 patients were fasting for 3 hours before MRA imaging and trained for regular breathing before scanning.

3.2.2 MRA examination

All MRA examinations were performed with a 1.5-T MR imager (MAGNETOM Aera, software version syngo MR D11; Siemens Healthcare, Erlangen, Germany) equipped with 2 body coils placed both at the front (18-element body matrix) and back (12-element spine matrix) of the abdomen. All patients were scanned in the supine and feet-first position with a refractory belt put around the abdomen to reduce motion artifact while a respiratory-gated navigator was placed at the inferior level of the diaphragm to synchronize data readout to trigger TrueFISP scanning with free breathing.

After acquisition of scout images, non-contrast TrueFISP MRA (syngo NATIVE TrueFISP; Siemens Medical Solution) was performed before CE-MRA using a balanced steady state gradient echo technique triggered by respiratory-gated navigator. The preparation of the imaging volume with a spatially selective inversion pulse was used to suppress signal from stationary tissues at the background and suppress signal from venous blood within the

imaging volume. Depending on patient respiratory rhythm, inversion time and acquired number of imaging sections, the acquisition time ranged from 5 to 7 minutes (300-420 seconds).

Non-contrast and contrast-enhanced MRA protocol parameters are listed in Table 3.

Table 3. Sequence parameters of CE-MRA and TrueFISP MRA

Parameter	CE-MRA	TrueFISP MRA
Repetition time (msec)	3.17	1293.8
Echo time (msec)	1.10	1.49
Data acquisition time (sec)	13	300-420
Flip angle (degree)	25	90
Bandwidth (kHz)	450	781
Field of view (mm^2)	400×320	320×240
Slice thickness (mm)	1.2	1.0-1.2
No. of slices	80-94	64-80
Matrix	288×384	192×256
No. of acquired partition	1	1
Accelerated factor	3	2
Time of inversion (msec)	-	1200

To reduce the signal intensity of the background tissue during CE-MRA, a 3D data set that served as mask image data was obtained before contrast material administration and was subtracted from the arterial phase contrast enhanced images. High-spatial-resolution breath-hold contrast-enhanced MRA was performed with a 3D gradient-echo fast low-angle shot pulse sequence after administration of 0.2 mmol gadopentetate dimeglumine injection (Iohexol; Beijing Beilu Pharmaceuticals, Beijing, China) per kilogram of body weight, which was followed by 20 ml saline at 2.0 ml/sec in all examinations.

3.2.3 Data post-processing

DICOM image data was transferred to the imaging workstation Vitrea (Version 6.5.1, Toshiba, Minnetonka, United States) and also to the commercial image processing package Mimics (Version 14.0, Materialise Company, Leuven, Belgium). Vitrea was used to calculate the length of maximal visible renal arteries and number of visualized branch vessels, while Mimics was used to measure the volume of the main renal arteries. A technologist with experience in 3D reconstruction techniques performed all standardized post-processing procedures. This technologist was not involved in the subsequent image analysis and was blinded to the patient clinical information. Volume rendering (VR) and maximum intensity projection (MIP) display of the renal arteries was generated. All reconstructions were performed in an identical manner for TrueFISP MRA and CE-MRA during separate sessions; and the reconstructed images were stored for subsequent evaluation. The presence or absence of accessory renal arteries was not assessed in this

study; and only the main blood supply renal artery was evaluated when accessory renal artery appeared.

TrueFISP MRA and CE-MRA images were analyzed jointly by two radiologists with 11 and 5 years of experience in cardiovascular imaging. Both readers were blinded to the patient clinical data and a consensus was reached for each patient. TrueFISP MRA and the corresponding CE-MRA images obtained in the same patients were assessed separately in random order, with an interval of at least 2 weeks between the readings. Data analysis was based on source images，VR and MIP reconstruction. Both readers were allowed to perform additional reconstructions, if necessary.

For quantitative analysis, all renal arteries were analyzed to determine volume of the main renal arteries (Figure 1), length of maximal visible renal arteries (Figure 2), and number of visualized first branch vessels. Main renal artery volume size was calculated from ostium to the end of main renal artery. The maximum visible renal artery length was measured from the ostium to the most distal visible end of the renal artery branch. The maximum visible renal artery length and visualized branch vessel number were measured on VR reconstructions obtained using both techniques.

Additionally, the extent of RAS was graded as follows: Grade 1 (normal) indicated less than 24% luminal narrowing; grade 2 (mild), 25%–49%; grade 3 (moderate), 50%–74%; grade 4 (severe), 75%–99%; and grade 5 (occlusion), 100%. Stenosis grading was performed using an electronic caliper to measure the minimal luminal diameter at the

optimal projection angle along the vessel axis. The percentage of stenosis was calculated as follows:

$$\% \text{ of stenosis} = [1 - (S/R)] \times 100 \qquad (1)$$

Where S and R are the diameters of the stenosis and the reference site, respectively. Reference site was defined as the normal-looking portion of vessel presented either distal or proximal to the lesion.

For qualitative assessment, all main renal arteries were divided into proximal, middle, and distal segments. Image quality was based on the degree of artery visualization, motion artifacts, and signal suppression in the background. The image quality of VR and MIP images, three segments of main renal arteries, and first branches of renal arteries of the source images were graded using a five-point scale: grade 4 indicated excellent (high homogeneous signal intensity within vessel lumen, optimal delineation of vessel border, no artifacts present); 3, good (good enhancement of vessel lumen, incomplete delineation of vessel border, some artifact may be present); 2, fair (low inhomogeneous signal intensity, incomplete delineation of vessel border, diagnostic evaluation possibly impaired); 1, poor (minimal enhancement, diagnostic evaluation hardly possible); and 0, non-diagnostic (no enhancement, non-diagnostic). An image quality score of 4-2 was defined as an acceptable image quality, and images with a score 1-0 were excluded from further analysis.

3.2.4 Statistical analysis

The data was presented as mean ± SD. For continuous variables, paired two-tailed Student t test was applied to evaluate values of the volume of main renal arteries, length of maximal visible renal arteries, and number of visualized first branch vessels between TrueFISP MRA and CE-MRA. The Wilcoxon signed rank test was used to analyze ordinal scaled image quality scores. For assessment of image quality, mean grades obtained from TrueFISP MRA and CE-MRA were calculated and compared. A two-tailed P value 0.05 or less with 95% intervals was considered to indicate a significant difference. Statistical analyses were performed with the commercially available SPSS software (version 16.0; SPSS, Chicago, III).

3.3 Results

TrueFISP MRA and CE-MRA were successfully acquired in all 22 patients and the total number of main renal arteries was forty-four.

In forty-four main renal arteries, volume and maximal visible renal arteries length were measured. The volume of main renal arteries was smaller in CE-MRA (Figure 3a) than those from TrueFISP MRA (Figure 3b), but no significant difference was indicated between CE-MRA and TrueFISP MRA (1187.2 mm^3 ± 566.5 in CE-MRA, and 1212.2 mm^3 ± 505.5 in TrueFISP MRA, P = .62). The length of maximum visible renal artery was less from CE-MRA (Figure 4a, 4c, 4e) than those from TrueFISP MRA (Figure 4b, 4d, 4f), but no significant difference was shown between the two techniques (87.3 mm ± 20.4 in

CE-MRA vs 88.3 mm ± 19.6 in TrueFISP MRA, P = .59). Number of visualized first branch vessels was slightly greater from TrueFISP MRA than those from CE-MRA, which did not significantly differ between two techniques (3.77 ± 1.78 in CE-MRA vs 3.80 ± 1.44 in TrueFISP, P = .91). The results for the quantitative measurements are summarized in Table 4.

Table 4. Quantitative measurement of renal artery (RA)

	CE-MRA*	TrueFISP	P Value
Volume of main RA (mm^3)	1187.2±566.5	1212.2±505.5	0.62
Length of maximal visible RA (mm)	87.3±20.4	88.3±19.6	0.59
Number of RA first branches	3.77±1.78	3.80±1.44	0.91

* Scores are means ± standard deviations. P values were derived by using paired Student t test.

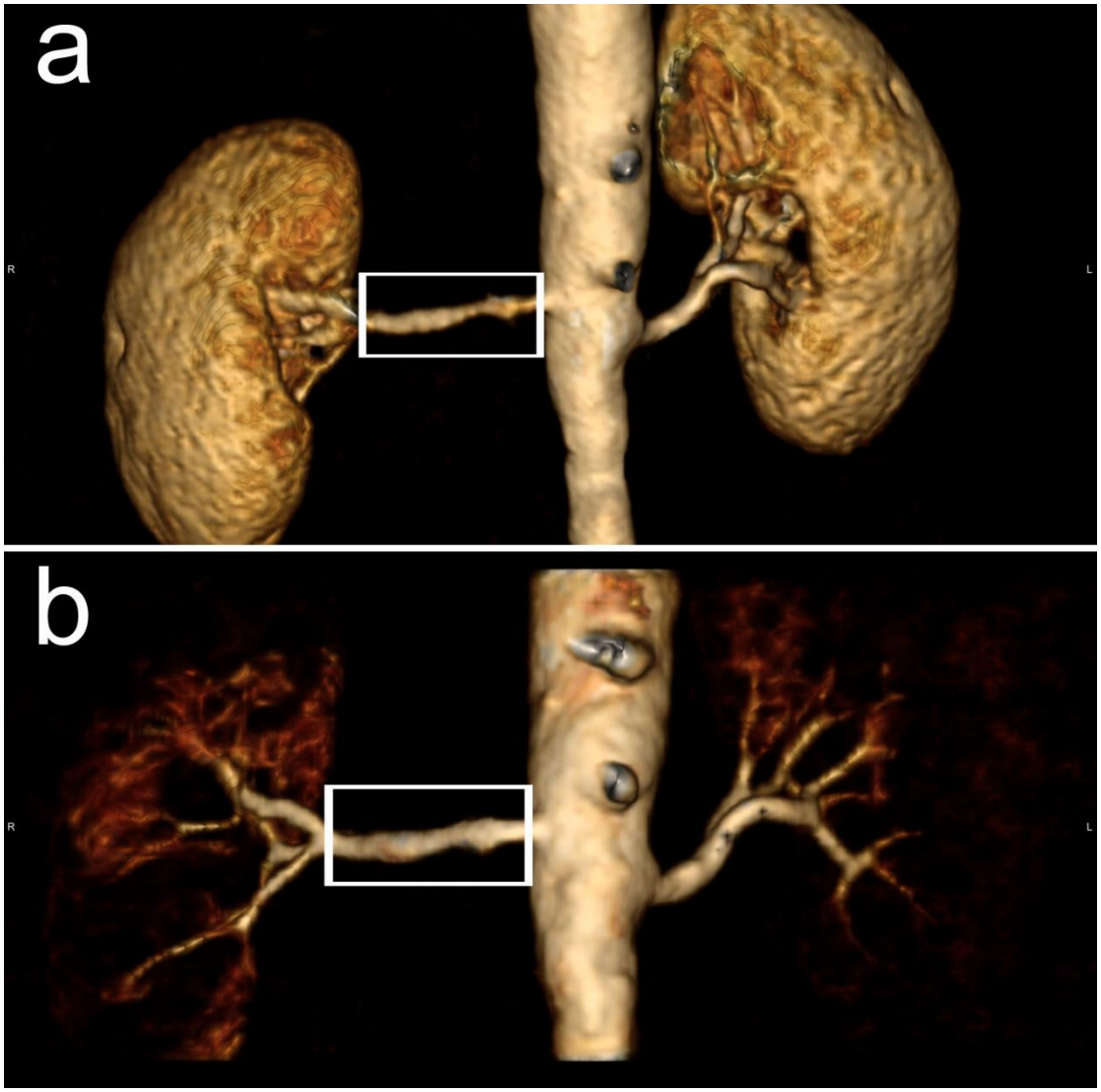

Figure 3. Volume rendering and maximum intensity projection images of renal arteries from CE-MRA (a) and from TrueFISP MRA (b) with respiratory gating in a 55–year-old female with refractory hypertension. Main renal artery volume was calculated from the ostium to the end of main renal artery shown in the rectangle frame (a, b). The volume of right main renal artery was 754.3 mm^3 from CE-MRA and 936.7 mm^3 from TrueFISP MRA

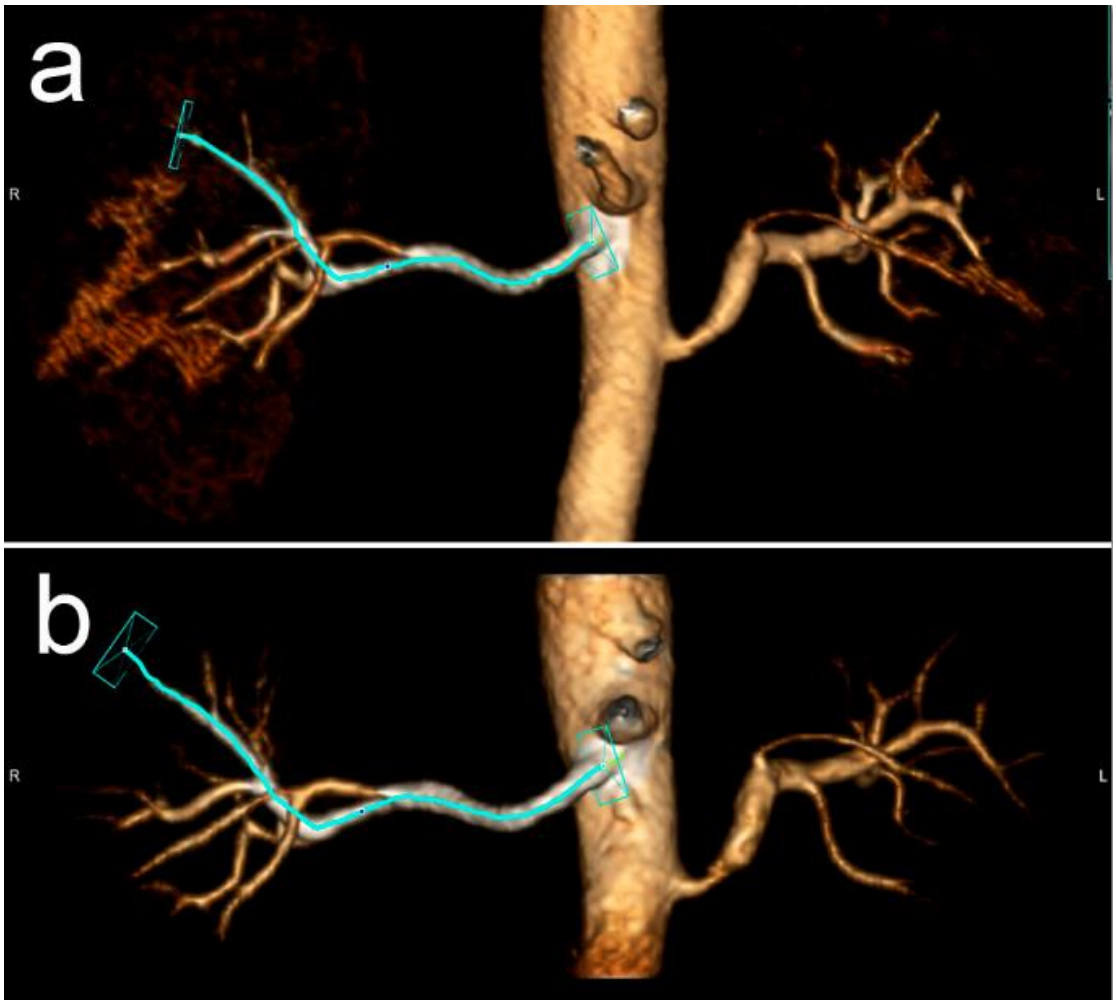

Figure 4. Volume rendering, maximum intensity projection and curved planar images acquired from CE-MRA (a, c, e) and TrueFISP MRA (b, d, f) in a 52-year-old man with hypertension resistant to medication. Left renal artery stenosis was diagnosed according to the images. The maximal visible length of right renal artery from the ostium to the distal end was calculated as about 103.3mm from CE-MRA and 112.5mm from TrueFISP MRA (c,d,e and f were shown on next page.)

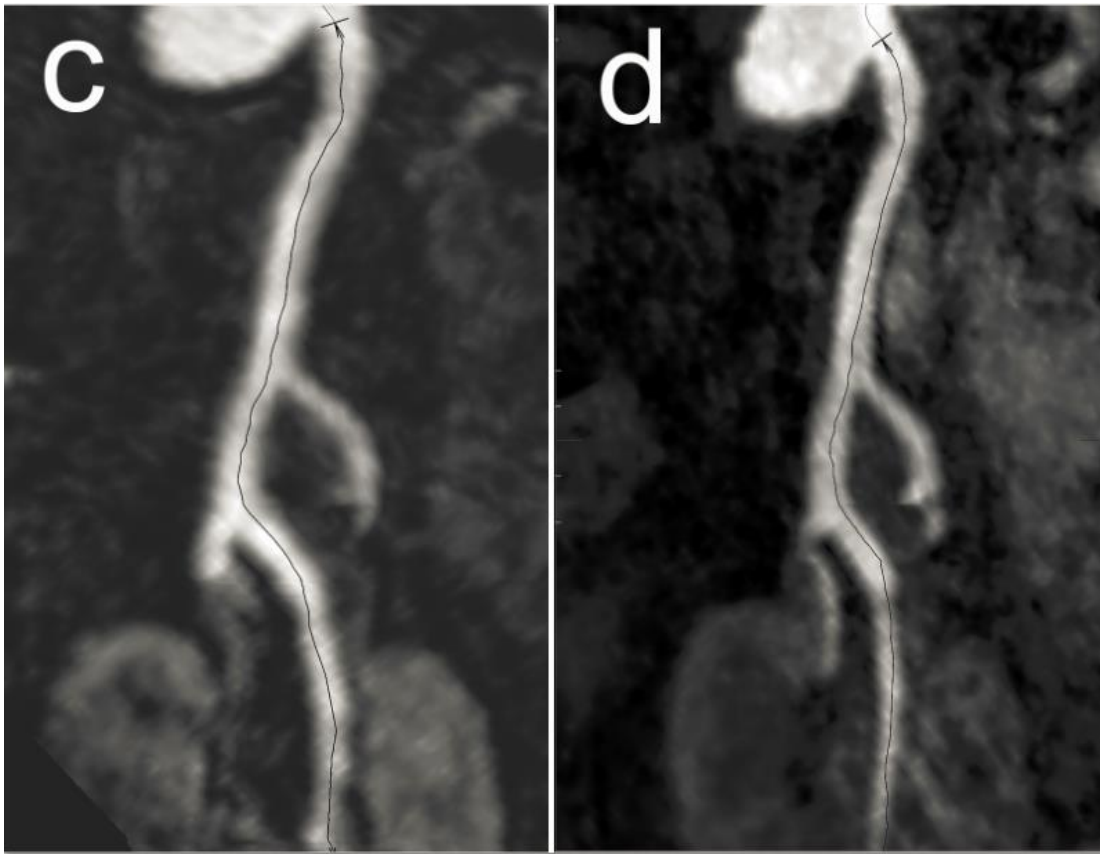
c
d


e
f

For assessment of the severity of stenosis, a total of 44 main renal arteries were evaluated. CE-MRA found a total of 13 RAS with stenotic grades from mild to severe. TrueFISP MRA showed eight RAS with stenotic grades from mild to moderate. Five (13-8; 38.5%, 5/13) false-positive results existed in CE-MRA. In three (24%) of 13 RAS cases, the findings were concordant between CE-MRA and TrueFISP MRA. Inconsistency was found between the two techniques on 10 (76%, 10/13) segments with the calculated degree of stenosis greater for the CE-MRA images (Figure 5a) than TrueFISP MRA (Figure 5b), especially regarding Grade 4 stenosis.

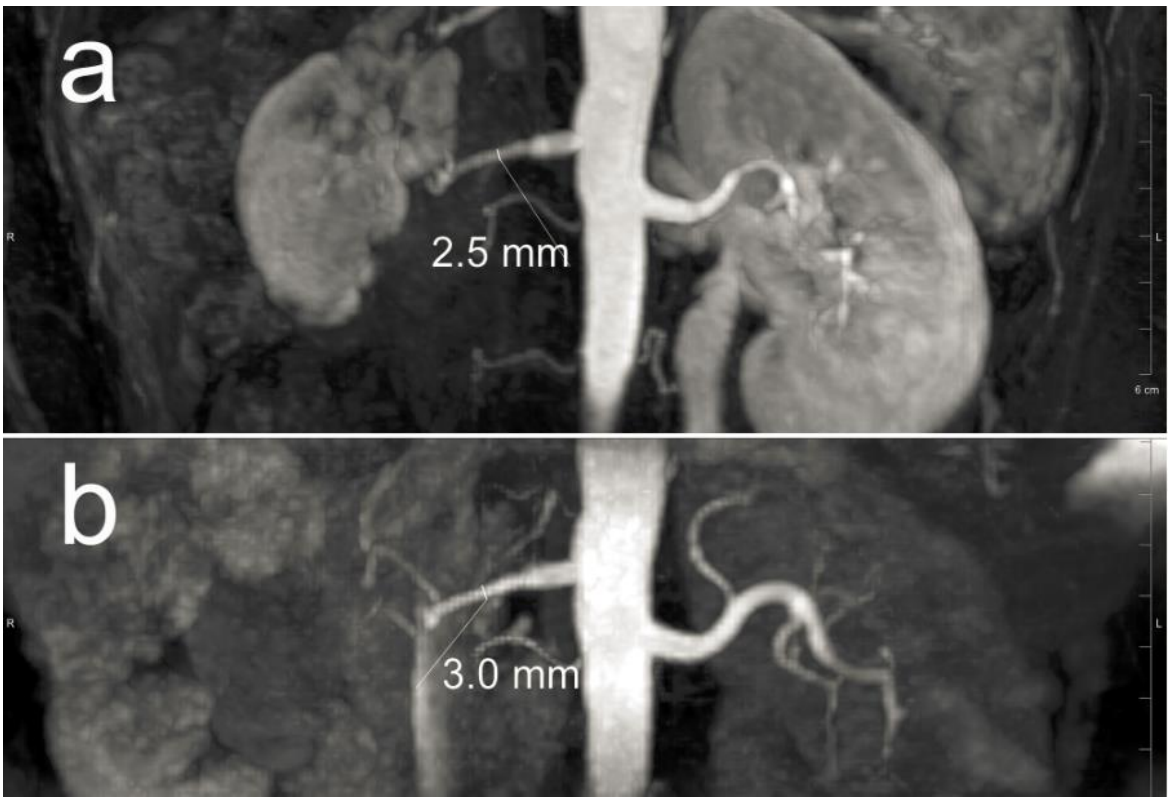

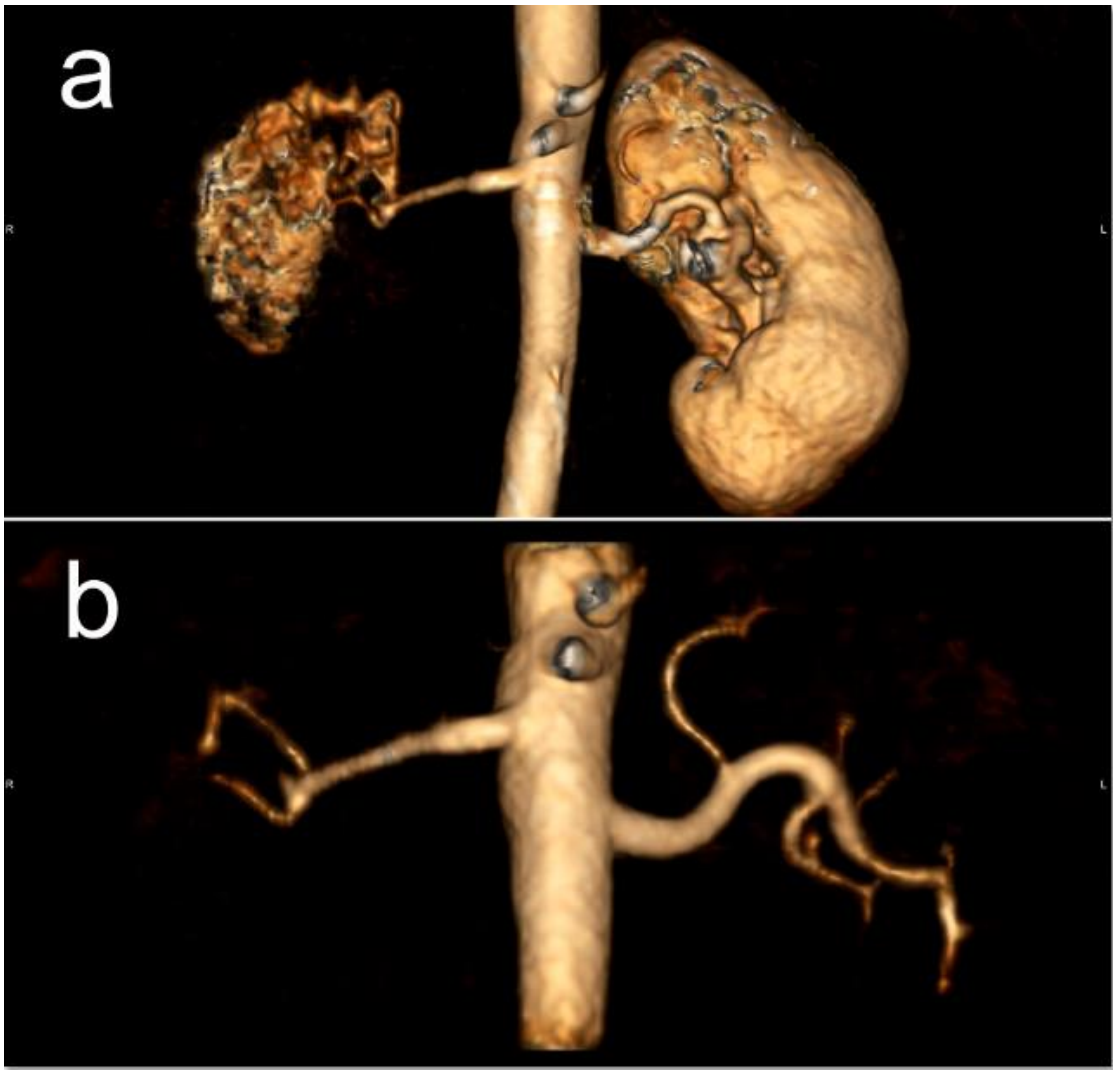

Figure 5. The diameter stenotic degree of right renal artery from CE-MRA (a) was greater than those from TrueFISP MRA (b) in the maximum intensity projection and volume rendering images in a 56-year-old hypertensive female with right kidney atrophy. The stenotic degree of right renal artery was 55% from CE-MRA and 45% from TrueFISP MRA, respectively

Image quality in each renal artery was acceptable. There was no significant difference of the image quality of proximal segments between the two techniques (P > .05). Qualitative scores for VR and MIP images, middle and distal segments of the main renal arteries, and their first branches, were higher on images from TrueFISP MRA than those from CE-MRA (P < .05). Qualitative scores of the image quality assessment for TrueFISP MRA and CE-MRA are summarized in Table 5.

Table 5. Qualitative assessment of 44 renal arteries between CE-MRA and TrueFISP MRA in 22 patients with hypertension

	CE-MRA	TrueFISP	P
Proximal segment	3.77 ±0.42	3.93 ±0.26	0.051
Middle segment	3.48 ±0.59	3.75 ±0.44	0.017
Distal segment	3.32 ±0.74	3.61 ±0.54	0.031
First branches	2.77 ±0.61	3.00 ±0.69	0.012

Scores are means ± standard deviations. Image quality: Score 0, indicated non-diagnostic (no enhancement, non-diagnostic); 1, poor (minimal enhancement, diagnostic evaluation hardly possible); 2, fair (low inhomogeneous signal intensity, incomplete delineation of vessel border, diagnostic evaluation possibly impaired); 3, good (good enhancement of vessel lumen, incomplete delineation of vessel border, some artifact may be present); 4, excellent (high homogeneous signal intensity within vessel lumen, optimal delineation of vessel border, no artifacts present). *P* values were derived by using the Wilcoxon signed rank test.

3.4 Discussion

In our study, TrueFISP MRA was performed to evaluate RAS in hypertensive patients. Our patient data demonstrated that it had capabilities for the depiction of renal arteries and for the detection of renal arterial stenosis comparable with those from CE-MRA in patients with hypertension.

Commonly used non-contrast MRA techniques, including phase-contrast and time-of-flight, have not been successfully used in clinical practice for renal arterial visualization because of their low spatial resolution, prolonged imaging time and flow artifacts. Newly developed steady-state free precession non-contrast technique, named TrueFISP technique, offers superior signal-to-noise ratio and high contrast between blood and soft tissue. TrueFISP MRA comes from the preparation of the imaging volume with a spatially selective inversion pulse, resulting in the suppression of stationary tissue and venous blood, so it allows an excellent depiction of renal arteries with high contrast between arteries and surrounding soft tissues without use of contrast agents. TrueFISP is further powered by parallel imaging, which allows for rapid data acquisition of renal artery MRA within a clinically practical imaging time.

Our data demonstrated a good agreement between TrueFISP MRA and CE-MRA, though volume of main renal arteries and length of renal arteries shown in the images from TrueFISP MRA were a little greater than those from CE-MRA. To our knowledge, it is the first report utilizing volume statistics to analyze renal arteries. Volume data may be a more accurate method for assessing renal arteries especially for the severe stenotic renal arteries

for which diameters cannot be measured easily and correctly. Mimics, which was used for analyzing the volume of main renal artery, is generally accepted as an established mature method to be utilized in clinics and biomechanics to analyze clinical and medical engineering data (26, 27). The visualization of the branches embedded in the parenchyma was attributed to the good suppression of renal parenchyma signal using an inversion-recovery pre-pulse. This suppression also increased the maximum visible vessel length in TrueFISP MRA images compared with that in CE-MRA images. These findings are consistent with those of other investigations of renal arteries with respiratory-gated acquisition (24, 65, 88).

TrueFISP may avoid overestimation of RAS. In this study, there were 10 segments of renal arteries where the measured stenotic degree was greater in the images from CE-MRA than those from TrueFISP MRA, and 5 false-positive results from CE-MRA. This might result from several reasons such as insufficient concentration of contrast, dephasing effect in the stenotic segment or poor breath-holding of patients. It is very important for clinicians to make a correct decision before treatment of the patients with RAS according to the real condition of renal arteries. The results of our study indicated that free-breathing TrueFISP MRA can reliably depict the renal arteries in patients suspected of having RAS. Furthermore, it does not need patients to hold their breath, especially for the patients who are difficult to do so for CE-MRA scanning.

Previous studies have shown that the image quality of CE-MRA is significantly better than that of steady-state free precession MRA in all segments of renal arteries (65, 88).

However, results of the present study demonstrated that there was no statistically significant difference in image quality for proximal segment of main renal artery. The image quality of TrueFISP was found better than that of CE-MRA for VR and MIP images, middle and distal segments of the main renal arteries, and their first branches. Further studies with larger sample size are warranted to confirm this finding. Moreover, success of CE-MRA technique in demonstration of RAS depends on an exact scanning phase at the time of the peak intensity of contrast so as to avoid renal parenchyma and veins being early enhanced. Accurate detection of renal artery branches is important when trying to identify diseases that affect the segmental renal arteries, especially in cases of FD, which tends to affect females who are between 15 and 50 years of age (8) , frequently involving the distal segments of the main renal artery and its branches. It may be difficult for CE-MRA to display the distal stenotic part in FD.

Several limitations exist in our study. First, compared with CE-MRA coverage, the longitudinal scanning coverage of blood vessels in the images from TrueFISP MRA was shorter than CE-MRA. Second, the study population was small, especially the number of patients with RAS. In addition, no DSA data was referenced. Finally, no other clinical conditions, such as accessory renal artery or aneurysm, were analyzed in this study.

3.5 Conclusions

In conclusion, non-contrast TrueFISP MRA is a reliable method for evaluating renal artery disease and it demonstrates comparable or even better image quality than CE-MRA for diagnosis of RAS with no use of contrast material. It is an excellent alternative for

assessing renal arteries in patients with suspected secondary hypertension in certain clinical scenarios, such as renal insufficiency.

Chapter 4

Hemodynamic Computational Fluid Dynamic Techniques and Their Application in Renal Artery

Summary

This chapter provides the techniques of computational fluid dynamics, including blood flow model, processing, convergence criteria, post-processing and its application in renal artery hemodynamics analyzing.

4.1 Introduction

Computational fluid dynamics (CFD) has been utilized in a lot of industry applications, such as turbine machine, airplane industry, and aerospace, etc., and has acquired an extensive progress to improve the design and performance. In the area of biomedical engineering, CFD technology has been utilized in such areas: diagnosis and personalized medicine (90), drug delivery systems (91), performance of medical devices (92), and physiological modeling (93). Presently, CFD has evolved as one important research area in vascular hemodynamic clinical application and enable to provide numerous solutions of blood flow by solving the three-dimensional moment equations.

In disease states such as atherosclerosis, remodeling of walls of arteries leads to increased stiffness, with a resultant increase in flow resistance and arterial blood pressure. Atherosclerosis also causes a buildup of plaque in the walls of certain arteries. This decreases the cross-sectional area that is available for flow (stenosis), causes a local increase in flow resistance, and leads to blood flow lower than normal flow or absence of flow (ischemia). If this occurs in renal arteries, it can result in resistant renovascular hypertension. The patients will be suggested to perform either angioplasty or bypass operation to improve their renal artery hemodynamic conditions. CFD is suggested to be a useful tool to provide the diagnostic information, such as velocity, pressure difference and WSS, to assist clinicians to make a treatment decision.

CFD technology provides significant advantages such as time saving, low costs and effectiveness. And it might be a potentially important tool to evaluate blood pressure and estimate the function of kidney.

4.2 CFD Technology Application in Hemodynamics

4.2.1 Blood flow model and numerical simulation scheme

4.2.1.1 Governing equations

The Navier-Stokes equations are the conservative equations governing fluid motion. They consist of mathematical descriptions of conservation of mass, conservation of momentum and conservation of energy. When the flow is considered isothermal and incompressible, the energy conservation law is not included in the equations.

Conservation of mass indicates that the mass in a closed system remains constant over time,

$$\frac{\partial \rho}{\partial t} + \frac{\partial}{\partial x_j}(\rho u_j) = 0 \qquad (2)$$

Where ρ is the density of fluid; t means time; X_j is the Cartesian coordinate axis of x, y and z presenting space; and u_j is the velocity component (u, v and w). However, for incompressible flow where ρ is constant, the continuity equation is as follows:

$$\frac{\partial u_j}{\partial x_j} = 0 \qquad (3)$$

Conservation of momentum is derived by applying Newton's 2nd law of motion to a fluid element, which states that the changing rate of the momentum element is equal to the net external force acting on the element. Therefore, by assuming an individual fluid element (Lagrangian reference frame), the time changing rate of momentum for the fluid element is

$$\rho\left(\frac{\partial u_i}{\partial t} + u_j\frac{\partial u_i}{\partial x_j}\right) = -\frac{\partial P}{\partial x_i} + \frac{\partial \tau_{ij}}{\partial x_j} + \rho f_i \qquad (4)$$

Where u_i and u_j are the velocity components in the directions of i and j, respectively; τ_{ij} is the total stress; and f_j is a body force component in the i direction; and P is the pressure.

Simple model to solve Navier-Stokes equation is to consider blood as a Newtonian fluid in which the stress-strain curve is linear and passes through the origin. The constant of proportionality is known as the viscosity (μ).

$$\tau = \mu\frac{\partial u}{\partial y} \qquad (5)$$

Where τ is the shear stress exerted by the fluid [Pa], μ is the fluid viscosity (a constant of proportionality) [Pa s], $\frac{\partial u}{\partial y}$ or shear rate is the velocity gradient perpendicular to the direction of shear [s-1].

Therefore, the Navier-Stokes equation for an incompressible, Newtonian fluid simplifies to

$$\underbrace{\frac{\partial u}{\partial t}}_{\substack{\text{Unsteady}\\ \text{acceleration}}} + \underbrace{u\cdot\nabla u}_{\substack{\text{convective}\\ \text{acceleration}}} = \underbrace{-\frac{1}{\rho}\nabla p}_{\substack{\text{pressure}\\ \text{gradient}}} + \underbrace{\nu\cdot\nabla^2 u}_{\substack{\text{viscous}\\ \text{term}}} + \underbrace{f}_{\substack{\text{body}\\ \text{force}}} \qquad (6)$$

Typical values of density and dynamic viscosity (v) of 1060 kg/m^3 and 0.0035 Pa s were considered for blood (94) in this study respectively.

4.2.1.2 Discretization scheme

Because of non-linear, second-order, partial-difference for the Navier-Stokes equation, precise solution is not possible to be obtained by using current mathematic methods. Therefore, discretization schemes have been proposed to perform numerical calculation to solve the Navier-Stokes equation. The Finite Volume Method (FVM), which is one of the mostly used discretization methods for CFD simulation, directly discretises the integral form of the conservation laws. This method can be applied to both structured and unstructured grids that are used in most commercial software. FVM analysis includes (95): dividing the flow domain into small volumes or elements, integrating the transport equations over these control volumes, discretizing the partial derivatives to obtain an algebraic system, and solving the algebraic equations by means of an iterative numerical method.

To illustrate the FVM methodology, the conservation of mass and momentum equations are expressed in priority in Cartesian coordinates:

$$\frac{\partial u_j}{\partial x_j} = 0 \qquad (7)$$

$$\rho\left(\frac{\partial u_i}{\partial t} + \frac{\partial u_j u_i}{\partial x_j}\right) = -\frac{\partial P}{\partial x_i} + \frac{\partial}{\partial x_j}\left(\mu\left(\frac{\partial u_i}{\partial x_j} + \frac{\partial u_j}{\partial x_i}\right)\right) \qquad (8)$$

By integrating over each control volume and applying the Gauss' Divergence Theorem, the above equations can be expressed as:

$$\int_s \ u_j dn_j = 0 \qquad (9)$$

$$\frac{d}{dt}\int_v \ \rho u_i dV + \int_S \ \rho u_j \, u_i dn_j = -\int_s \ P dn_j + \int_s \ \mu\left(\frac{\partial u_i}{\partial x_j} + \frac{\partial u_j}{\partial x_i}\right) dn_j \quad (10)$$

Where V and S represent volume and surface regions of integration; and dnj is the differential Cartesian components of the outward normal surface vector.

In this study, after integrating conservation laws, the high resolution scheme which is a second order bounded differencing scheme for the convective terms was selected for discretization.

4.2.2 Medical image segmentation

Image segmentation is the process of partitioning a digital image into three-dimensional geometry. It is typically used to locate objects and boundaries (lines, curves, etc.) in images. More precisely, image segmentation is the process of assigning a label to every pixel in an image such that pixels with the same label share certain characteristics. Image segmentation could be used for object recognition, occlusion boundary estimation within motion or stereo systems, image compression, image editing, or image database look-up. There are many different practical applications of medical image segmentation, including: study of anatomical structure, locate tumors and other pathologies, measure tissue volumes and surgery simulation.

Several algorithms and techniques have been developed for image segmentation as follows.

1) Thresholding method: Thresholding method is the simplest and most commonly used method of image segmentation. This method is based on a threshold value to turn a gray-scale image into a binary image. The key of this method is to select the threshold value (or values when multiple-levels are selected). Several popular methods are used in industry including the maximum entropy method, Otsu's method (maximum variance), and k-means clustering. However, for thresholding CTA or MRA images, the key idea is that, unlike Otsu's method, the thresholds are derived from the plane DICOM image. This method suggested the usage of multi-dimensional fuzzy rule-based non-linear thresholds. In these works decision over each pixel's membership to a segment is based on multi-dimensional rules derived from fuzzy logic and evolutionary algorithms based on image lighting environment and application.

2) Color-based Segmentation: The general term clustering refers to a number of different methods. We will look at several different types of clustering algorithms that have been found useful in image segmentation. One of these methods is called K-means clustering. The K-means algorithm is an iterative technique that is used to partition an image into K clusters. K can be selected manually, randomly, or by a heuristic. This algorithm is guaranteed to converge, but it may not return the optimal solution. The quality of the solution depends on the initial set of clusters and the value of K.

3) Region growing methods: Region growing methods rely mainly on the assumption that the neighboring pixels within one region have similar values. The common procedure is to compare one pixel with its neighbors. If a similarity criterion is satisfied, the pixel can be set to belong to the cluster as one or more of its neighbors. The region grower begins at one position in the image and attempts to grow each region until the pixels being compared are too dissimilar to the region to add them. Usually a statistical test is performed to decide if this is the case.

4.2.3 Mesh generation

To generate the mesh for the model geometry, three key factors need to be considered: quality, size and element types. The mesh quality is one of the key important issues to maintain the accuracy for CFD simulation. And fine mesh usually requires a large computer memory and is associated with greater computational cost for analyzing. Therefore, the mesh size should be carefully selected to guarantee the quality of simulation and reasonable computational costs.

4.2.4 Definition of fluid properties

4.2.4.1 Newtonian and non-Newtonian models of blood

A Newtonian fluid is a fluid with a linear relation between stress and rate of strain and passes through the origin. When the dynamic viscosity depends on shear rate, the fluid is called non-Newtonian. The non-Newtonian behavior is seen in fluids which contains large particles, in case of blood, a suspension of erythrocytes, leukocytes, and platelets in blood

plasma. Blood plasma itself is a suspension of molecular organic/inorganic substances and macromolecules (fibrinogen, immunoglobulin, albumins, and lipoproteins) in an electrolyte solution which can be considered to behave as a Newtonian fluid (Nichols W, O'Rourke M. McDonald's blood flow in arteries: Theoretical, experimental and clinical principles. Hodder Arnold Publishers, 2005). Thus, blood should be considered as a non-Newtonian fluid in two conditions of very low shear rates or very small vessels (diameter <0.1 mm) (96). In studies of cerebral aneurysms with large vessels (diameter >0.5mm), the non-Newtonian behavior of blood is neglected by many researches (97-100). Valencia et al. studied a patient-specific carotid artery model with a saccular aneurysm under both Newtonian and non-Newtonian blood model conditions by using the Herschel-Bulkley model. No differences were found in temporal variations of WSS obtained from the two models. The types of blood models affect the prediction of velocity, pressure and WSS distribution only in the region with high velocity. Therefore, it was concluded that using the Newtonian blood model for cerebrovascular hemodynamic investigation was assumed to be acceptable (101). Another publication concluded that there was only 3% difference between these two models when the time averaged WSS was calculated (102). All of above studies suggested that the assumption of Newtonian flow model was suitable for cardiovascular and cerebrovascular CFD simulations (103).

The viscosity measurement of blood can be affected by temperature, hematocrit and other specific pathological condition of the blood donors. To determine the specification of the viscosity model, selecting the correct rheological behavior of blood is also important (104).

However, it is almost impossible to measure the viscosity from each patient case by case. It has been well known as the limitation in vascular hemodynamic research.

4.2.4.2 Fully developed flow

The effect of Womersley and flat (plug) profile boundary conditions on flow development was investigated by previous publications (27, 105). Despite the difference of inflow assumptions at the inlet, the results showed that the velocity profile close to domain is relatively similar for all boundary conditions (105). To ensure fully developed flow before and after renal artery in the current study, the inlet was extended 15 times length and all outlet branches at the distal ends were extruded to 40 times of the vessel renal artery diameter size in the normal downstream direction, to assure sufficient for the pressure recovery (27).

4.2.4.3 Steady state or pulsatile analysis

Experimental study conducted by Liou et al. (106) to investigate the effect of bifurcation angle at two different flow conditions showed that the steady flow could adequately simulate the flow pattern in cerebral aneurysms. However, there were some differences related to fluctuation amplitude and the region affected by maximum fluctuation between pulsatile and steady flow studies (106). Mantha et al. investigated the effect of blood flow pulsatility in 3 sidewall and 3 bifurcation aneurysms and concluded that in many cases, steady state flow analysis can provide reasonable information on cerebrovascular flow in addition to be faster and time-independent (107).

4.2.5 Boundary conditions

Correct definition of boundary conditions is one of the important issues in CFD analysis to obtain accurate results.

4.2.5.1 Rigid wall boundary assumption

Regarding the vascular wall condition, it was always discussed in previous publications. A comparative study using the technology of fluid and solid interface (FSI) has indicated that only 1% difference in wall shear stress was calculated in comparison with elastic model and rigid model (108).

Due to the limitation of information about renal artery wall displacement in this study, rigid wall condition was assumed on vessel surfaces.

4.2.5.2 Inflow boundary condition

The physiological flow condition is the main parameter used to set up the CFD simulation. Hence, the methods of inflow boundary conditions used by previous studies can be categorized as follows:

1) Healthy subjects (PC-MRA): flow rates were measured at the renal artery inlet area by integration of the measured velocity profile over the vessel cross section manually or using the threshold segmentation of the magnitude images, the time-dependent flow rates are obtained. The flow rate curve is decomposed into Fourier modes (97)

$$Q(t) = \sum_{n=0}^{N} Q_n \, e^{in\omega t} \qquad (11)$$

Where ω is the angular frequency from the period of cardiac cycle, N is the number of modes. Thus, the velocity profile can be computed from the Womersley solution

$$v(r,t) = \frac{2Q_0}{\pi R^2}\left[1 - \left(\frac{r}{R}\right)\right] + \sum_{n=1}^{N} \frac{Q_n}{\pi R^2}\left[\frac{1 - \frac{J_0\left(\frac{\beta_n r}{R}\right)}{J_0(\beta_n)}}{1 - \frac{2J_1(\beta_n)}{\beta_n J_0(\beta_n)}}\right] e^{in\omega t} \qquad (12)$$

Where R is the radius of artery, r is the cylindrical coordinate, J_0 and J_1 are the Bessel function of the first kind of order 0 and 1, respectively and α_n is the Womersley parameter of order n as follows:

$$\beta_n = i^{3/2}\alpha_n = i^{3/2} R \sqrt{\frac{n\omega}{v}} \qquad (13)$$

Where v is the dynamic viscosity.

2) Patient-specific (PC-MRA): flow rates were measured from PC-MRA of patients being examined (109-111).

3) Healthy subject (TCD): a velocity profile was simulated with the typical velocity obtained by Doppler ultrasound (D-US) and computed from the Womersley solution (112, 113).

4) Healthy subjects (scaled): the flow waveform was scaled according to the cross-sectional area of the inflow vessels (98, 114, 115).

5) Pressure waveform: the pressure pulse was applied at the inlet boundary condition (116).

In addition to the uncertainty regarding the physiological value of inflow at the abdominal aorta, inflow boundary condition sensitivities have also been investigated from different aspects in the literature as are summarized below:

1) Inlet velocity profile: Myers et al. (117) studied a patient-specific right coronary artery (RCA) under steady and pulsatile flow conditions in following conditions: 1) a fully developed inlet velocity profile; 2) a "blunt" inlet velocity profile, with constant axial velocity component; 3) a fully developed Dean-type velocity profile. The ratio of the effective centrifugal inertial forces to the viscous forces is called Dean-number (D), which is used to evaluate the fully developed flow in curved tubes and is given by using $D = Re\sqrt{\frac{r}{R}}$, where Re is the Reynolds number, r is the radius of the lumen along the line of the radius of curvature and R is the radius of curvature of the arch. The comparative analysis showed that the arterial velocity and WSS did not change significantly with variation of the inlet velocity profiles. Therefore, they suggested that the geometry effects are more dominant than the inlet velocity profiles (118).

   Oshima et al. (119) studied the velocity field of the curved pipe model by setting up PIV experiment and CFD simulation. Good agreement was found between numerical and experimental results. The results showed that the vortex structure is associated with the Reynolds numbers. They simulated one patient-specific cerebral aneurysm by applying an inflow with and without secondary flow obtained from curved pipe model.

Differences between velocity and WSS distribution obtained from both types of inflow suggested that the influence of the secondary inflow boundary condition should be considered in simulations (119). Myers et al. continued this work by generating the secondary flow inlet profiles using long entrance lengths with curvature and helical pitch in 3 carotid bifurcations. They found that the effect of secondary flow on hemodynamic parameters of WSS and OSI is 3.5 times less than the effect of geometry variations (13% vs 48%). Thus, it was concluded that applying the fully developed Womersley inflow to the sufficient entrance length of patient-specific model is a reasonable assumption (120).

2) Inflow parameters and flow distribution: Sensitivity of patient-specific models with a cerebral aneurysm to the variable inflow parameters and flow distribution was studied by Venugopal et al. (115) using an anatomically cerebral aneurysm model. One pulsation cycle with fixed time step was selected while heart and blood flow rates as well as the distribution of flow rates in the A1 segments of the anterior cerebral artery were varied over physiological ranges. They found that although there is a linear relation between the inflow Reynolds number and the shear stress in the parent arteries, the nonlinear effects were observed for intra-aneurysmal flow. The results indicated that the shear stress distribution is not sensitive to the heart rate changes despite a significant dependency on blood flow rate alteration and flow rate distribution in the feeding arteries.

3) Inflow type: Marzo et al. (105) studied the influence of inflow type (Womersley and flat (plug) profile) on hemodynamics at three locations. The results of this

comparative study reported that there is no significant difference in qualitative flow patterns obtained from both types of inflow (less than 5%) compared with the other uncertainties in the analysis such as segmentation or patient-specific flow measurements.

4) Normal or patient-specific wave form: Karmonik et al. (121) conducted a comparative study between one idealized normal subject waveform and patient-specific flow measurement using 2D PC-MRA. Significant differences were found between the temporal variation of the WSS of the cerebral aneurysms using idealized and patient-specific waveforms. Thus, special care is essential to quantify results obtained from different waveforms.

4.2.5.3 Outflow boundary condition

To model the flow exit from the normal or stenotic renal arteries, outflow boundary conditions were assigned to the outlet face zones. According to the literature, Dirichlet boundary conditions are also prescribed for the outlets. However, due to lack of access to patient-specific flow measurements, different assumptions were considered to define the magnitude of outflows. Assumptions involved in imposing outflow boundary conditions can be basically categorized with two major groups of traction free (pressure equal to zero) and flow distributions.

1) Traction free boundary condition (pressure=0) is based on the assumption that the flow divisions among the branches are associated with the geometry and cross

section area (97) while the impedance of the distal arterial tree determines the flow divisions.

2) The Windkessel models of the arterial network (122) describe basic properties of vascular bed by assuming the pressure, flow rate and flow resistance as the voltage, current and resistance in an electric circuit. To determine the pressure at outlets the following equation is integrated:

$$Q(t) = C\frac{dp(t)}{dt} + \frac{P(t)}{R} \qquad (14)$$

Where $Q(t)$ is the flow rate, R is the resistance of distal arterial network and C is the compliance of the artery. For a healthy subject, the parameters (C and R) are estimated based on the standard range of blood pressure (80 mmHg to 120 mmHg).

Comparative study of the infundibulum of a patient with three outflow boundary conditions of traction free and two types of the Windkessel models reported that qualitative distributions of WSS and pressure are the same except near the region close to the outlets and at the top of the infundibulum (123). So when no information is available regarding flow measurement at branches and outlets, the traction free boundary condition assumption was considered in most previous studies (97, 109, 112, 113, 124-129).

4.2.6 Convergence Criteria

The residual as applied to each discretized equation of the system is a measure of the local imbalance of each equation that becomes negligible as the iterations increases. In CFD

simulation, a residual parameter can be used to monitor the behavior of the numerical process and to determine the convergence of the solution trend.

During the simulation, the iterations will stop at two points (whichever occurs first):

1) The maximum number of iterations that is mostly set to a very large number to ensure the iterations reaching to convergence criteria first.

2) If the convergence criteria is reached, either the convergence criteria can be chosen from the maximum normalized residuals (Max Res) or the root mean square (RMS) of the normalized residuals.

4.2.7 CFD results validation methods

CFD applying in patient-specific simulation for renal artery (130) and cerebral aneurysm (110) has been demonstrated to be a useful tool to provide information for assisting diagnosis and making therapeutic decision (110). However, it is lack of enough studies to confirm CFD results with in vivo validation by measuring patient flow conditions. It is still a challenge to promote CFD technology to be a reliable diagnosis tool for estimating the function of renal artery flow behavior.

Ford et al. in 2005 (131) introduced 3D X-ray angiography to validate CFD simulation results. The virtual angiographic images derived from an image-based CFD model of a giant aneurysm have been shown a good agreement with the corresponding clinical images when the contrast agent injections were properly selected.

Acevedo et al. (132) validated CFD analysis of patient-specific aneurysms by using in vitro (exact silicon phantom replica of the patient's aneurysm) and in vivo PC-MRA. A good agreement was obtained in the paper. The results represented the potential confidence to use CFD to simulate the giant size of cerebral aneurysm.

Another validation method is to use particle image velocimetry (PIV). One study presented by Ford et al. compared the velocity field in two realistic patient specific models of giant cerebral aneurysms which constructed of a silicone elastomer. The results demonstrated excellent agreement between the results of CFD simulations and PIV measurements in both gross flow patterns and their associated cycle-to-cycle variations. In addition, the PIV results were also validated by using MRI flow measurement (133). The study indicated that CFD simulation results can be matched with PIV.

Moreover, the technology of noninvasive estimation of renal artery model presented by Yim et al. (134) has been conceptually accepted. The technology has been estimated to be a potential tool to improve the capability for evaluation of renovascular disease. It may be possible to estimate the blood pressure alteration in various stenoses of renal artery by using the flow results together with medical images.

4.3 Introduction of CFD Application in Renal Artery

CFD technology has been introduced to investigate the hemodynamic parameters of renal artery. The simulations were carried out for cases of normal renal artery and pathological

changed- stenotic models to virtually evaluating the hemodynamic changes of renal artery in renovascular hypertension.

4.3.1 Patient-specific modelling

The images of patient-specific renal arteries used in the current study were acquired from Department of Diagnostic Radiology, Shanghai Zhongshan Hospital, Shanghai Medical College of Fudan University. The study has been approved by both Shanghai Zhongshan Hospital (Ethic Approval No.: B2012-095) and Macquarie University Ethics Committee (Ethics Ref: 5201300448). DICOM format clinical MR images were obtained using a 1.5T MR imager (MAGNETOM Aera, software version syngo MR D11; Siemens Healthcare, Erlangen, Germany).

The definition of renal artery stenosis remains a controversial subject among researchers and interventional radiologists. In the current study, RAS degrees were defined as **Formula 1** (page 63) (130). Reference site was defined as the normal-looking portion of vessel presented in either distal or proximal to the lesion. The grading of stenosis was performed using an electronic caliper to measure the minimum luminal diameter at the optimal projection angle along the vessel axial image.

Two medical visualization software packages, Real INTAGE® (Cybernet, Tokyo, Japan) and Mimics® (Version 14.0, Materialise Company, Leuven, Belgium) were used to convert medical DICOM images into 3D angiography. To create the geometry required for simulation of renal arteries, unrelated arteries and branches were segmented from the

images. Due to high sensitivity of renal artery hemodynamics to the segmentation of the abdominal aorta and for comparison reason, the similar lengths of each artery branches were selected for each patient in order to be able to relatively compare hemodynamic parameters among patients. The geometry data was exported as STL format, and transferred into ICEM (ANSYS, Inc) for mesh generation.

Pre-processing of CFD simulation consists of the following three steps (95) (Figure 6):

1) Patient images segmentation (Figure 7 and Figure 8);
2) Mesh generation;
3) Assigning boundary conditions and defining fluid properties.

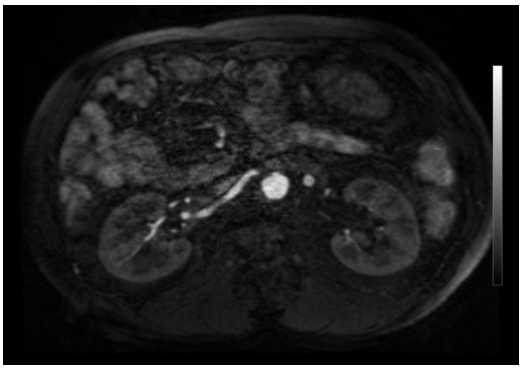

Primary 2D images →

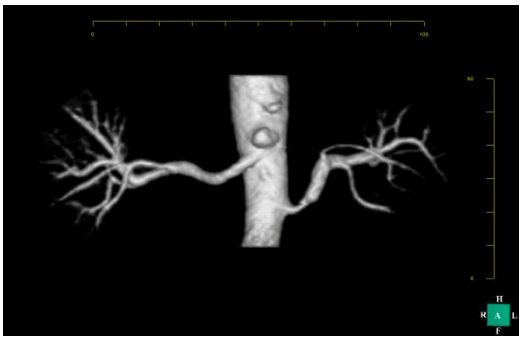

3D angiography →

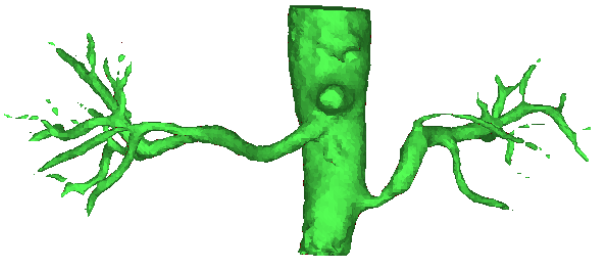

3D geometry STL data →

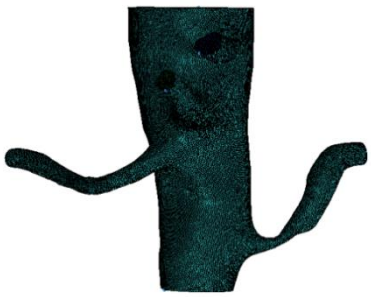

Mesh generated model

Figure 6. Patient-specific modelling process from MRA to mesh generation

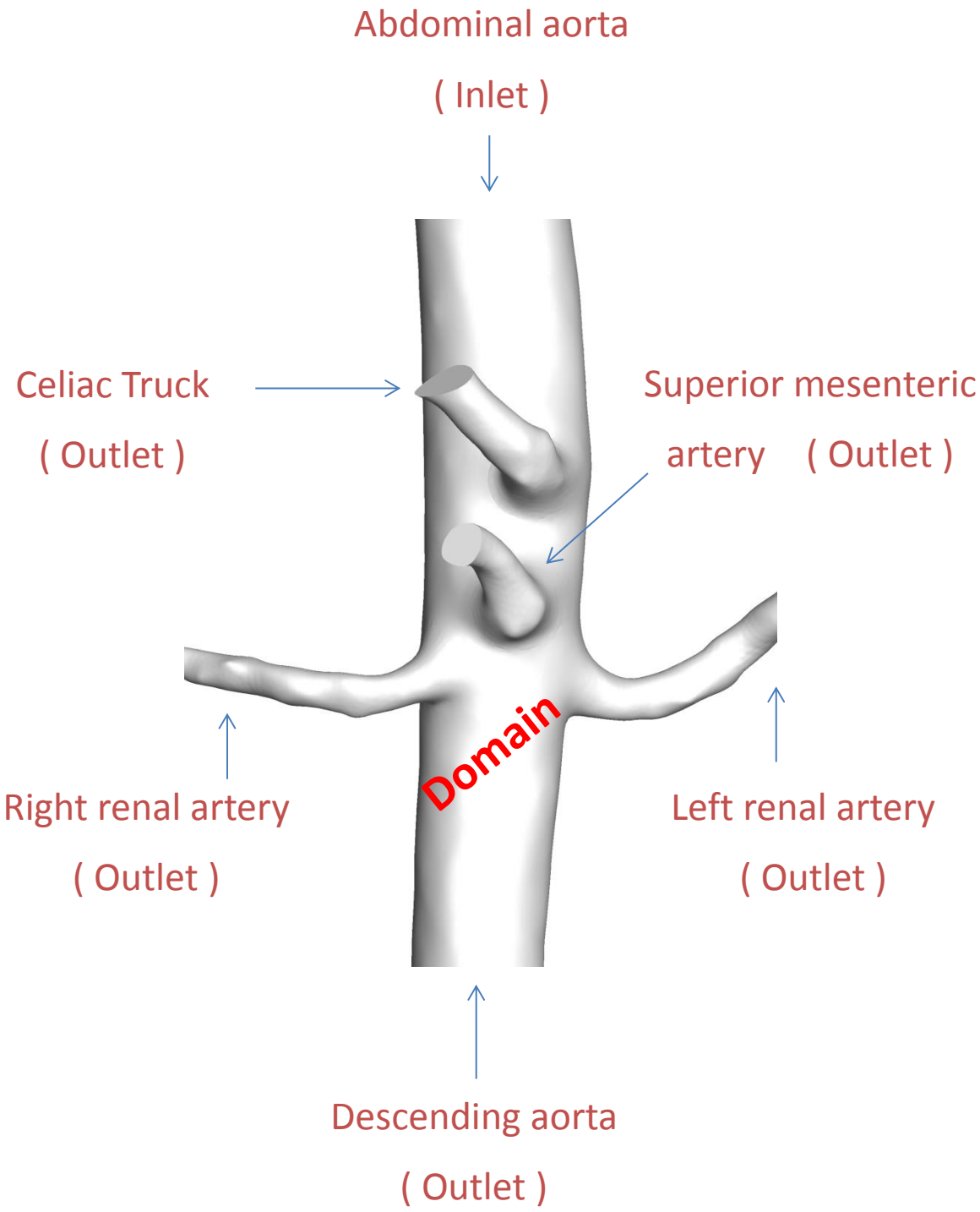

Figure 7. Inlet and outlets names of renal artery fluid domain

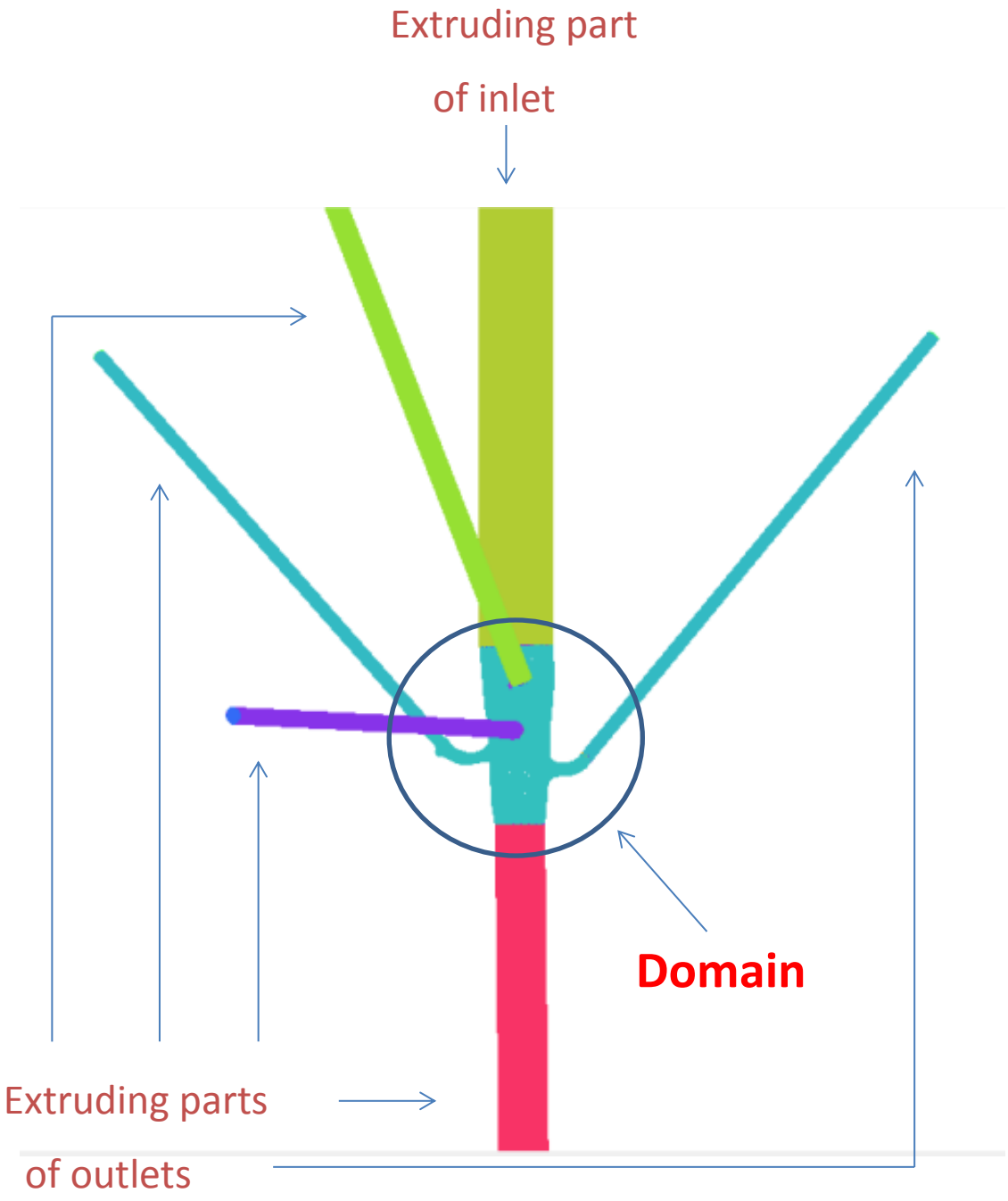

Figure 8. Renal artery fluid domain with extruding parts of inlet and outlets

4.3.2 Patient images segmentation

In this study, three types of renal artery models (normal, stenosis and virtually stent-treated model) were created using MIMICS (Version 14.0, Materialise Company, Leuven, Belgium) (Figure 9 and Figure 10).

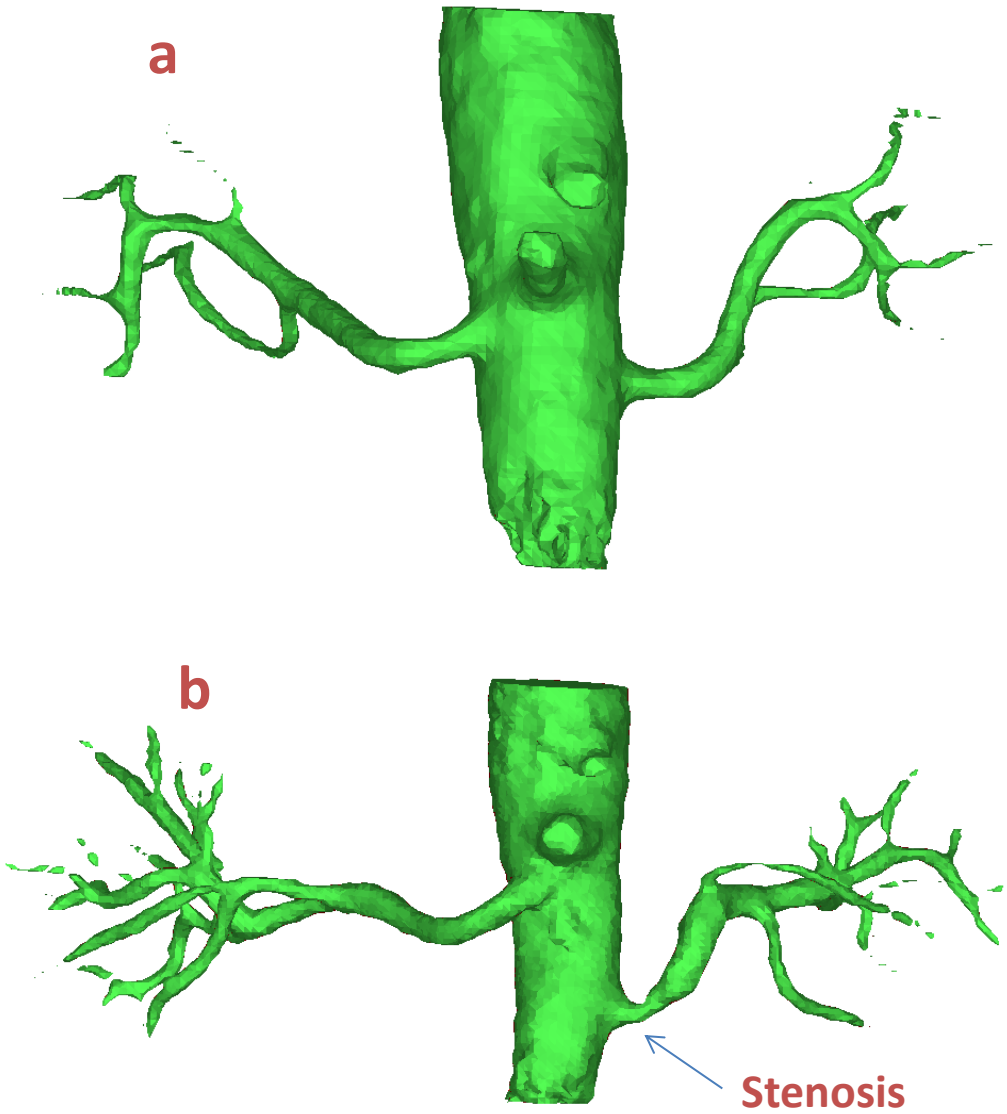

Figure 9. Two types of idealized renal arteries from 2 patients: (a) normal renal artery; (b) renal artery stenosis

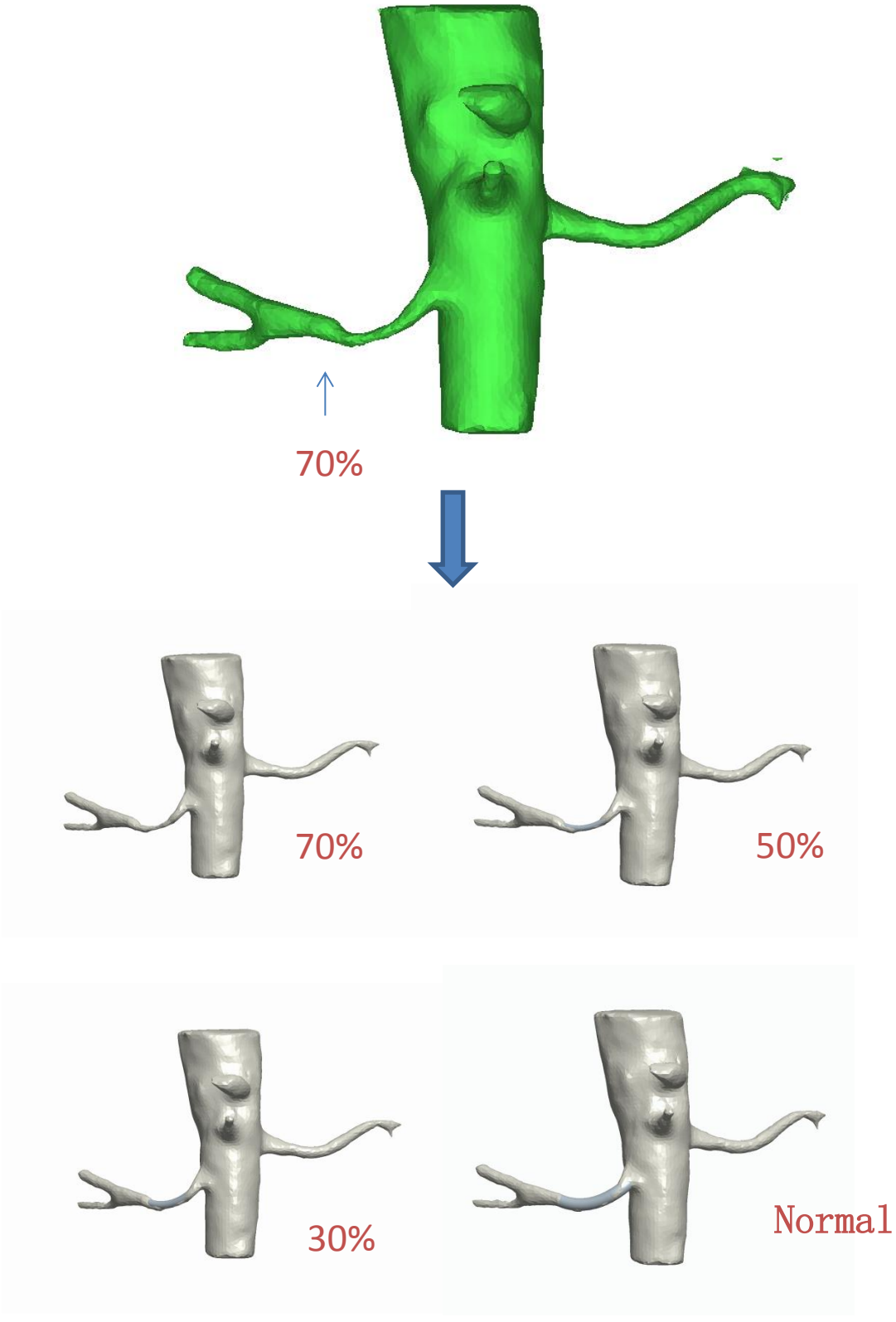

Figure 10. Primary stenotic degree 70% of one patient. Different modified models mimicking different degree stents (as shown 70%, 50%, 30 % and non-stenosis), the three-dimensional STL formatted artery surface data was utilized to form grid for CFD simulation

Different configuration of abdominal arteries and renal arteries along with main branches from the above geometries (fluid domain) were created and discussed.

4.3.3 Mesh generation

In current study, ICEM (ANSYS 15.0, Lebanon, NH, USA) blocking method is difficult to create the arbitrary surface of renal artery. Therefore, an unstructured tetrahedral grid was selected for all geometries and prismatic mesh applied at the boundary layer.

The mesh independent study was performed by using different discretization on single renal artery model with mesh size from 2060198 to 3608948 elements. The hemodynamic parameters have been observed to be stable. The fine mesh size was considered well enough for CFD simulation of this study.

To accurately calculate the hemodynamic parameters from artery surface, three prismatic layers were generated with an average nodal space increasingly by a ratio of 1.2 at gradient distances, gradually moving them away from the vessel to handle the boundary layer efficiently. The distance of the first layer to the vessel surface was fixed at 0.02 mm. ANSYS CFX 15.0 (Lebanon, NH, USA) was used to perform CFD simulations. The image of meshes of one model was shown in Figure 11.

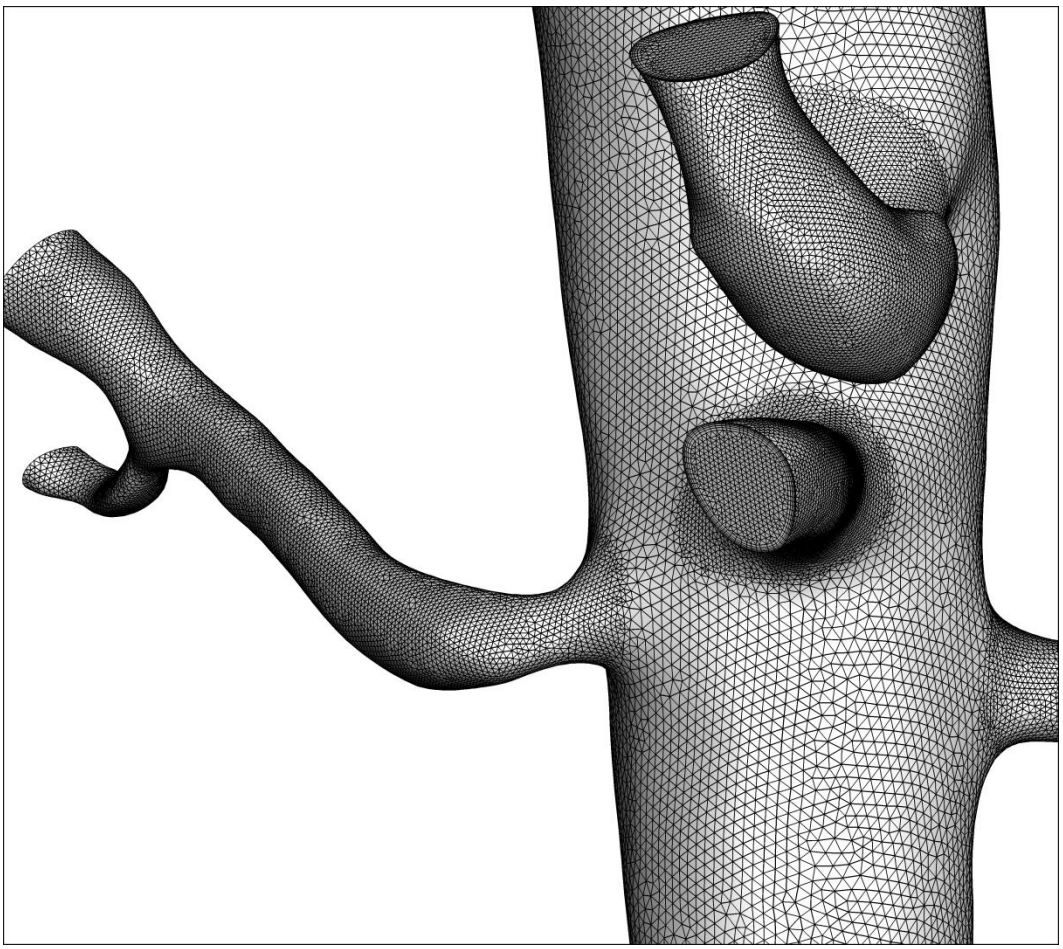

Figure 11. Geometric mesh of one model

4.3.4 Assigning boundary conditions and definition of fluid properties

Under resting conditions, approximately 70% of the heart output (around 5000 ml) that enters the descending aorta is extracted by celiac truck, superior mesenteric artery, and renal arteries; and the majority of the remaining 30% flows down the infra-renal segment (34). However, it is not possible to measure patient real individual conditions of blood flow in aorta. According to the flow ratios, an average abdominal aortic blood flow rate of 3500 ml/min (5000ml×70%=3500ml) was introduced at the extended aortic inlet boundary as the inlet boundary condition in this study. In order to avoid the indefinite outflow condition, this study recounted the relatively compared results of different renal artery stenosis. The traction free boundary condition (pressure=0) was applied for the simulation of left and right renal arteries.

Since previous research has confirmed that the instant blood pressure results from pulsatile flow simulation could proportionally represent those of the steady-state flow simulation (135). Therefore, steady-state flow simulation was selected for this study.

Blood model in this study was assumed to be Newtonian and incompressible in this study.

In this study, due to the high sensitivity of pressure difference and energy loss, the Max Res of 10^{-5} was selected for all simulations as the residual target test. The validation tests indicated that the results tended to be less than 1% alteration of energy loss (EL) calculated with residual target 10^{-5} and 10^{-6}.

4.3.5 Post-processing

It has been recognized that hemodynamic factors play an important role in vascular biology and in the localization and development of atherosclerotic lesions. Renal artery velocity profiles have been evaluated by PC-MRA and D-US (136, 137).

Three hemodynamic parameters were assessed by using CFD simulation in this study, including maximum velocity, mass flow rate and pressure difference. WSS, which may be significantly related to the formation of aneurysm and stenosis, will be discussed in the near future. The maximum velocity was measured at the most severe stenotic part of renal artery and compared with PSV from US results. Meanwhile, the volunteer velocity was calculated in the middle part of main renal artery. All MRF profiles were measured at the end of main renal arteries. Streamline contour was utilized to intuitively and reasonably show the flow of target vessel (Figure 12). The translesional PD was measured from the start of main renal artery to the end of stenosis, while, for normal volunteers, the PD was evaluated from the start to the end of main renal artery (Figure 13).

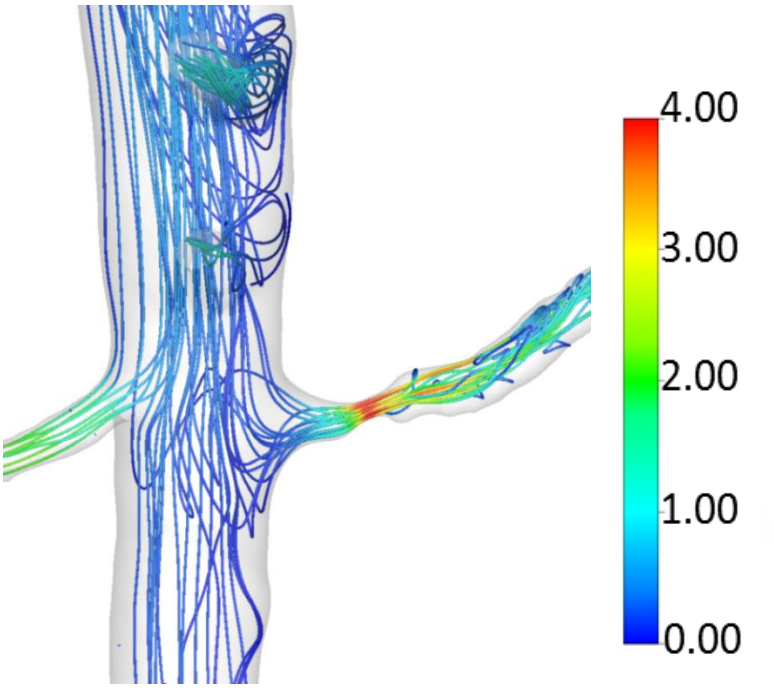

Figure 12. Streamline contour of one model (m/sec)

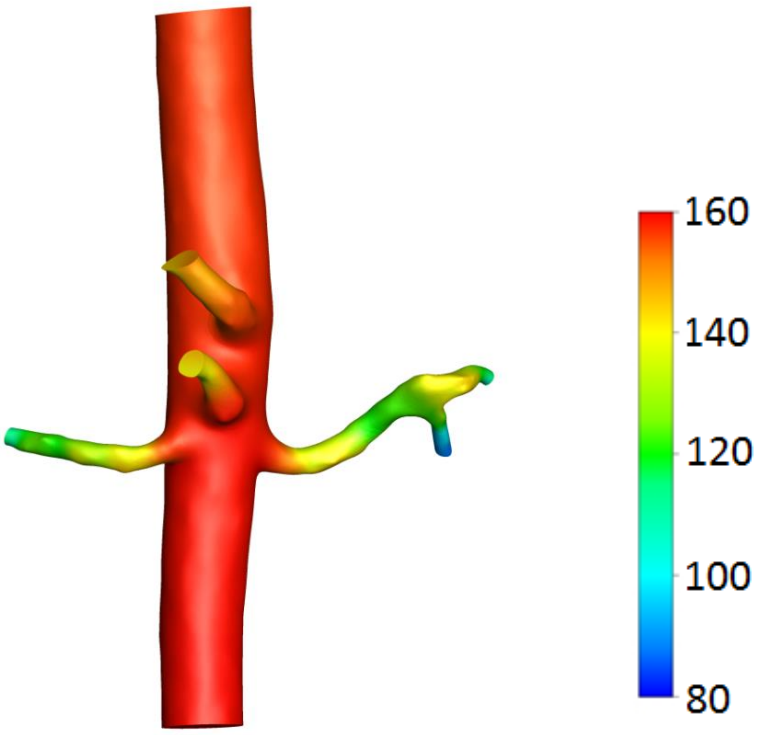

Figure 13. Pressure of one hypertensive model (mmHg)

Chapter 5

Hemodynamic Analysis of Renal Artery Stenosis using Computational Fluid Dynamics Technology Based on Non-Contrast Steady-State Free Precession MR Angiography

Published as

Weisheng Zhang, Yi Qian, Jiang Lin, Peng Lv, Kaavya Karunanithi, Mengsu Zeng. Hemodynamic analysis of renal artery stenosis using computational fluid dynamics technology based on unenhanced steady-state free precession magnetic resonance angiography: preliminary results. International Journal of Cardiovascular Imaging, 2014, 30(2):367-375. (IF=2.322).

Summary

This chapter reports the study on hemodynamics of stenotic renal artery. The image data used in this study are acquired using non-contrast MR angiography technique. Then patient-specific models are virtually manipulated. Pressure difference (PD), velocity and mass flow rate (MFR) at various renal artery stenotic grades are analyzed. The simulation results are compared with clinical data measured using Doppler ultrasound.

5.1 Introduction

Renal artery stenosis (RAS) is the cause of renovascular hypertension in approximately 1-5% of hypertensive patients (1, 2). The kidney responds to a decrease in blood flow of RAS by activation of the renin-angiotensin-aldosterone system that increases blood pressure and can result in severe refractory hypertension (3). Renal vascular diseases, including atherosclerotic arterial lesions, fibromuscular dysplasia, Takayasu arteritis, and so on, may lead to RAS. Furthermore, RAS exists in 40–50% of patients with occlusive disease of the lower extremities and 15–30% of patients with coronary artery disease (4). In addition, the prevalence of RAS in patients with end-stage renal disease is 10–22% (5, 6).

MRA is well suited for both the angiographic illustration of RAS and for assessment of its impact on renal artery flow using contrast-enhanced and phase-contrast (PC) techniques. Currently, newly developed non-contrast MRA technique, named steady-state free precession (SSFP), comes from the preparation of the imaging volume with a spatially selective inversion pulse, resulting in the suppression of stationary tissue and venous blood, allowing an excellent depiction of renal arteries with high contrast, and it has been accepted as an accurate method in visualization of renal artery (21-24).

On the other hand, patient-specific computational fluid dynamics (CFD) technology is one of the novel technologies to quantitatively estimate hemodynamics. It has been successfully applied in different aspects of cardiovascular system: intracranial and carotid artery (25-27), heart disease and coronary artery (28-30), aortic artery (31, 32), and pulmonary artery (33). To date, there are no reports to determine the hemodynamic

conditions of in vivo RAS using CFD technique although the computational method has been introduced to quantitatively characterize the hemodynamic conditions under simulated resting pulsatile flow conditions in an idealized model of an abdominal aorta (34).

In the current study, CFD based on non-contrast SSFP MRA was used to analyze the pressure difference (PD), velocity and mass flow rate (MFR) of different main renal artery stenoses.

5.2 Materials and Methods

5.2.1 Patients data

The study has been approved by the Institutional Ethics Committee of Shanghai Zhongshan Hospital of Fudan University (Shanghai, China) and the Macquarie University Human Research Ethics Committee (HREC (Medical Sciences)). From March 2012 through April 2013, 30 consecutive patients (22 male, 8 female; age range, 33-83 years; mean age, 59.8 ± 12.8 years; mean weight 75 ± 7.4 kg, mean systemic blood pressure 160.8 ± 22.6 mmHg) diagnosed with unilateral RAS, free from elevated serum creatinine and decreased estimated glomerular filtration rate, were prospectively enrolled in this study. Also 10 normal volunteers (6 male, 4 female; age range, 24-66 years; mean age ± standard deviation, 38.5 ±14.2 years) were recruited, scanned by non-contrast MRA, and processed using the same methods.

5.2.2 MRA examination

All patients and volunteers underwent MRA examinations with a 1.5T MR imager (MAGNETOM Aera, software version syngo MR D11; Siemens Healthcare, Erlangen, Germany) equipped with 2 body coils placed both at the front (18-element body matrix) and back (12-element spine matrix) of the abdomen. All patients were scanned in the supine and feet-first position with a belt fastened around the abdomen to reduce motion artifact. And a respiratory-gated navigator was placed at the lower level of the diaphragm to synchronize data readout to trigger SSFP scanning with free breathing.

After acquisition of the scout images, non-contrast SSFP MRA (syngo NATIVE TrueFISP; Siemens Medical Solution) was performed using a balanced steady-state gradient echo technique. The preparation of the imaging volume with a spatially selective inversion pulse was used to suppress signal from stationary tissues at the background and suppress signal from venous blood within the imaging volume. Depending on patient respiratory rhythm, inversion time and acquired number of imaging sections, the acquisition time ranged from 5 to 7 min (300-420 sec).

Sequence Parameters for SSFP MRA were set as follows: repetition time 1293.80 msec, echo time 1.49 msec, data acquisition time 300-420 sec, flip angle 90 degree, bandwidth 781 kHz, field of view 320mm×240 mm, section thickness 1.0-1.2 mm, No. of sections 64-80, spatial resolution 192X256 mm^2, accelerated factor 2, and inversion time 1200 msec.

5.2.3 US examination

Twelve of 30 patients underwent US (IU22, Philips Medical Systems, Netherlands). Color Doppler flow examination was performed by an ultrasonographer and peak systolic velocity (PSV) of stenotic main renal artery was obtained under resting conditions in 3 days after MRA examination.

5.2.4 CFD simulation methods (patient images segmentation, mesh generation, simulation methods and boundary conditions)

A commercial segmentation software Mimics (Version 14.0, Materialise Company, Leuven, Belgium) was utilized to transfer MRA images (DICOM format) into vessel-shaped three-dimensional geometric data (STL format). The STL artery surface data was meshed using ICEM (ANSYS, Lebanon, New Hampshire) to form grids for CFD simulation. The whole transfer system for RAS geometry generation is shown in Figure 14.

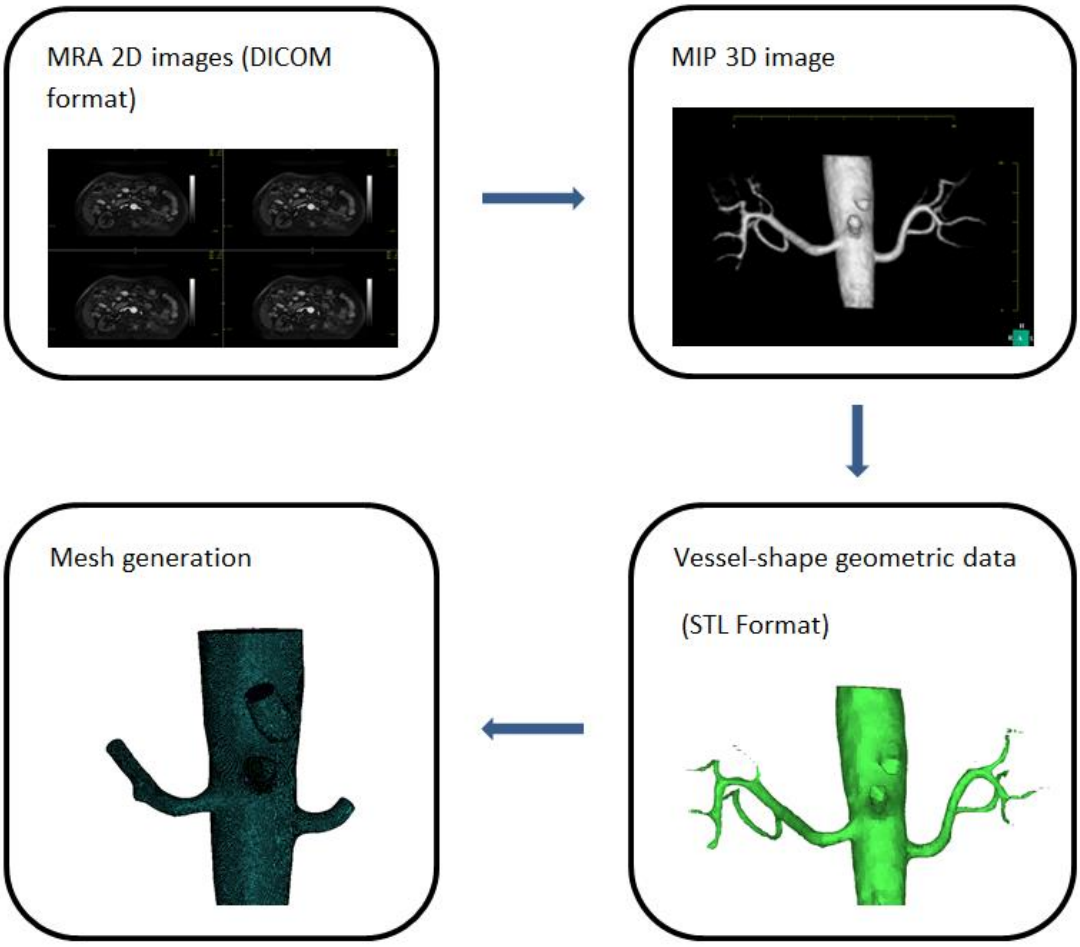

Figure 14. Data transfer system for RAS geometry generation. After acquiring MRA 2D images (upper left), the first step was to transform the DICOM format data to 3D image (upper right), then segmentation software-Mimics was used to transfer it to the STL format (lower right), and mesh grid (lower left) for CFD simulation was created using ICEM software

To accurately calculate the parameters from the surface of the vessel, we meshed 3 layers of growth mesh (prism mesh) at gradient distances, gradually moving them away from the vessel to handle the boundary layer efficiently. The distance of the first layer to the vessel surface was fixed at 0.02 mm. The number of elements in all patient-specific models ranged from 2060198 to 3608948. The process of segmentation and mesh generation took 5-10 minutes.

Flow entry and exit from the calculation domain were assumed to be normal to the inlet and outlet surface regions of the arterial geometry. To form a fully developed flow boundary layer at the proximal inlet, the inlet of the domain in an upstream direction was extended to 15 times the inlet diameter size so that fully developed velocities profiles were formed in the boundary layer. To simulate the peripheral capacitance, all outlets at the distal ends in the normal downstream direction were extruded to 40 times the vessel diameter size, sufficient for the recovery of blood pressure. These boundary conditions ensured that the length of the extended domain would not further influence the flow in the main-body domain. The mesh and boundary conditions were independently evaluated in previous validation processes (27). The extended domains at the inlet and outlets were only for the purpose of the simulation and were not included in the analysis of flow characteristics. The coarse mesh of the extended domain did not have any influence on the final results as they were solely designed for pressure recovery (27).

The vessel wall was assumed as rigid wall and the assumption of zero wall motion was utilized in calculations (26, 27, 34, 134). The fluid in this study was assumed as an

incompressible and Newtonian fluid, while the flow was assumed to be laminar flow. The density was set 1060 kg/m^3, and the dynamic viscosity was 0.0035 Pa.s (26, 27). Steady Navier-Stokes governing equations were solved by CFX (ANSYS v.15.0) on the basis of the finite volume method.

Steady state flow condition was introduced in order to reproduce the measured average volumetric rate and velocity data. One previous study (34) has investigated that the flow of cardiac cycle influenced by aorta was less than 10% of size. The protocol of patient enrolled standard in this study (Section 5.2.1) illustrated that all patients were selected at weight with less than 10% standard deviation, which reflected the similar estimated blood volume. Therefore, we assumed the inflow alteration at aorta would be at controllable range. As indicated in Section 4.3.4 of Chapter 4, an average abdominal aortic blood flow rate of 3500 ml/min was introduced as the inlet boundary condition. Zero relative gradient pressure in the flow direction was used at both left and right renal artery outlets at all times. All of the above boundary conditions ensured to meet the primary conditions of linear equations.

5.2.5 Evaluation of MRA images and CFD results

The data was analyzed jointly by two radiologists with 11 and 5 years of experience in cardiovascular imaging. Both readers were blinded to the patient clinical data and a consensus was reached for each patient. The readers were allowed to perform additional reconstructions, if necessary.

For qualitative assessment, image quality was based on the degree of whole-artery visualization, motion artifacts, and signal suppression of the background. The image quality of overall main renal artery MIP (Maximum intensity projection) images was graded by using a five-point scale: grade 4 indicated excellent (high homogeneous signal intensity within vessel lumen, optimal delineation of vessel border, no artifacts present); 3, good (good enhancement of vessel lumen, incomplete delineation of vessel border, some artifact may be present); 2, fair (low inhomogeneous signal intensity, incomplete delineation of vessel border, diagnostic evaluation possibly impaired); 1, poor (minimal enhancement, diagnostic evaluation hardly possible); and 0, non-diagnostic (no enhancement, non-diagnostic). An image quality score of 4 or 3 was defined as an acceptable image quality, and images with score 2-0 were excluded from further analysis.

Quantitative analysis was performed to determine diameter stenotic grades involving the main renal arteries. The extent of RAS was graded as follows: Grade 1 indicated less than 24% luminal narrowing; grade 2 (mild), 25%–49%; grade 3 (moderate), 50%–74%; grade 4 (severe), 75%–99%; and grade 5 (occlusion), 100%. Stenosis grading was performed by using an electronic caliper to measure the minimum luminal diameter at the optimal projection angle along the vessel axis. The percentage of stenosis was calculated as **Formula 1** (page 63).

Maximum flow velocity of renal arteries from CFD results were compared with PSV from US which was used as a reference standard in 12 patients. As for CFD results in patients, the translesional PD was measured from the start of main renal artery to the end of stenosis

(Figure. 15a), while the maximum velocity was measured at the most severe stenotic part (Figure. 15b). In normal volunteers, the PD was evaluated from the start to the end of main renal artery, while the velocity was calculated in the middle part of main renal artery. All MRF profiles were measured at the end of main renal arteries.

5.2.6 Statistical analysis methods

The maximum velocity measured using CFD was compared to PSV of US. Reliability was assessed using intraclass correlation coefficient; and Paired t test was used to measure statistically significant difference. For continuous variables, Paired t test and One-Way ANOVA (Fisher test) were applied to evaluate PD, velocity and MFR of various main renal artery stenoses and compare them with the control normal group. A two-tailed P value of 0.05 or less with 95% intervals was considered to indicate a significant difference. Statistical analysis was performed with the commercially available SPSS software (version 16.0; SPSS, Chicago, III).

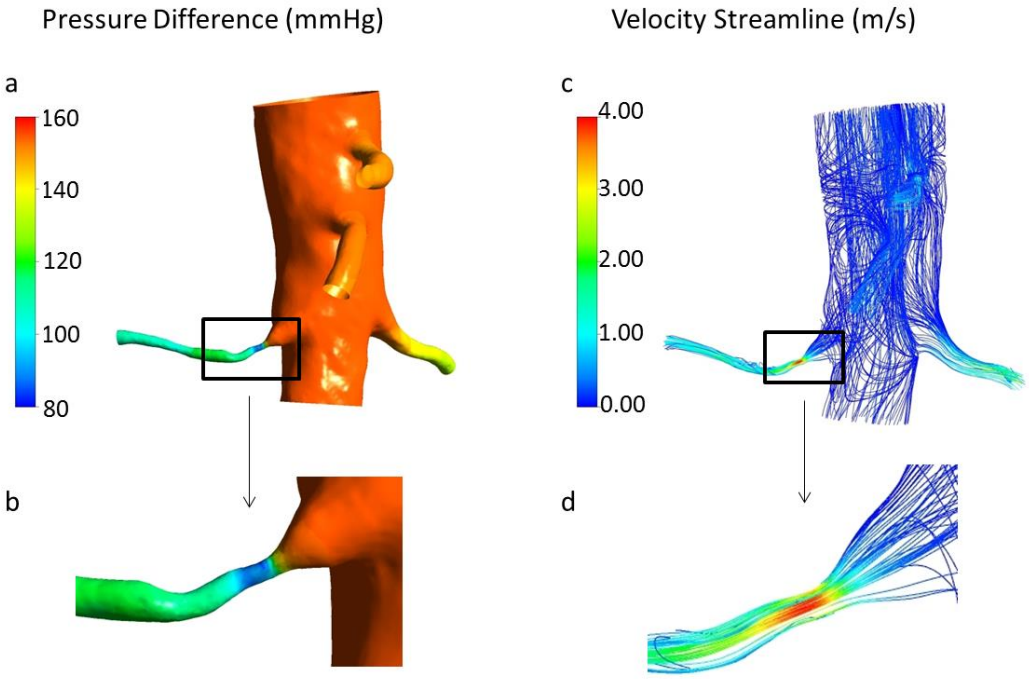

Figure 15. Detailed results of PD and velocity of a 67 years old male with hypertension and a diameter stenotic degree of 59.4% of the right main renal artery. (a) PD of the whole domain. (b) Translesional PD (mean 55.06mmHg) of enlarged stenotic part of right main renal artery. (c) Velocity streamline of the whole domain. (d) Velocity detail (maximum 3.76m/sec) of enlarged stenotic part

5.3 Results

SSFP MRA images and CFD results were successfully acquired in all 30 patients and 10 normal volunteers. And 12 of 30 enrolled patients underwent US.

5.3.1 Grade of stenosis

The number of stenotic main renal arteries was 30 (left 15, right 15). Various degrees of RAS (minimum, 2.0%; maximum, 75.5%) were evaluated. Grade 1 was appreciated in twelve renal arteries, grade 2 in seven renal arteries, grade 3 in nine renal arteries, grade 4 in two renal arteries, and grade 5 in none of the renal arteries.

5.3.2 Experimental verification

Maximum velocity of CFD and PSV of US showed high intraclass correlation coefficient (value 0.955) in those 12 patients. And no significant difference ($p>0.05$) between them existed. The CFD results showed the same relationship between velocity and stenotic degree as the Doppler US did (Figure 16).

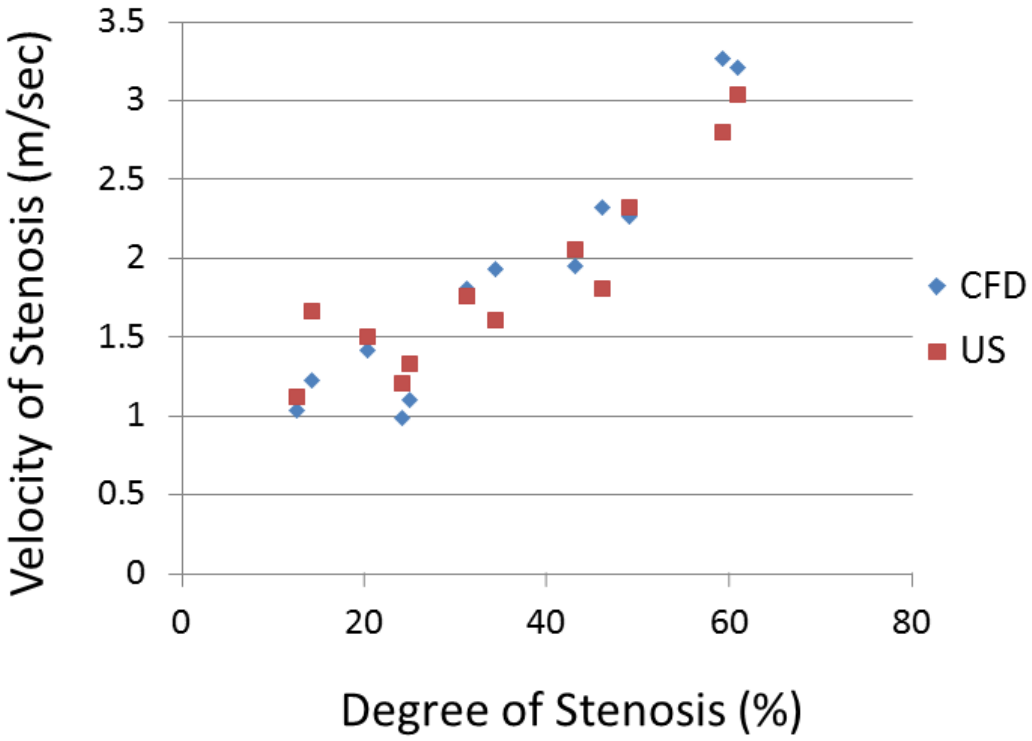

Figure 16. Comparison of maximum velocity of RAS measured using CFD against PSV of US at different stenotic degree in 12 patients. The CFD results showed the same relationship between velocity and stenostic degree as the Doppler US did. There was high intraclass correlation coefficient (value 0.995) and no significant difference ($p>0.05$) between CFD and US

5.3.3 Hemodynamic variables of normal volunteers

In normal volunteers, physiological and hemodynamic characters of main renal arteries were assessed. The average PD of left renal artery extended from 1.80 mmHg to 9.24 mmHg (mean 4.33±1.96 mmHg) and right between 1.82 mmHg and 8.45 mmHg (mean 4.11±1.94 mmHg). The maximum velocity of left normal main renal artery was between 0.67 m/sec and 1.09 m/sec (mean 0.82±0.12 m/sec), and right between 0.64 m/sec and 1.18 m/sec (mean 0.80±0.16 m/sec). MFR values ranged from 541.7 ml/min to 814.7 ml/min (mean 653.7±108.1 ml/min) on the left and from 385.3 ml/min to 658.3 ml/min (mean 546.3±108.1 ml/min) on the right. The velocity, PD and MFR of main renal artery were compared between right and left renal arteries, and these values showed no significant difference ($p>0.05$).

5.3.4 PD of RAS

The different grade of stenosis evoked different PD. The PD profiles were much higher in grade 3 and 4 stenotic cases than in normal, grade 1 and 2 cases, and these are depicted in Figure 17a and 17b. The mean PD, relevant to different stenotic grades of both left and right, were calculated as 4.22±1.90 mmHg for normal cases, 5.86±3.41 mmHg for grade 1, 14.60±6.30 mmHg for grade 2, 68.36±31.01 mmHg for grade 3, and 120.50±2.71 mmHg for grade 4, respectively. No significance existed among normal, grade 1, and grade 2 cases ($p>0.05$). However, all of them were significantly different from grade 3 and grade 4 ($p<0.001$). Measurements in grade 4 were significantly higher than those in grade 3 ($p<0.001$).

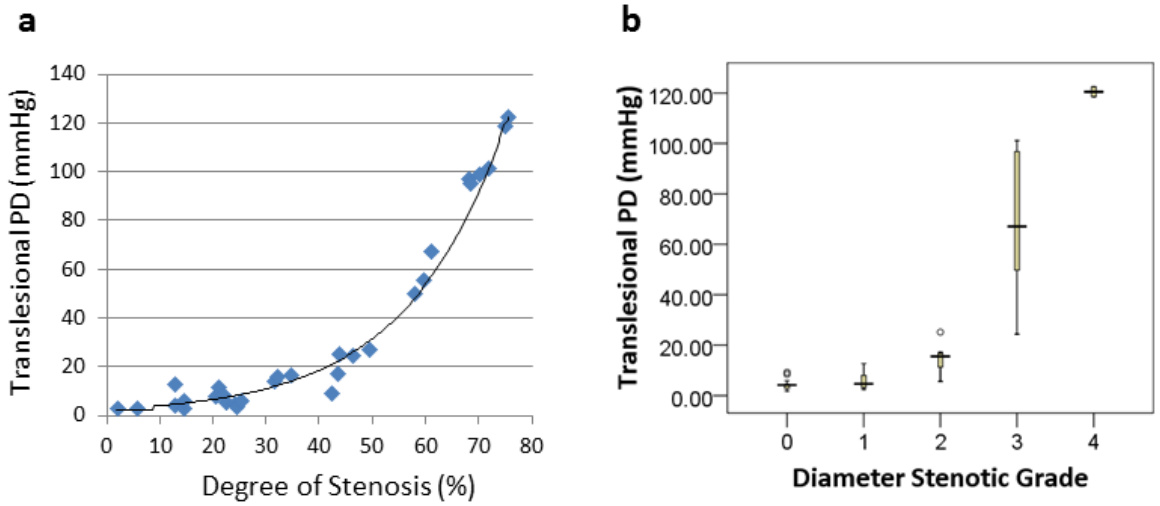

Figure 17. Sum of the static pressure difference of different stenosis. Scatterplot (a) and boxplot (b) charts showed that PD increased with the severity of different stenotic degrees, and the profiles of grade 3 (diameter stenotic degree 50-74%) and grade 4 (75-99%) cases were much higher than those of normal, grade 1 and 2 cases. There was a sudden spike of about 30mmHg for a stenotic degree of 50%, and the range of grade 3 cases was larger than that of other grade cases

5.3.5 Maximum velocity of RAS

The maximum velocities increased with the severity of stenotic degree. And the corresponding velocities of different grades of RAS were: 0.94±0.23, 1.56±0.41, 3.43±0.98, and 4.65±0.31 m/s (maximum 4.87 m/s of diameter stenotic degree 75.5%) for grade 1, 2, 3 and 4. The velocity at the region of stenosis is shown in Figure 18a and 18b. There was a negligible difference between the velocity in normal renal arteries and grade 1 stenotic vessels (p=0.059). Statistical significance in velocity existed between grade 2-4 and control group (p<0.001), and also among grade 2, grade 3, and grade 4 (p<0.01). A spike of more than 2.0 m/s for stenotic degree of 50% and about 4.0 m/s for 70% stenosis was observed.

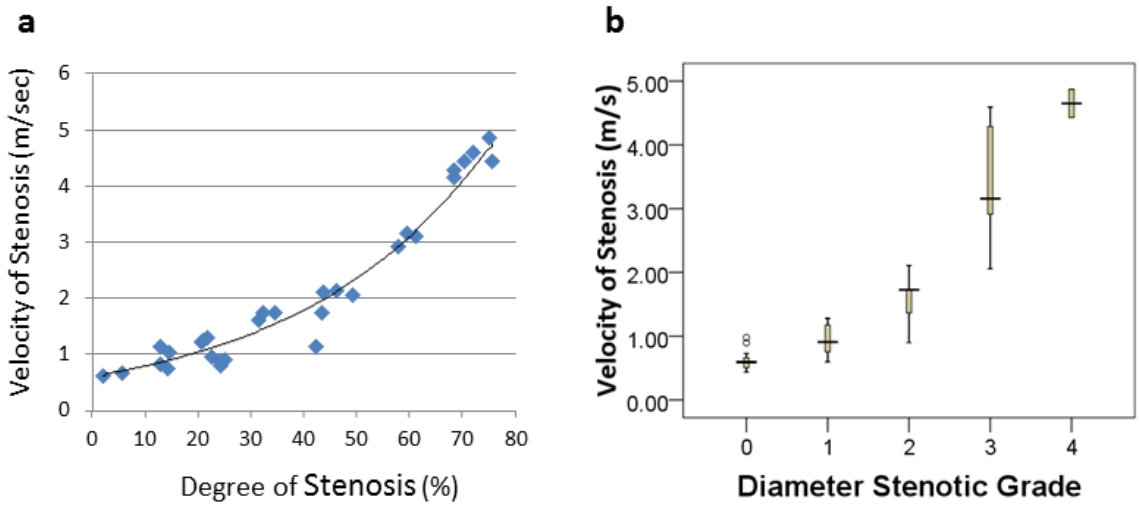

Figure 18. Maximum velocity of different stenoses. Scatterplot (a) and boxplot (b) graphs indicated that the maximum velocity increased with the severity of stenotic degree. Spike of more than 2.0 m/sec for stenotic degree of 50% and about 4.0 m/sec for 70% stenosis were observed

5.3.6 MFR of RAS

The general tendency of MFR decreased with the stenotic degree (Fig. 19a and 19b). Mean MFR of unilateral main renal artery were 544.4±132.8, 502.1±122.6, 299.0±122.6 and 137.4±5.0 ml/min, for grade 1, 2, 3 and 4 cases, respectively. A non-significant trend existed among normal, grade 1 and grade 2 ($p>0.05$). No significant difference was observed between grade 3 and grade 4 ($p>0.05$). However, the two groups showed different statistical significance ($p<0.01$), namely, MFR significantly changed in cases with more than 50% stenoses.

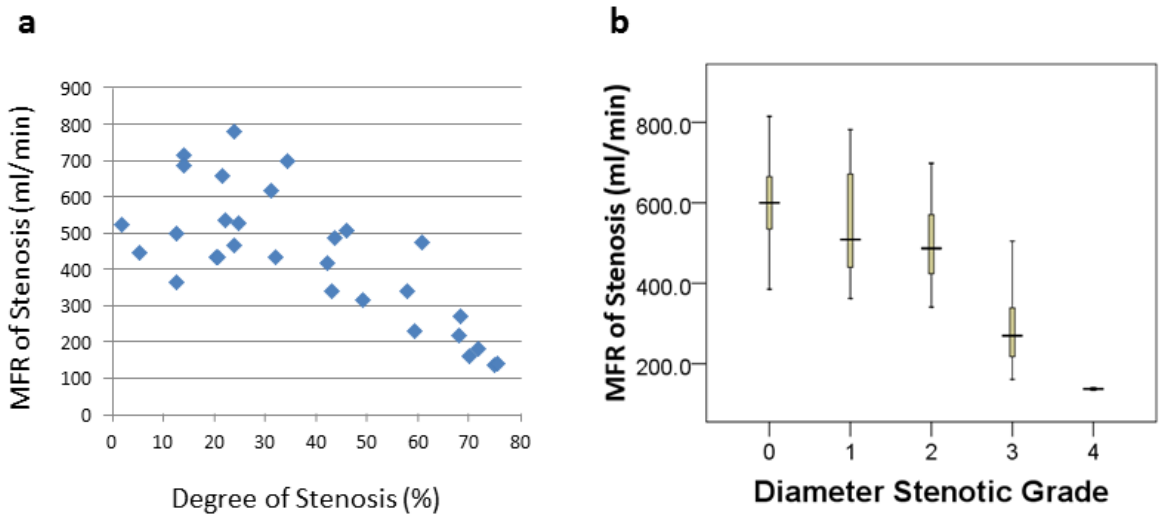

Figure 19. Mass flow rate of stenoses. Scatterplot (a) and boxplot (b) figures showed that the general tendency of MFR decreased with the increase of stenotic degree. MFR of unilateral main renal artery significantly changed in cases with more than 50% stenoses

5.4 Discussion

Currently, CFD technology has been recommended as a tool for clinical application, and it is constantly demonstrated in various models and in vivo studies (25-31, 33, 34, 134, 138). The patient-specific CFD is an evolving technology based on MR and/or CT images, its application has recently gained increased importance due to advanced techniques in MR/CT imaging systems, and its potential to provide a comprehensive evaluation of cardiovascular hemodynamics is promising for improving diagnosis of cardiovascular lesions. To the best of our knowledge, this study is the first of its kind to utilize CFD technology to conduct simulations of blood flow across in vivo RAS based on non-contrast MRA images.

In order to verify the experiment, the maximum velocity measured using CFD was compared to the PSV profile from US which was used as criteria. And CFD results showed the same relationship between velocity and stenotic degree as that of Doppler US according to our results and reports (9, 10). High intraclass correlation coefficient between CFD and US assured that CFD was a reliable method to detect the velocity of RAS and might also be used for further measurement of other hemodynamic parameters of RAS.

For assessment of hemodynamic characters at moderate and severe stenosis, hemodynamically significant RAS is defined as: (1) 50% to 70% diameter stenosis by visual estimation with a peak translesional gradient (measured with a ≤ 5F catheter or pressure wire) of 20 mmHg or higher or a mean gradient of 10 mmHg or higher; (2) 70% or greater diameter stenosis by visual estimation; or (3) 70% or greater diameter stenosis

by intravascular US measurement according to the RAS management guidelines (139, 140). In the present study, only two cases had about 75% diameter stenosis and no cases were observed with a more severe stenosis. Diameter stenosis of more than 75% often shows abnormal glomerular filtration rate with notable clinical symptoms. The significance of the findings, regarding PD, velocity, and MFR, is subsequently described, followed by an examination of the assumptions employed in the present investigation.

The PD in moderate and severe RAS cases were much larger than that in healthy cases, while the mean PD was less than 15 mmHg for normal, grade 1 and 2 groups (less than 50% stenotic degree). Importantly, PD increased with the severity of different stenotic degrees, and there was a sudden spike of about 30 mmHg for a stenotic degree of 50%. According to the arterial disease management guidelines (140), if the translesional PD was more than 20 mmHg for 50% stenosis, it needs adequate treatment. The results presented herein clearly demonstrates that all of cases having greater than or equal to 50% diameter stenosis had a PD of more than 30 mmHg. If it was certified with a much larger group, we may boldly assume that the quantification of the PD may not be necessary and all cases having more than 50% stenoses need further treatment.

The velocity at RAS increased with the severity of different stenotic degrees. It was more than 2 m/s for 50% stenotic degree and reached 4 m/s for 70% stenotic degree, while the maximum velocity of control group was about 0.8 m/sec. Several features of Doppler US velocity field are worth noting (9, 10). First, it utilizes renal artery peak systolic velocity parameters to diagnose RAS. Second, it may not visualize the whole renal arteries and it is

operator-dependent. Also it cannot provide other hemodynamic indications than PSV. As a result, CFD may be more feasible than Doppler US for describing the actual stenotic degree and could also provide the exact hemodynamic changes of the stenotic arteries simultaneously.

As to MFR, the MFR on the left of 10 normal cases was a little higher than that on the right and the total MFR was about 1200 ml/min, and there was no significant difference between left and right. Almost all of renal arteries on the left were at a higher anatomical level than those on the right, which might contribute to the slight difference in the MFR between right and left sides. For stenotic cases, MFR generally decreased with the severity of stenotic degrees and significantly decreased in cases with stenosis more than 50%, which could further influence the glomerular filtration rate of ipsilateral kidney. Additionally, the presence of RAS increased flow resistance and led to considerably lower MFR, which in turn leads to the production of renin and activation of the renin-angiotensin-aldosterone axis, and further increases the blood pressure.

It should be emphasized that 50% diameter stenosis grade is the significant threshold where there is change in the three main hemodynamic parameters in the current study. The translesional PD and Velocity of main renal arteries increased with the severity of different stenotic degrees, and a sudden spike was observed at 50% stenosis. However, MFR decreased with stenotic degrees, along with a sudden drop in cases with more than 50% stenosis.

Although CFD has provided relevant hemodynamic results, it will be necessary to perform further clinical validation to confirm its availabilities in various vascular situations. Especially, the inflow condition of aorta should be investigated by patient-specific blood flow waveform. Furthermore, the assumption of rigid wall and steady blood flow conditions may also affect the results.

Small number of patients with severe renal arterial stenosis is one of the key limitations for this study. A large number of samples with different grades of RAS are proposed for next-stage studies. In addition, stenoses involving accessory renal artery, bilateral RAS or occlusion cases have not been studied in the present study, and will be also another important future works.

5.5 Conclusions

The combination of non-contrast MRA with CFD is an attempt to utilize completely noninvasive methods for comprehensive evaluation of renal artery stenosis. Our initial application of CFD on renal artery demonstrates its potential for an improved understanding of the link that exists between hemodynamics and renal artery stenosis. It may provide useful information regarding patient stratification and strategy in further treatment.

Chapter 6

Analysis of Various Virtual Angioplasty Operation of Renal Artery Stenosis in Hypertension using MR Angiography-Based Computational Fluid Dynamics Technology

Submitted as

Weisheng Zhang, Yi Qian, "Analysis of Various Simulated Angioplasty of Renal Artery Stenosis in Hypertension Using MR Angiography-Based Computational Fluid Dynamics Technology", International Journal of Cardiovascular Imaging, August 2015

Summary

Hemodynamics of renal artery after simulated angioplasty will be discussed in this chapter. A hypertensive patient performed non-contrast MRA is diagnosed with right RAS of 70%. In this study, a series of idealized typical stent models are designed using Pro-Engineer software to modify stent treated branch arteries, then the idealized model are connected with the patient-specific artery to form various situations of virtual endovascular treatment. Hemodynamic simulations under the conditions of various virtual endovascular treatments were analyzed in this chapter.

6.1 Introduction

Renal artery stenosis (RAS) may result from renal vascular diseases, including atherosclerotic arterial lesions, fibromuscular dysplasia and Takayasu arteritis, and as well as 40–50% of patients with occlusive disease of the lower extremities and 15–30% of patients with coronary artery disease (4). RAS can be found in approximately 1-5% of hypertensive patients (1, 2). However, controversy exists among experts regarding the most appropriate utilization of percutaneous renal intervention as the treatment for significant RAS (39, 141). A key principle is that clinical benefit from revascularization will result from correcting renal hypoperfusion caused by significant RAS. Renal artery interventional success occurs when stent deployment results in anatomic and physiological relief of the obstruction to renal blood flow, so physiological confirmation is necessary before and after angioplasty (39).

Currently, the blood flow of renal artery can be noninvasively assessed by Ultrasound, nuclear medicine and phase-contrast (PC) MR angiography (MRA). However, the first two techniques cannot evaluate the pressure difference of RAS and are generally unable to illustrate the actual stenotic location (9-12). PC MRA is strongly influenced by the choice of velocity encoding (ranging 20-80 cm/sec), resulting in decreased peak velocity measurements. And there are also other limitations such as flow artifacts, intravascular signal loss and low vessel depiction quality (16, 18-20).

DSA technique has been widely recognized as a golden standard for determining the severity of RAS. It may as well be used for measuring the hemodynamic characters before

and after angioplasty. However, DSA may be unable to discriminate between non-obstructive RAS and clinical significant RAS. These lesions may be morphologically complex and can be difficult to visualize with 2D angiography. And visual estimation of angiographic stenoses lacks reproducibility and precision (39). A decreasing number of DSA, which cannot predict the effect of different implanted stents, has been used for solely diagnostic imaging of RAS due to its invasive nature.

Clinicians remain in sore need of better tools to identify when renal function can be or no longer be improved with renal revascularization. And there is lack of standard methods to assess hemodynamic or functional reserve of renal artery revascularization (141). However, computational fluid dynamics (CFD) technology is one of the novel technologies to quantitatively estimate hemodynamic conditions of cardiovascular system. It has been successfully applied in a growing number of aspects: intracranial and carotid artery (25-27), heart disease and coronary artery (28-30), aortic artery (31, 32, 142), renal artery (130) and pulmonary artery (33). Currently, fractional flow reserve and systolic translesional gradients have been used to discern those patients likely to benefit from percutaneous transluminal renal artery stent placement (38). CFD technology can well detect hemodynamic viable including pressure difference (PD), velocity, and mass flow rate (MFR) of target vessel (130).

The purpose of this article is to assess MRA-based CFD technology for predicting the treatment effect through analyzing hemodynamic parameters of RAS of different modified stenotic degrees after simulating interventional angioplasty.

6.2 Materials and Methods

6.2.1 Patient data

The tested patient was a 78-year old male, who had a current blood pressure 150/95mmHg and a history of hypertensive medication taken for 20 years, left carotid artery stenting and right carotid endarterectomy 3 years ago, and lower extremity arteriosclerosis obliterans, and was free from elevated creatinine and decreased glomerular filtration rate. The right RAS was diagnosed with 70% diameter stenosis and with normal kidney size using non-contrast MRA. This study was approved by Macquarie University Human Research Ethics Committee (Ref No.: 5201300448, Sydney, Australia).

6.2.2 Scanning method

Non-contrast MRA examination was performed with a 1.5T MR imager (MAGNETOM Aera, software version syngo MR D11; Siemens Healthcare, Erlangen, Germany) using steady-state free precession technique. Sequence Parameters were set as follows: Repetition time 1293.80 msec, Echo time 1.49 msec, Data acquisition time 300-420 sec, Flip angle 90 degree, Bandwidth 781 kHz, Field of view 320×240 mm^2, Section thickness 1.0-1.2 mm, No. of sections 64-80, Spatial resolution 192X256 mm^2, Accelerated factor 2, Inversion time 1200 msec.

6.2.3 RAS geometry generation

A commercial segmentation software Mimics (Version 14.0, Materialise Company, Leuven, Belgium) was utilized to transfer MRA images (DICOM format) into vessel-shape geometric data (STL format). Following the patient-geometry segmentation, a number of different idealized models of typical stents were generated using Pro Engineer Wildfire (Version 2.0, PTC, Needham, MA, USA), and the patient-geometry and the idealized stent geometries were merged together to form a new patient-geometry. The resulting three-dimensional STL formatted artery surface data was meshed using ICEM CFD 13 (ANSYS, Lebanon, New Hampshire) to generate a suitable computational grid for CFD simulation. The whole process shows in Figure 20.

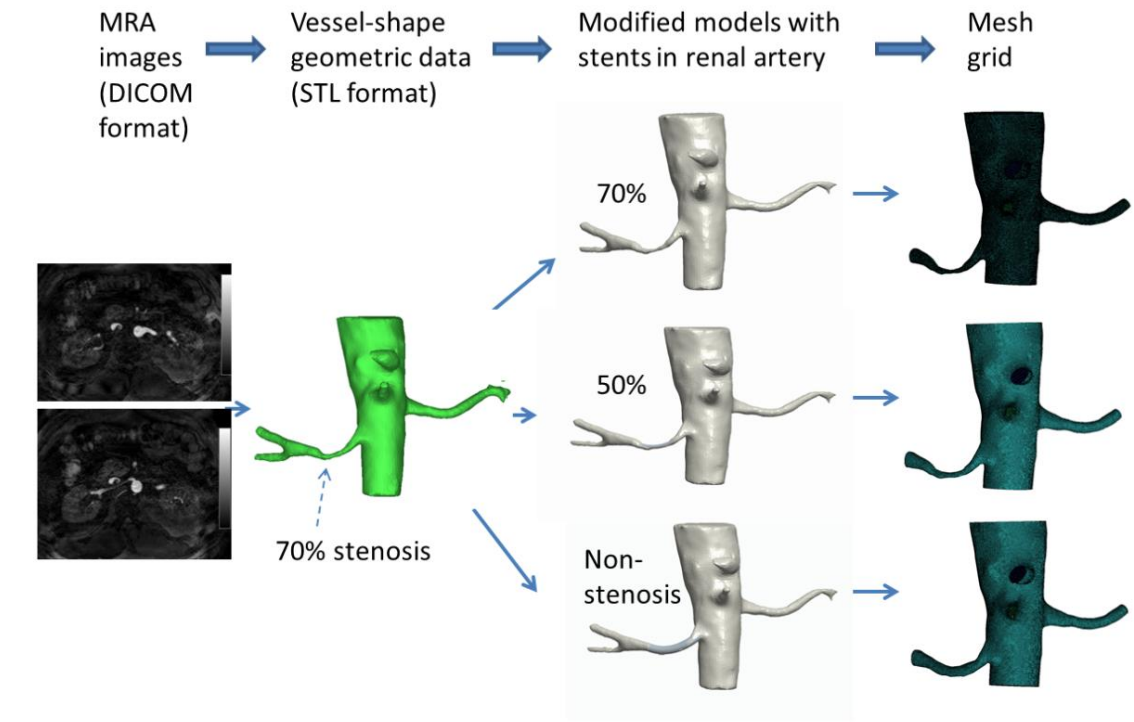

Figure 20. The whole data transfer process of geometry generation. The first step was to transfer MRA images (DICOM format) into vessel-shape geometric data (STL format) with original 70% diameter stenosis on the right side. After different idealized models modified mimicking different degree stents (as shown 70%, 50% and non-stenosis), the three-dimensional STL formatted artery surface data was utilized to form grid for CFD simulation

6.2.4 Simulation methods

Flow entry and exit from the fluid domain was assumed to be normal to the inlet and outlet surface regions of the arterial geometry. The vessel was modeled as rigid with zero wall motion (26, 27, 34). The fluid in this study was assumed as an incompressible Newtonian fluid, while the flow was assumed to be laminar. The density was set 1060 kg/m^3, and the dynamic viscosity 0.0035 Pa.s (26, 27, 130). Steady state flow condition was introduced in order to reproduce the measured volumetric rate and velocity data in an average.

6.2.5 Boundary conditions

Under resting conditions, the patient's blood pressure 150/95mmHg and an average abdominal aortic blood flow rate of 3500 ml/min were introduced at the extended aortic inlet boundary as the inlet boundary condition (34). Zero relative gradient pressure in the flow direction was used at both left and right renal artery outlets at all times (130). All of the above boundary conditions ensured to meet the primary conditions of linear equations. Navier-Stokes governing equations were solved using ANSYS CFX.

6.3 Results

Seven modified models were reconstructed with different diameter stenotic degrees from 60% to 0 with an interval of 10%. The hemodynamic parameters were analyzed for total eight stenotic degrees, including the original 70% stenosis.

6.3.1 PD of RAS

The translesional PD of right stenotic main renal artery of different modified simulating stenoses are shown along with the PD of left normal renal artery (Figure 21a-21e). The PD profile of modified stenosis was much higher than that of normal left side. The translesional PD of right main renal arteries undulately decreased with the declining severity of stenotic degrees. The PD were calculated as 79.78 mmHg for original 70% stenotic degree, 59.16 mmHg for 60%, 58.99 mmHg for 50%, 51.99 mmHg for 40%, and 36.08 mmHg for 30%, 33.62 mmHg for 20%, 29.37 mmHg for 10% and 22.12 mmHg for modified non-stenotic model, respectively.

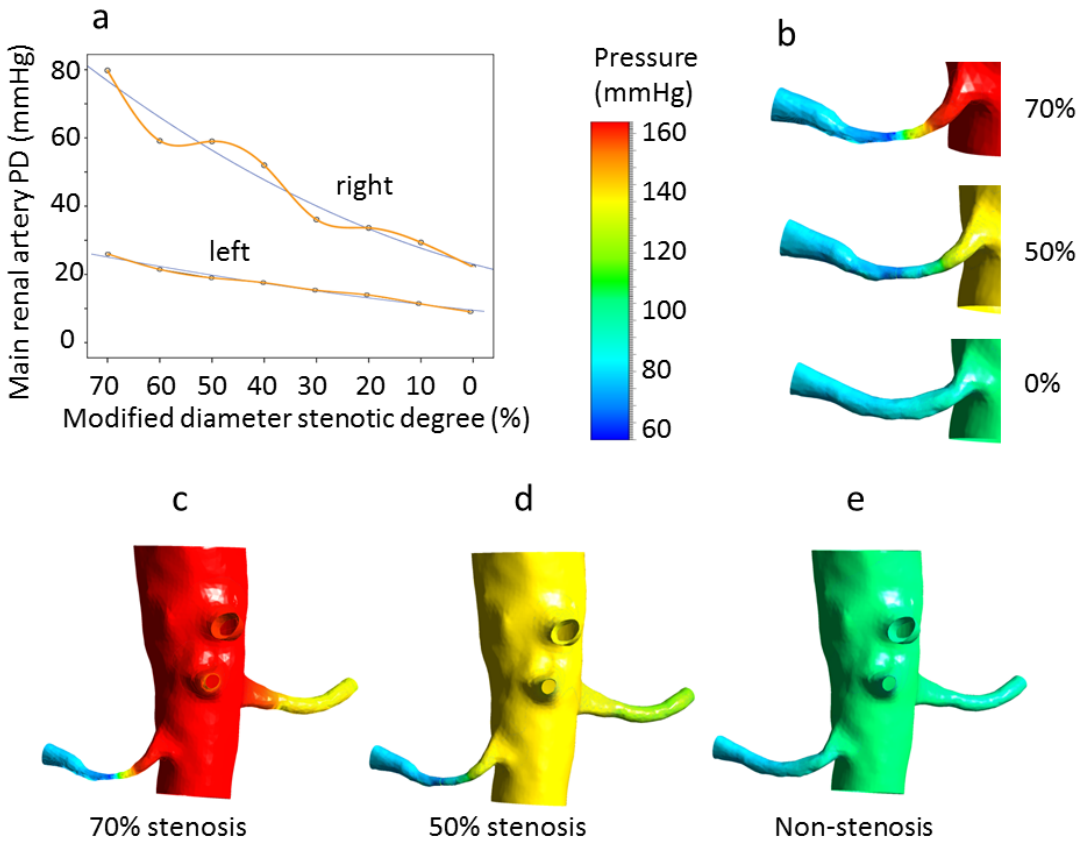

Figure 21. The translesional PD of right RAS in different modified stenoses mimicking revascularization. (a) The spline line shows the real measured PD of right RAS while the quadratic line demonstrates the general tendency. The PD of right RAS undulately decreased with the decline of stenosis along with the PD of left normal renal artery. However, the PD of right RAS was continuously higher than that of left renal artery on the same stenotic level. (b) The enlarged stenotic parts of right RAS in the three diverse stenotic degree stenoses (70%, 50% and non-stenosis with a mimicking stent). (c, d, e) The detailed PD of the whole modified domains mimicking revascularization

6.3.2 Abdominal aortic pressure change

According to the patient's blood pressure 150/95mmHg measured during and after long-term medication, the systolic blood pressure of abdominal aorta decreased and the pressure percentage variation calculated as 13.7%, 14.7%, 18.0%, 24.3%, 28.0%, 29.2%, 34.0% with the decreasing modified diameter stenotic degree from 60% to 0.

6.3.3 Velocity of RAS

The mean velocity inside renal arteries was computed at the stenotic part of each model (Figure 22a-22e). The results indicated that the velocity undulately decreased with the decline of modified stenotic degrees. The maximum velocity of 70% degree stenosis was 4.65m/sec. The mean velocities of different degrees were: 3.68, 2.84, 3.10, 2.73, 2.09, 1.80, 1.95, 1.64 m/sec for stenotic degree 70%, 60%, 50%, 40%, 30%, 20%, 10% and 0, respectively.

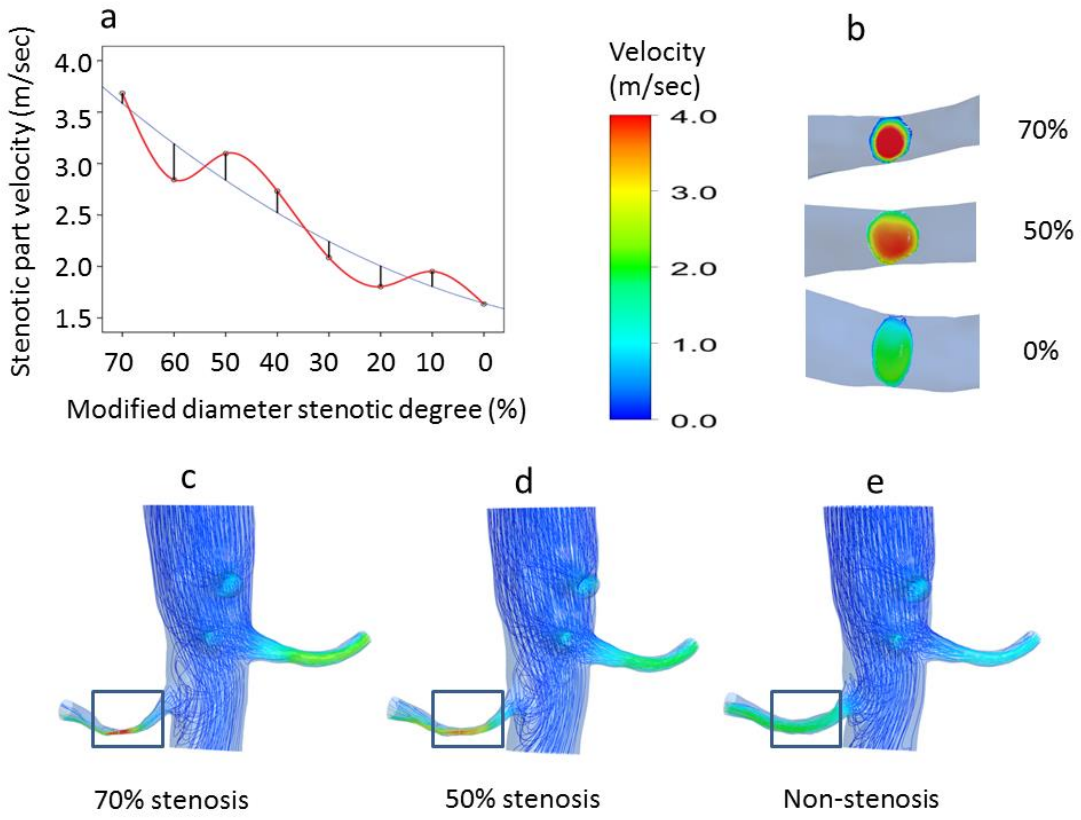

Figure 22. The velocity profiles inside renal artery at the stenotic parts of models. (a) The spline line shows the real measured velocity of right RAS while the quadratic line demonstrates the general tendency. The velocity of RAS undulately decreased with the decline of stenotic degrees. And the mean velocity of 70% was about 3.68 m/sec in comparison with 1.64 m/sec of non-stenosis with a mimicking stent. (b) The cross-sectional velocity profiles of enlarged stenotic parts of right RAS in the three diverse stenotic degree stenoses (70%, 50% and non-stenosis modified with a stent). (c, d, e) The colour-identified streamlines of the whole domains of modified revascularization

6.3.4 MFR of ipsilateral renal artery

The general tendency of MFR increased with the stenotic degrees (Figure 23). MFR of right renal artery were calculated 178.1, 228.2, 338.4, 472.8, 693.4, 528.3, 710.5, 722.8 ml/min, for successive decreasing stenotic degrees.

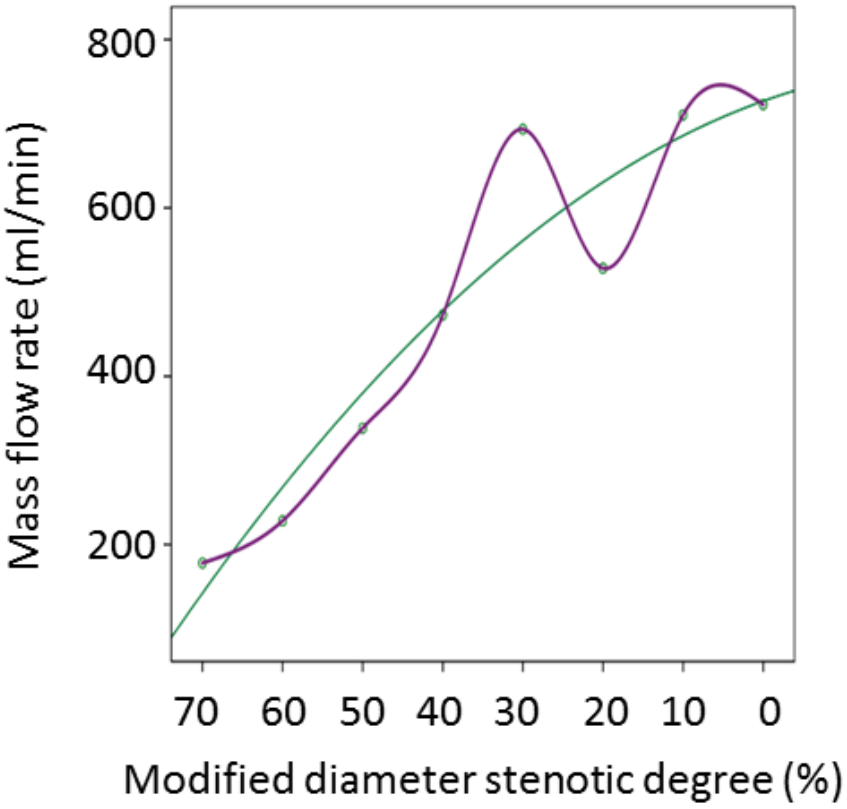

Figure 23. The MFR of right renal artery of different stenotic degrees. The general tendency of MFR increased along with the stenotic degrees while the real undulate PD of right renal artery showed as the spline line

6.4 Discussion

The patient-specific CFD is an evolving technology, and its application has recently gained increased importance because the potential to provide a comprehensive evaluation of cardiovascular hemodynamics is promising for improving diagnosis of cardiovascular lesions. Currently, CFD technology has been accepted in clinical applications, which is constantly demonstrated in various in vitro and in vivo studies (25-34, 130, 142). To our knowledge, this study is the first of its kind to utilize CFD technology to calculate hemodynamic parameters across in vivo RAS of simulated different stenotic degrees.

The patients with percutaneous renal angioplasty and stent placement detected soon after a major change in clinical status are most likely to respond to revascularization (141). Most imaging procedures focus specifically upon the anatomic severity and approach ability of RAS. Although these characteristics are important, they are clearly not sufficient to predict the outcome of renal revascularization. The significance of the present study findings, regarding PD, velocity, and MFR, is subsequently described as follows.

The PD in modified RAS undulately decreased with the decreasing severity of different stenotic degrees. According to the arterial disease management guidelines (140), if the translesional PD was more than 20 mmHg, it needs adequate treatment in clinic. The results presented herein clearly demonstrates that although PD decreased, the revascularized model without stenosis still had a PD more than 20 mmHg, which prompted referring physicians for further medication treatment to these hypertensive patients. The reports show that the strongest correlation for blood pressure improvement is the

hyperemic translesional pressure gradient (39, 143). Our results provided the strong hemodynamic evidence supporting the continuing medications taken in clinic after intervention.

It should be emphasized that the systolic blood pressure of abdominal aorta also decreased along with the decreasing simulated stenotic degree of RAS, although controversy still exists among experts regarding the most appropriate utilization of percutaneous renal intervention as the treatment for significant RAS (39). So we boldly guess that the interventional angioplasty with or without implantation of stent can more or less ameliorate the condition of hypertension. And CFD may be one of the novel methods to predict and certify the effect of stenting.

The velocity at RAS changed with the severity of different stenotic degrees, and it was only 1.64 m/s for modified part without stenosis. The CFD results showed the same relationship between velocity and stenotic degree as Doppler US did (9, 10). But two features of Doppler US velocity field are worth noting (9, 10). First, it utilizes renal artery peak systolic velocity parameters to diagnose RAS. Second, it cannot visualize the whole renal arteries. As a result, CFD was found to be more feasible than Doppler US for describing the real stenotic degree and could provide the exact hemodynamics changes of the stenotic arteries.

As to MFR, it generally increased with the decreasing severity of stenotic degrees and the increase may further influence the glomerular filtration rate of ipsilateral kidney. MFR of right renal artery were calculated 722.8 ml/min of modified non-stenotic model, which

means that the perfusion after revascularization increased and the flow resistance and blood pressure both decreased as would be expected. Renal artery interventional success can be manifested by CFD technology when stent deployment results in anatomic and physiological relief of the obstruction to renal blood flow.

There were several limitations in our present study. A major limitation was the assumption of zero wall motion and constant blood flow utilized for calculations because the basis of CFD methodology is governed by the Navier-Stokes equations with the fluid assumed as an incompressible Newtonian, laminar fluid. The effect of aortic compliance and blood flow waveform were not considered in the current investigation. Further, boundary conditions should be certified and the calculating method should also be standardized. In addition, only one unilateral RAS with 70% stenosis was analysed in present study. The results need to be validated in a large series of patients before widespread clinical adoption, though the results were encouraging.

6.5 Conclusions

In conclusion, our initial application of CFD technology on modified renal artery stenosis demonstrates its potential for an improved prediction of the hemodynamics of renal artery after simulated percutaneous renal angioplasty and stenting. It may help to guide the clinical practice of renal artery stenosis intervention.

Chapter 7

Conclusions and Future Works

Summary

This chapter provides an overview of the objective and findings of this thesis regarding non-contrast MRA and CFD analysis of renal artery in renovascular hypertension. Overall, it was found that the combination of non-contrast MRA with CFD was the first of its kind attempt to utilize completely noninvasive methods for comprehensive evaluation of renal artery stenosis. CFD can provide useful information regarding hypertensive patient stratification and strategy in further treatment. Finally, future directions and necessary considerations are suggested.

7.1 Conclusions and General Discussion

The following conclusions and discussion combined limitations and possible issues are derived from these studies:

1) Chapter 1 provides a background to this thesis by reviewing studies conducted by others in the field of renal artery.

2) SSFP MRA may be a better method approach for imaging renal arteries than other techniques as described in Chapter 2.

3) Non-contrast MRA can avoid the potentially severe adverse effects associated with contrast materials. TrueFISP is a state-of-the-art MRA method comparing with contrast-enhanced MRA for diagnosis of renal artery stenosis in hypertensive patients as presented in Chapter 3.

4) Chapter 4 outlines the techniques of computational fluid dynamics, including blood flow model, governing equations, processing, convergence criteria and post-processing, and its application in renal artery hemodynamics analyzing.

5) In Chapter 5, it was concluded that the combination of non-contrast MRA with CFD was an attempt to utilize completely noninvasive methods for comprehensive evaluation of renal artery stenosis. Our initial application of CFD on renal artery demonstrated its potential for an improved understanding of the link between

hemodynamics and renal artery stenosis. CFD may provide useful information regarding patient stratification and strategy in further treatment.

6) Initial application of CFD technology on modified renal artery stenosis (Chapter 6) demonstrates its potential for an improved prediction of the hemodynamics of renal artery after simulated percutaneous renal angioplasty and stenting. It may help to guide the clinical practice of renal artery stenosis intervention.

7) Conclusions and future directions are generally discussed in this chapter.

7.2 Future Directions

7.2.1 Wall shear stress (WSS) & energy loss (EL) evaluation of RAS

7.2.1.1 WSS definition

Mechanical force affecting endothelial cells can be classified as: 1) an oscillatory force due to pulsatile pressure; 2) WSS (Figure 24) as the tangential force per unit area that is exerted by the moving fluid on the surface of the artery and its magnitude is proportional to the velocity gradient near the artery surface (144).

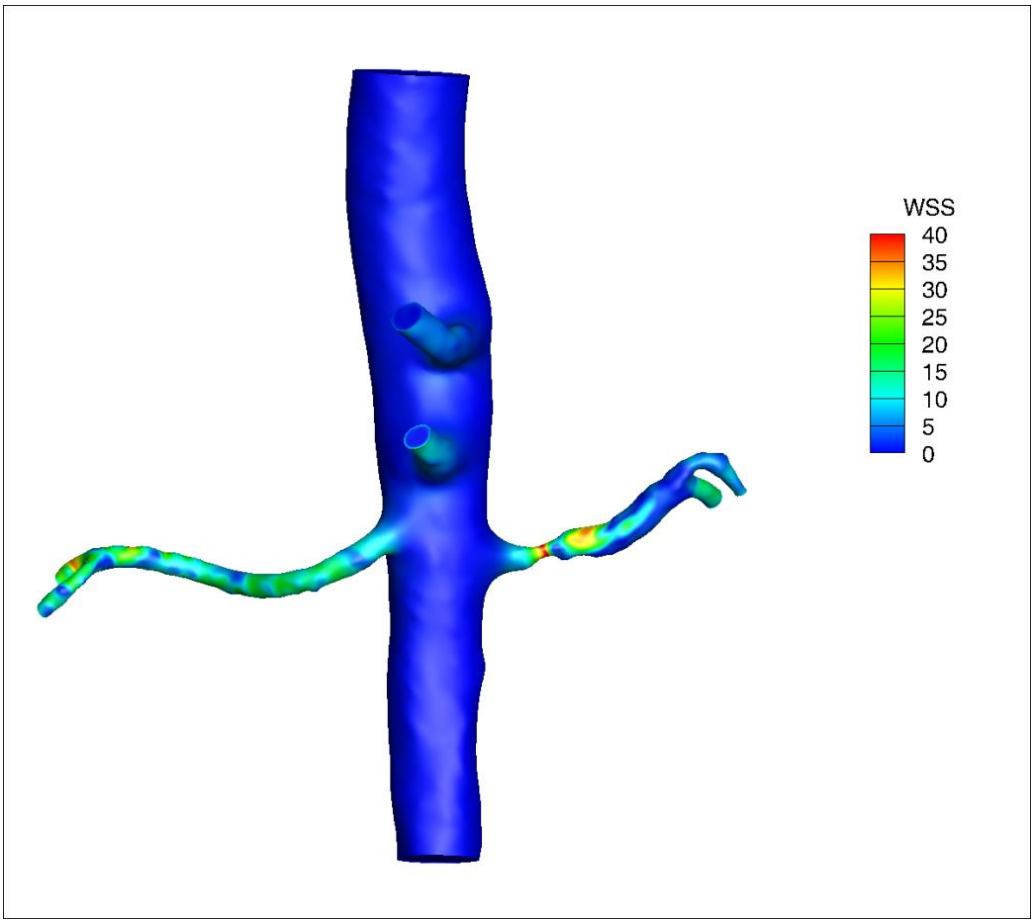

Figure 24. WSS of one model (Pa)

The interaction between WSS and endothelial cells which results in chemical and mechanical changes in extracellular matrix (ECM) and vascular smooth muscle cells (VSMC) (145) is of particular interest for investigating the mechanism of aneurysm/stenosis formation, growth and rupture. This shearing force between the vascular wall and the outermost layer of blood mainly applies to the vascular endothelium, the inner layer of the vascular wall in contact with blood flow, and affects the structural integrity and the function of the endothelial cells (ECs) (146). In healthy arteries and in the presence of EC and VSMC, it has been shown that by variation of vascular diameter according to the stress, the auto-regulatory mechanism of the vascular wall keeps the WSS constant at physiological baseline values (147, 148). This morphological change of the vascular endothelium produces different levels of vasoactive mediators such as nitric oxide (NO) which exerts in flow-mediated arterial remodeling (149). Local increase of WSS can result in local enlargement and injury to the arterial wall and destructive remodeling due to extreme production of NO (148). Over-expression of NO causes a disturbance between the equilibrium of blood pressure and internal wall stress force leading to local dilation of the arterial wall (150). The arterial wall's mechanical properties are determined by collagen, elastin, and smooth muscle cells. Therefore, the variation of structure and composition of the arterial wall will affect its mechanical properties (151). The growth of the aneurysm stretches the collagen and elastin fibers of the medical and adventitial layers and increases the internal stresses which are associated with arterial stiffness. Eventually, the internal wall stresses and the transmural pressure become equal to equilibrate the biomechanical system, while the local hemodynamics cannot change the property of the arterial wall.

Thus, the collagen and the elastin that are constantly affected by a non-physiological mechanical load undergo remodeling.

Localized blood flow velocity causes the aggregation of red blood cells, the adhesion of cells to lumen and accumulation of platelets and leukocytes along the intimal surface due to dysfunction of flow-induced NO (121, 152). This process results in intimal damage and the infiltration of white blood cells and fibrin inside the vessel wall (153). As a result of this inflammation, the localized degeneration of the vessel wall decreases the pressure threshold below the physiological tensile forces that can be supported, leading to gradual reduction of wall thickness and eventually tearing the tissue (154). Based on high (98, 112, 155-157) and low (158-160) WSS theories, there is significant controversy among CFD investigation regarding the mechanism responsible for the formation of aneurysms/stenosis. It is assumed that a WSS of 2.0 N/m^2 is suitable for maintaining the structure of arterial vessels and a WSS lower than 1.5 N/m^2 will degenerate endothelial cells via the apoptotic cell cycle (161).

7.2.1.2 Calculation of EL

The product of force and displacement in the direction of force are defined as energy in physics. In the cardiovascular system, as the blood leaves the heart, it loses its power when passing through the vasculature in the form of heat, therefore the average pressure and the velocity of the blood flow decrease along with distance. For points in proximity, heat energy transferred between the arteries and fluid as either a heat gain or loss is small and can be neglected. According to the first law of thermodynamics, the energy stored in the

system must be equal to the amount of energy transferred to the system. However, formation of vortex, flow separation and stagnation result in energy loss of the system.

By using Bernoulli's equation, energy loss was defined as the difference between energy transport to the stenosis by influx and energy loss from the stenosis by outflow. Thus, the stenotic section area was considered for EL calculation by assuming that positive and negative velocities depict an inflow and outflow.

EL can be calculated by the following equation:

$$\text{Energy loss(EL)} = E_{\text{inlet}} - E_{\text{outlet}} \tag{15}$$

$$\text{EL} = \underbrace{\sum \left(P_i + \frac{1}{2}\rho {v_i}^2\right) Q_i}_{E_{inlet}} - \underbrace{\sum \left(P_o + \frac{1}{2}\rho {v_o}^2\right) Q_o}_{E_{outlet}} \tag{16}$$

Where P, v are the static pressure and velocity, respectively; i indicates the inflow to the stenosis; o shows the outflow of stenosis. E_{inlet} and E_{outlet} are the spatially averaged energy values over the cross section of the stenosis.

According to the above discussion, the study on WSS & EL evaluation of RAS is meaningful for renal artery stenosis formation and clinical treatment. We are planning for the near future study about this.

7.2.2 Exploration of renal artery atherosclerosis

As the statement in the item 7.2.1.1 and 7.2.1.2, WSS and EL play an important role for the formation of stenosis. RAS is caused by a heterogeneous group of conditions, including

atherosclerosis, FMD, vasculitis, neurofibromatosis, congenital bands, and extrinsic compression, and radiation (40). Atherosclerosis accounts for approximately 90% of the lesions that obstruct blood flow to the renal arteries. Atherosclerotic RAS typically involves the ostium and/or proximal one-third of the renal artery and often the adjacent aorta (162).

Atherosclerotic RAS results in a progressive loss of renal mass and function over time. In a subgroup of patients with renovascular hypertension and 60% obstruction, renal atrophy occurs in 21% (163, 164). Historical data suggest that up to 27% of patients with atherosclerotic RAS will develop chronic renal failure within 6 years (165). A prospective angiographic study reveals that atherosclerotic RAS is the cause of end-stage renal disease in 14% of patients in whom dialysis was newly initiated (166). Thus, early detection and appropriate treatment of atherosclerotic RAS could have important consequences.

For an imaging study to be considered optimal, the following 4 objectives must be considered: (1) atherosclerotic RAS must be detected and characterized on the basis of anatomic and hemodynamic severity; (2) anatomic consequences of atherosclerotic RAS on the artery itself and on the kidney must be assessed; (3) functional and cellular consequences of RAS on the kidney must be evaluated; and (4) criteria associated with renal impairment related to renovascular disease must be identified (167).

7.2.3 Analysis of renal artery aneurysm using CFD

We have noticed that post-stenotic dilatation or aneurysm happens when severe stenosis exists in the proximity of renal artery. Renal artery aneurysms are uncommon, occurring in approximately 0.09% of the general population (168). However, renal artery aneurysms are considered the second most common visceral aneurysm (15-22%), most common being splenic artery aneurysm (60%) (169). They are more common in females. Most of the lesions are saccular and tend to occur at the bifurcation of main renal artery.

In addition, we find that the kidney atrophy happens if stenosis exists in the end part of renal artery. It means shrinkage of the renal parenchyma, with the kidney being <8 cm (167).

Most prior definitions of the clinical, pathologic, and management features of renal artery aneurysm have evolved from anecdotal reports. Controversy surrounding this clinical entity continues. Therefore, analysis of renal artery aneurysm using CFD will help to discover the principal of the renal artery aneurysm formation.

7.2.4 Renal vessel diseases analysis using MRA

Renal vascular disease is the name given to a variety of complications that affect the arteries and veins of the kidneys. These complications affect the blood circulation of the kidneys, and may cause damage to the tissues of the kidneys, kidney failure, and/or high blood pressure.

Vascular conditions affecting the renal arteries and veins include the following:

1) Renal artery stenosis. Renal artery stenosis (RAS) is a blockage of an artery to the kidneys. It may cause kidney failure and hypertension (high blood pressure). Smokers have a greater risk of developing RAS. RAS is most common in men between the ages of 50 and 70. High cholesterol, diabetes, being overweight, and having a family history of cardiovascular disease are also risk factors for RAS. High blood pressure is both a cause and a result of RAS.

2) Renal artery thrombosis. Renal artery thrombosis is the formation of a clot in a renal artery. A thrombosis of a renal artery may cause kidney failure because of blocked blood flow to the kidney.

3) Renal artery aneurysm. A renal artery aneurysm is a bulging, weakened area in the wall of an artery to the kidney. Most of these aneurysms are small (less than two centimeters, or about three-quarters of an inch) and without symptoms. Renal artery aneurysms are uncommon and are generally discovered during diagnostic procedures performed in relation to other conditions.

4) Atheroembolic renal disease. Atheroembolic renal disease occurs when a piece of plaque from the aorta and/or other large arteries breaks off and travels through the bloodstream, blocking small arteries such as the renal arteries. Atheroembolic renal disease is becoming a common cause of renal insufficiency (poor kidney function) in the elderly.

5) Renal vein thrombosis. A renal vein thrombosis is the formation of a clot in a vein to the kidney.

MRA is a noninvasive diagnostic procedure that uses a combination of magnetic resonance imaging (MRI) technology and intravenous (IV) contrast dye to visualize blood vessels. Morphological and functional characterization of left renal vein can be assessed with multiphase breath-hold 3D gadolinium-enhanced MRA. Functional data can be obtained via the abnormal intra-renal transit of gadolinium during magnetic resonance imaging with use of captopril. And future studies are assessing the ability of diffusion-weighted magnetic resonance imaging to determine the cellular viability of renal parenchyma tissue in patients with chronic kidney disease.

7.2.5 Hemodynamic analysis of iliac artery

Along with the study of renal vessels using MRA and CFD, iliac artery diseases may be included in further study. There are also many puzzles exists for scientific study.

Aortoiliac occlusive disease is a type of peripheral arterial disease, which affects the iliac arteries. The aorta, the body's largest artery, divides around the area of the belly button into two branches form the iliac arteries. The iliac arteries run through the pelvis and down into the legs then divide further into smaller arteries that end at the toes. Aortoiliac occlusive disease occurs when the iliac arteries become hardened or blocked. At youth age, it is not uncommon for plaque to build up on the inside of artery walls. As more plaque accumulates, the arteries begin to narrow and stiffen causing atherosclerosis, or hardening

of the arteries. When enough plaque builds up to interfere with blood flow, it is called aortoiliac occlusive disease. It can reduce blood flow to the legs, which can lead to a condition called ischemia. When blood flow is reduced, the legs do not receive enough oxygen, which can cause pain. If left untreated, ischemia can become severe and lead to sores or gangrene, and even the loss of a limb.

Diagnostic procedures are needed to determine a firm diagnosis and to learn how much the disease has advanced. Typically, MRA takes longer to perform than CTA. However, unlike CTA, it does not use radiation, so doctors commonly favor MRA for repeated follow-ups.

However, currently, there is no report about hemodynamic analysis of iliac artery. It must be an important novel area for research and useful for clinician total assessment and treatment of iliac artery.

REFERENCES

1. Olin JW. Atherosclerotic renal artery disease. *Cardiol Clin* 2002;20:547-562, vi
2. Mann SJ, Pickering TG. Detection of renovascular hypertension. State of the art: 1992. *Ann Intern Med* 1992;117:845-853
3. Derkx FH, Schalekamp MA. Renal artery stenosis and hypertension. *Lancet* 1994;344:237-239
4. Uzu T, Inoue T, Fujii T, Nakamura S, Inenaga T, Yutani C, et al. Prevalence and predictors of renal artery stenosis in patients with myocardial infarction. *Am J Kidney Dis* 1997;29:733-738
5. Ramos F, Kotliar C, Alvarez D, Baglivo H, Rafaelle P, Londero H, et al. Renal function and outcome of PTRA and stenting for atherosclerotic renal artery stenosis. *Kidney Int* 2003;63:276-282
6. Beutler JJ, Van Ampting JM, Van De Ven PJ, Koomans HA, Beek FJ, Woittiez AJ, et al. Long-term effects of arterial stenting on kidney function for patients with ostial atherosclerotic renal artery stenosis and renal insufficiency. *J Am Soc Nephrol* 2001;12:1475-1481
7. White CJ. Catheter-based therapy for atherosclerotic renal artery stenosis. *Circulation* 2006;113:1464-1473
8. Safian RD, Textor SC. Renal-artery stenosis. *N Engl J Med* 2001;344:431-442
9. Li JC, Jiang YX, Zhang SY, Wang L, Ouyang YS, Qi ZH. Evaluation of renal artery stenosis with hemodynamic parameters of Doppler sonography. *J Vasc Surg* 2008;48:323-328
10. Chain S, Luciardi H, Feldman G, Berman S, Herrera RN, Ochoa J, et al. Diagnostic role of new Doppler index in assessment of renal artery stenosis. *Cardiovasc Ultrasound* 2006;4:4
11. Taylor A. Renovascular hypertension: nuclear medicine techniques. *Q J Nucl Med* 2002;46:268-282
12. Itoh K. 99mTc-MAG3: review of pharmacokinetics, clinical application to renal diseases and quantification of renal function. *Ann Nucl Med* 2001;15:179-190
13. Chopra T, Kandukurti K, Shah S, Ahmed R, Panesar M. Understanding nephrogenic systemic fibrosis. *Int J Nephrol* 2012;2012:912189
14. Thomsen HS, Morcos SK, Dawson P. Is there a causal relation between the administration of gadolinium based contrast media and the development of nephrogenic systemic fibrosis (NSF)? *Clin Radiol* 2006;61:905-906
15. Grobner T. Gadolinium--a specific trigger for the development of nephrogenic fibrosing dermopathy and nephrogenic systemic fibrosis? *Nephrol Dial Transplant* 2006;21:1104-1108
16. de Haan MW, Kouwenhoven M, Kessels AG, van Engelshoven JM. Renal artery blood flow: quantification with breath-hold or respiratory triggered phase-contrast MR imaging. *Eur Radiol* 2000;10:1133-1137
17. Schoenberg SO, Bock M, Kallinowski F, Just A. Correlation of hemodynamic impact and morphologic degree of renal artery stenosis in a canine model. *J Am Soc Nephrol* 2000;11:2190-2198
18. Westenberg JJ, Wasser MN, van der Geest RJ, Pattynama PM, de Roos A, Vanderschoot J, et al. Variations in blood flow waveforms in stenotic renal arteries by 2D phase-contrast cine MRI. *J Magn Reson Imaging* 1998;8:590-597
19. Markl M, Frydrychowicz A, Kozerke S, Hope M, Wieben O. 4D flow MRI. *J Magn Reson Imaging* 2012;36:1015-1036
20. Francois CJ, Lum DP, Johnson KM, Landgraf BR, Bley TA, Reeder SB, et al. Renal arteries: isotropic, high-spatial-resolution, unenhanced MR angiography with three-dimensional radial phase contrast. *Radiology* 2011;258:254-260
21. Tan H, Koktzoglou I, Glielmi C, Galizia M, Edelman RR. Optimization of single shot 3D breath-hold non-enhanced MR angiography of the renal arteries. *J Cardiovasc Magn Reson* 2012;14:30

22. Klee D, Lanzman RS, Blondin D, Schmitt P, Oh J, Salgin B, et al. Non-enhanced ECG-gated respiratory-triggered 3-D steady-state free-precession MR angiography with slab-selective inversion: initial experience in visualisation of renal arteries in free-breathing children without renal artery abnormality. *Pediatr Radiol* 2012;42:785-790
23. Parienty I, Rostoker G, Jouniaux F, Piotin M, Admiraal-Behloul F, Miyazaki M. Renal artery stenosis evaluation in chronic kidney disease patients: nonenhanced time-spatial labeling inversion-pulse three-dimensional MR angiography with regulated breathing versus DSA. *Radiology* 2011;259:592-601
24. Liu X, Berg N, Sheehan J, Bi X, Weale P, Jerecic R, et al. Renal transplant: nonenhanced renal MR angiography with magnetization-prepared steady-state free precession. *Radiology* 2009;251:535-542
25. Schneiders JJ, Marquering HA, Antiga L, van den Berg R, VanBavel E, Majoie CB. Intracranial aneurysm neck size overestimation with 3D rotational angiography: the impact on intra-aneurysmal hemodynamics simulated with computational fluid dynamics. *AJNR Am J Neuroradiol* 2013;34:121-128
26. Zhang Y, Sia SF, Morgan MK, Qian Y. Flow resistance analysis of extracranial-to-intracranial (EC-IC) vein bypass. *J Biomech* 2012;45:1400-1405
27. Qian Y, Takao H, Umezu M, Murayama Y. Risk analysis of unruptured aneurysms using computational fluid dynamics technology: preliminary results. *AJNR Am J Neuroradiol* 2011;32:1948-1955
28. Katritsis DG, Theodorakakos A, Pantos I, Gavaises M, Karcanias N, Efstathopoulos EP. Flow patterns at stented coronary bifurcations: computational fluid dynamics analysis. *Circ Cardiovasc Interv* 2012;5:530-539
29. DeCampli WM, Argueta-Morales IR, Divo E, Kassab AJ. Computational fluid dynamics in congenital heart disease. *Cardiol Young* 2012;22:800-808
30. Chaichana T, Sun Z, Jewkes J. Computational fluid dynamics analysis of the effect of plaques in the left coronary artery. *Comput Math Methods Med* 2012;2012:504367
31. Tse KM, Chang R, Lee HP, Lim SP, Venkatesh SK, Ho P. A computational fluid dynamics study on geometrical influence of the aorta on haemodynamics. *Eur J Cardiothorac Surg* 2013;43:829-838
32. Karmonik C, Partovi S, Davies MG, Bismuth J, Shah DJ, Bilecen D, et al. Integration of the computational fluid dynamics technique with MRI in aortic dissections. *Magn Reson Med* 2013;69:1438-1442
33. Tang BT, Pickard SS, Chan FP, Tsao PS, Taylor CA, Feinstein JA. Wall shear stress is decreased in the pulmonary arteries of patients with pulmonary arterial hypertension: An image-based, computational fluid dynamics study. *Pulm Circ* 2012;2:470-476
34. Taylor CA, Hughes TJ, Zarins CK. Finite element modeling of three-dimensional pulsatile flow in the abdominal aorta: relevance to atherosclerosis. *Ann Biomed Eng* 1998;26:975-987
35. Kem DC, Lyons DF, Wenzl J, Halverstadt D, Yu X. Renin-dependent hypertension caused by nonfocal stenotic aberrant renal arteries: proof of a new syndrome. *Hypertension* 2005;46:380-385
36. Aytac SK, Yigit H, Sancak T, Ozcan H. Correlation between the diameter of the main renal artery and the presence of an accessory renal artery: sonographic and angiographic evaluation. *J Ultrasound Med* 2003;22:433-439; quiz 440-432
37. Chrysant SG, Chrysant GS. Treatment of hypertension in patients with renal artery stenosis due to fibromuscular dysplasia of the renal arteries. *Cardiovasc Diagn Ther* 2014;4:36-43
38. Patel RA, White CJ. Renal intervention to treat hypertension. *Curr Cardiol Rep* 2012;14:142-149

39. White CJ. Optimizing outcomes for renal artery intervention. *Circ Cardiovasc Interv* 2010;3:184-192
40. Dubel GJ, Murphy TP. The role of percutaneous revascularization for renal artery stenosis. *Vasc Med* 2008;13:141-156
41. Levey AS, Coresh J, Balk E, Kausz AT, Levin A, Steffes MW, et al. National Kidney Foundation practice guidelines for chronic kidney disease: evaluation, classification, and stratification. *Ann Intern Med* 2003;139:137-147
42. Miyazaki M, Lee VS. Nonenhanced MR angiography. *Radiology* 2008;248:20-43
43. JM UK-I, Young V, Gillard JH. Carotid-artery imaging in the diagnosis and management of patients at risk of stroke. *Lancet Neurol* 2009;8:569-580
44. Tatli S, Lipton MJ, Davison BD, Skorstad RB, Yucel EK. From the RSNA refresher courses: MR imaging of aortic and peripheral vascular disease. *Radiographics* 2003;23 Spec No:S59-78
45. Ozsarlak O, Van Goethem JW, Maes M, Parizel PM. MR angiography of the intracranial vessels: technical aspects and clinical applications. *Neuroradiology* 2004;46:955-972
46. Pui MH. Cerebral MR venography. *Clin Imaging* 2004;28:85-89
47. de Haan MW, Kouwenhoven M, Thelissen RP, Koster D, Kessels AG, de Leeuw PW, et al. Renovascular disease in patients with hypertension: detection with systolic and diastolic gating in three-dimensional, phase-contrast MR angiography. *Radiology* 1996;198:449-456
48. Steffens JC, Link J, Muller-Hulsbeck S, Freund M, Brinkmann G, Heller M. Cardiac-gated two-dimensional phase-contrast MR angiography of lower extremity occlusive disease. *AJR Am J Roentgenol* 1997;169:749-754
49. Vanninen RL, Manninen HI, Partanen PL, Vainio PA, Soimakallio S. Carotid artery stenosis: clinical efficacy of MR phase-contrast flow quantification as an adjunct to MR angiography. *Radiology* 1995;194:459-467
50. Mohajer K, Zhang H, Gurell D, Ersoy H, Ho B, Kent KC, et al. Superficial femoral artery occlusive disease severity correlates with MR cine phase-contrast flow measurements. *J Magn Reson Imaging* 2006;23:355-360
51. Sanz J, Kuschnir P, Rius T, Salguero R, Sulica R, Einstein AJ, et al. Pulmonary arterial hypertension: noninvasive detection with phase-contrast MR imaging. *Radiology* 2007;243:70-79
52. Barger AV, Block WF, Toropov Y, Grist TM, Mistretta CA. Time-resolved contrast-enhanced imaging with isotropic resolution and broad coverage using an undersampled 3D projection trajectory. *Magn Reson Med* 2002;48:297-305
53. Hope TA, Markl M, Wigstrom L, Alley MT, Miller DC, Herfkens RJ. Comparison of flow patterns in ascending aortic aneurysms and volunteers using four-dimensional magnetic resonance velocity mapping. *J Magn Reson Imaging* 2007;26:1471-1479
54. Frydrychowicz A, Winterer JT, Zaitsev M, Jung B, Hennig J, Langer M, et al. Visualization of iliac and proximal femoral artery hemodynamics using time-resolved 3D phase contrast MRI at 3T. *J Magn Reson Imaging* 2007;25:1085-1092
55. Yamashita S, Isoda H, Hirano M, Takeda H, Inagawa S, Takehara Y, et al. Visualization of hemodynamics in intracranial arteries using time-resolved three-dimensional phase-contrast MRI. *J Magn Reson Imaging* 2007;25:473-478
56. Uribe S, Beerbaum P, Sorensen TS, Rasmusson A, Razavi R, Schaeffter T. Four-dimensional (4D) flow of the whole heart and great vessels using real-time respiratory self-gating. *Magn Reson Med* 2009;62:984-992
57. Markl M, Draney MT, Hope MD, Levin JM, Chan FP, Alley MT, et al. Time-resolved 3-dimensional velocity mapping in the thoracic aorta: visualization of 3-directional blood flow patterns in healthy

volunteers and patients. *J Comput Assist Tomogr* 2004;28:459-468

58. Wedeen VJ, Meuli RA, Edelman RR, Geller SC, Frank LR, Brady TJ, et al. Projective imaging of pulsatile flow with magnetic resonance. *Science* 1985;230:946-948
59. Lim RP, Hecht EM, Xu J, Babb JS, Oesingmann N, Wong S, et al. 3D nongadolinium-enhanced ECG-gated MRA of the distal lower extremities: preliminary clinical experience. *J Magn Reson Imaging* 2008;28:181-189
60. Miyazaki M, Sugiura S, Tateishi F, Wada H, Kassai Y, Abe H. Non-contrast-enhanced MR angiography using 3D ECG-synchronized half-Fourier fast spin echo. *J Magn Reson Imaging* 2000;12:776-783
61. Lim RP, Storey P, Atanasova IP, Xu J, Hecht EM, Babb JS, et al. Three-dimensional electrocardiographically gated variable flip angle FSE imaging for MR angiography of the hands at 3.0 T: initial experience. *Radiology* 2009;252:874-881
62. Fuchs F, Laub G, Othomo K. TrueFISP--technical considerations and cardiovascular applications. *Eur J Radiol* 2003;46:28-32
63. Scheffler K, Lehnhardt S. Principles and applications of balanced SSFP techniques. *Eur Radiol* 2003;13:2409-2418
64. Zhang W, Lin J, Wang S, Lv P, Wang L, Liu H, et al. Unenhanced respiratory-gated magnetic resonance angiography (MRA) of renal artery in hypertensive patients using true fast imaging with steady-state precession technique compared with contrast-enhanced MRA. *J Comput Assist Tomogr* 2014;38:700-704
65. Wyttenbach R, Braghetti A, Wyss M, Alerci M, Briner L, Santini P, et al. Renal artery assessment with nonenhanced steady-state free precession versus contrast-enhanced MR angiography. *Radiology* 2007;245:186-195
66. Amano Y, Takahama K, Kumita S. Non-contrast-enhanced MR angiography of the thoracic aorta using cardiac and navigator-gated magnetization-prepared three-dimensional steady-state free precession. *J Magn Reson Imaging* 2008;27:504-509
67. Krishnam MS, Tomasian A, Malik S, Desphande V, Laub G, Ruehm SG. Image quality and diagnostic accuracy of unenhanced SSFP MR angiography compared with conventional contrast-enhanced MR angiography for the assessment of thoracic aortic diseases. *Eur Radiol* 2010;20:1311-1320
68. Ishida M, Kato S, Sakuma H. Cardiac MRI in ischemic heart disease. *Circ J* 2009;73:1577-1588
69. Kim WY, Danias PG, Stuber M, Flamm SD, Plein S, Nagel E, et al. Coronary magnetic resonance angiography for the detection of coronary stenoses. *N Engl J Med* 2001;345:1863-1869
70. van Laar PJ, van der Grond J, Hendrikse J. Brain perfusion territory imaging: methods and clinical applications of selective arterial spin-labeling MR imaging. *Radiology* 2008;246:354-364
71. Spuentrup E, Manning WJ, Bornert P, Kissinger KV, Botnar RM, Stuber M. Renal arteries: navigator-gated balanced fast field-echo projection MR angiography with aortic spin labeling: initial experience. *Radiology* 2002;225:589-596
72. Shimada K, Isoda H, Okada T, Kamae T, Arizono S, Hirokawa Y, et al. Non-contrast-enhanced MR portography with time-spatial labeling inversion pulses: comparison of imaging with three-dimensional half-fourier fast spin-echo and true steady-state free-precession sequences. *J Magn Reson Imaging* 2009;29:1140-1146
73. Satogami N, Okada T, Koyama T, Gotoh K, Kamae T, Togashi K. Visualization of external carotid artery and its branches: non-contrast-enhanced MR angiography using balanced steady-state free-precession sequence and a time-spatial labeling inversion pulse. *J Magn Reson Imaging* 2009;30:678-683
74. Shimada K, Isoda H, Okada T, Kamae T, Maetani Y, Arizono S, et al. Non-contrast-enhanced MR

angiography for selective visualization of the hepatic vein and inferior vena cava with true steady-state free-precession sequence and time-spatial labeling inversion pulses: preliminary results. *J Magn Reson Imaging* 2009;29:474-479

75. Shimada K, Isoda H, Okada T, Maetani Y, Arizono S, Hirokawa Y, et al. Non-contrast-enhanced hepatic MR angiography with true steady-state free-precession and time spatial labeling inversion pulse: optimization of the technique and preliminary results. *Eur J Radiol* 2009;70:111-117
76. van Osch MJ, Hendrikse J, Golay X, Bakker CJ, van der Grond J. Non-invasive visualization of collateral blood flow patterns of the circle of Willis by dynamic MR angiography. *Med Image Anal* 2006;10:59-70
77. Yuan C, Mitsumori LM, Beach KW, Maravilla KR. Carotid atherosclerotic plaque: noninvasive MR characterization and identification of vulnerable lesions. *Radiology* 2001;221:285-299
78. Stemerman DH, Krinsky GA, Lee VS, Johnson G, Yang BM, Rofsky NM. Thoracic aorta: rapid black-blood MR imaging with half-Fourier rapid acquisition with relaxation enhancement with or without electrocardiographic triggering. *Radiology* 1999;213:185-191
79. Song HK, Wright AC, Wolf RL, Wehrli FW. Multislice double inversion pulse sequence for efficient black-blood MRI. *Magn Reson Med* 2002;47:616-620
80. Michaely HJ, Kramer H, Weckbach S, Dietrich O, Reiser MF, Schoenberg SO. Renal T2-weighted turbo-spin-echo imaging with BLADE at 3.0 Tesla: initial experience. *J Magn Reson Imaging* 2008;27:148-153
81. Mihai G, Chung YC, Kariisa M, Raman SV, Simonetti OP, Rajagopalan S. Initial feasibility of a multi-station high resolution three-dimensional dark blood angiography protocol for the assessment of peripheral arterial disease. *J Magn Reson Imaging* 2009;30:785-793
82. Schaefer FK, Schaefer PJ, Altjohann C, Bourne M, Decobelli F, Goyen M, et al. A multicenter, site-independent, blinded study to compare the diagnostic accuracy of contrast-enhanced magnetic resonance angiography using 1.0M gadobutrol (Gadovist) to intraarterial digital subtraction angiography in body arteries. *Eur J Radiol* 2007;61:315-323
83. Hacklander T, Mertens H, Stattaus J, Lurken M, Lerch H, Altenburg A, et al. Evaluation of renovascular hypertension: comparison of functional MRI and contrast-enhanced MRA with a routinely performed renal scintigraphy and DSA. *J Comput Assist Tomogr* 2004;28:823-831
84. Fain SB, King BF, Breen JF, Kruger DG, Riederer SJ. High-spatial-resolution contrast-enhanced MR angiography of the renal arteries: a prospective comparison with digital subtraction angiography. *Radiology* 2001;218:481-490
85. Neubauer AM, Caruthers SD, Hockett FD, Cyrus T, Robertson JD, Allen JS, et al. Fluorine cardiovascular magnetic resonance angiography in vivo at 1.5 T with perfluorocarbon nanoparticle contrast agents. *J Cardiovasc Magn Reson* 2007;9:565-573
86. Sakuma H, Ichikawa Y, Chino S, Hirano T, Makino K, Takeda K. Detection of coronary artery stenosis with whole-heart coronary magnetic resonance angiography. *J Am Coll Cardiol* 2006;48:1946-1950
87. Stafford RB, Sabati M, Haakstad MJ, Mahallati H, Frayne R. Unenhanced MR angiography of the renal arteries with balanced steady-state free precession dixon method. *AJR Am J Roentgenol* 2008;191:243-246
88. Maki JH, Wilson GJ, Eubank WB, Glickerman DJ, Pipavath S, Hoogeveen RM. Steady-state free precession MRA of the renal arteries: breath-hold and navigator-gated techniques vs. CE-MRA. *J Magn Reson Imaging* 2007;26:966-973
89. Crowley JJ, Santos RM, Peter RH, Puma JA, Schwab SJ, Phillips HR, et al. Progression of renal artery stenosis in patients undergoing cardiac catheterization. *Am Heart J* 1998;136:913-918

90. Jou LD, Mawad ME. Timing and size of flow impingement in a giant intracranial aneurysm at the internal carotid artery. *Med Biol Eng Comput* 2011;49:891-899
91. Gemci T, Shortall B, Allen GM, Corcoran TE, Chigier N. A CFD study of the throat during aerosol drug delivery using heliox and air. *Journal of Aerosol Science* 2003;34:1175-1192
92. Behbahani M, Behr M, Hormes M, Steinseifer U, Arora D, Coronado O, et al. A review of computational fluid dynamics analysis of blood pumps. *European Journal of Applied Mathematics* 2009;20:363-397
93. Alexopoulos AH, Karakosta P, Kiparissides C. Particle Transfer and Deposition Using an Integrated CFD Model of the Respiratory System. *20th European Symposium on Computer Aided Process Engineering* 2010;28:211-216
94. Zakaria H, Robertson AM, Kerber CW. A parametric model for studies of flow in arterial bifurcations. *Annals of Biomedical Engineering* 2008;36:1515-1530
95. Versteeg HK, Malalasekera W. *An introduction to computational fluid dynamics: The Finite Volume Method*: Pearson Education Limited, 2007
96. Burleson AC, Strother CM, Turitto VT. Computer Modeling of Intracranial Saccular and Lateral Aneurysms for the Study of Their Hemodynamics. *Neurosurgery* 1995;37:774-782
97. Cebral JR, Castro MA, Appanaboyina S, Putman CM, Millan D, Frangi AF. Efficient pipeline for image-based patient-specific analysis of cerebral aneurysm hemodynamics: Technique and sensitivity. *Ieee Transactions on Medical Imaging* 2005;24:457-467
98. Chien A, Castro MA, Tateshima S, Sayre J, Cebral J, Vinuela F. Quantitative Hemodynamic Analysis of Brain Aneurysms at Different Locations. *American Journal of Neuroradiology* 2009;30:1507-1512
99. Hoi YM, Meng H, Woodward SH, Bendok BR, Hanel RA, Guterman LR, et al. Effects of arterial geometry on aneurysm growth: three-dimensional computational fluid dynamics study. *Journal of Neurosurgery* 2004;101:676-681
100. Steinman DA, Thomas JB, Ladak HM, Milner JS, Rutt BK, Spence JD. Reconstruction of carotid bifurcation hemodynamics and wall thickness using computational fluid dynamics and MRI. *Magnetic Resonance in Medicine* 2002;47:149-159
101. Valencia A, Zarate A, Galvez M, Badilla L. Non-Newtonian blood flow dynamics in a right internal carotid artery with a saccular aneurysm. *International Journal for Numerical Methods in Fluids* 2006;50:751-764
102. Valencia AA, Guzman AM, Finol EA, Amon CH. Blood flow dynamics in saccular aneurysm models of the basilar artery. *Journal of Biomechanical Engineering-Transactions of the Asme* 2006;128:516-526
103. Valencia A, Botto S, Sordo J, Galvez M, Badilla L. Comparison of haemodynamics in cerebral aneurysms of different sizes located in the ophthalmic artery. *International Journal for Numerical Methods in Fluids* 2007;53:793-809
104. Gambaruto AM, Janela J, Moura A, Sequeira A. Sensitivity of Hemodynamics in a Patient Specific Cerebral Aneurysm to Vascular Geometry and Blood Rheology. *Mathematical Biosciences and Engineering* 2011;8:409-423
105. Marzo A, Singh P, Reymond P, Stergiopulos N, Patel U, Hose R. Influence of inlet boundary conditions on the local haemodynamics of intracranial aneurysms. *Computer Methods in Biomechanics and Biomedical Engineering* 2009;12:431-444
106. Liou TM, Chang TW, Chang WC. Pulsatile Flow-through a Bifurcation with a Cerebrovascular Aneurysm. *Journal of Biomechanical Engineering-Transactions of the Asme* 1994;116:112-118
107. Mantha AR, Benndorf G, Hernandez A, Metcalfe RW. Stability of pulsatile blood flow at the ostium

of cerebral aneurysms. *Journal of Biomechanics* 2009;42:1081-1087

108. Leung JH, Wright AR, Cheshire N, Crane J, Thom SA, Hughes AD, et al. Fluid structure interaction of patient specific abdominal aortic aneurysms: a comparison with solid stress models. *Biomedical Engineering Online* 2006;5
109. Hassan T, Ezura M, Timofeev EV, Tominaga T, Saito T, Takahashi A, et al. Computational simulation of therapeutic parent artery occlusion to treat giant vertebrobasilar aneurysm. *American Journal of Neuroradiology* 2004;25:63-68
110. Jou LD, Quick CM, Young WL, Lawton MT, Higashida R, Martin A, et al. Computational approach to quantifying hemodynamic forces in giant cerebral aneurysms. *American Journal of Neuroradiology* 2003;24:1804-1810
111. Rayz VL, Boussel L, Lawton MT, Acevedo-Bolton G, Ge L, Young WL, et al. Numerical modeling of the flow in intracranial aneurysms: Prediction of regions prone to thrombus formation. *Annals of Biomedical Engineering* 2008;36:1793-1804
112. Shojima M, Oshima M, Takagi K, Torii R, Nagata K, Shirouzu I, et al. Role of the bloodstream impacting force and the local pressure elevation in the rupture of cerebral aneurysms. *Stroke* 2005;36:1933-1938
113. Shojima M, Oshima M, Takagi K, Torii R, Hayakawa M, Katada K, et al. Magnitude and role of wall shear stress on cerebral aneurysm - Computational fluid dynamic study of 20 middle cerebral artery aneurysms. *Stroke* 2004;35:2500-2505
114. Mantha A, Karmonik C, Benndorf G, Strother C, Metcalfe R. Hemodynamics in a cerebral artery before and after the formation of an aneurysm. *American Journal of Neuroradiology* 2006;27:1113-1118
115. Venugopal P, Valentino D, Schmitt H, Villablanca JP, Vinuela F, Duckwiler G. Sensitivity of patient-specific numerical simulation of cerebal aneurysm hemodynamics to inflow boundary conditions. *Journal of Neurosurgery* 2007;106:1051-1060
116. Vignon-Clementel IE, Figueroa CA, Jansen KE, Taylor CA. Outflow boundary conditions for three-dimensional finite element modeling of blood flow and pressure in arteries. *Computer Methods in Applied Mechanics and Engineering* 2006;195:3776-3796
117. Morris L, Delassus P, Callanan A, Walsh M, Wallis F, Grace P, et al. 3-D numerical simulation of blood flow through models of the human aorta. *Journal of Biomechanical Engineering-Transactions of the Asme* 2005;127:767-775
118. Myers JG, Moore JA, Ojha M, Johnston KW, Ethier CR. Factors influencing blood flow patterns in the human right coronary artery. *Annals of Biomedical Engineering* 2001;29:109-120
119. Oshima M, Sakai H, Torii R. Modelling of inflow boundary conditions for image-based simulation of cerebrovascular flow. *International Journal for Numerical Methods in Fluids* 2005;47:603-617
120. Moyle KR, Antiga L, Steinman DA. Inlet conditions for image-based CFD models of the carotid bifurcation: Is it reasonable to assume fully developed flow? *Journal of Biomechanical Engineering-Transactions of the Asme* 2006;128:371-379
121. Karmonik C, Yen C, Diaz O, Klucznik R, Grossman RG, Benndorf G. Temporal variations of wall shear stress parameters in intracranial aneurysms-importance of patient-specific inflow waveforms for CFD calculations. *Acta Neurochirurgica* 2010;152:1391-1398
122. Torii R, Oshima M, Kobayashi T, Takagi K, Tezduyar TE. Computer modeling of cardiovascular fluid-structure interactions with the deforming-spatial-domain/stabilized space-time formulation. *Computer Methods in Applied Mechanics and Engineering* 2006;195:1885-1895
123. Baek H, Jayaraman MV, Karniadakis GE. Wall shear stress and pressure distribution on aneurysms

and infundibulae in the posterior communicating artery bifurcation. *Ann Biomed Eng* 2009;37:2469-2487

124. Mut F, Lohner R, Chien A, Tateshima S, Vinuela F, Putman C, et al. Computational Hemodynamics Framework for the Analysis of Cerebral Aneurysms. *Int j numer method biomed eng* 2011;27:822-839
125. Radaellia AG, Augsburger L, Cebral JR, Ohta M, Rufenacht DA, Balossino R, et al. Reproducibility of haemodynamical simulations in a subject-specific stented aneurysm model - A report on the Virtual Intracranial Stenting Challenge 2007. *Journal of Biomechanics* 2008;41:2069-2081
126. Karmonik C, Klucznik R, Benndorf G. Comparison of velocity patterns in an AComA aneurysm measured with 2D phase contrast MRI and simulated with CFD. *Technol Health Care* 2008;16:119-128
127. Chien A, Tateshima S, Castro M, Sayre J, Cebral J, Vinuela F. Patient-specific flow analysis of brain aneurysms at a single location: comparison of hemodynamic characteristics in small aneurysms. *Medical & Biological Engineering & Computing* 2008;46:1113-1120
128. Castro MA, Putman CM, Cebral JR. Computational fluid dynamics modeling of intracranial aneurysms: effects of parent artery segmentation on intra-aneurysmal hemodynamics. *AJNR Am J Neuroradiol* 2006;27:1703-1709
129. Steinman DA, Milner JS, Norley CJ, Lownie SP, Holdsworth DW. Image-based computational simulation of flow dynamics in a giant intracranial aneurysm. *American Journal of Neuroradiology* 2003;24:559-566
130. Zhang W, Qian Y, Lin J, Lv P, Karunanithi K, Zeng M. Hemodynamic analysis of renal artery stenosis using computational fluid dynamics technology based on unenhanced steady-state free precession magnetic resonance angiography: preliminary results. *Int J Cardiovasc Imaging* 2014;30:367-375
131. Ford MD, Stuhne GR, Nikolov HN, Habets DF, Lownie SP, Holdsworth DW, et al. Virtual angiography for visualization and validation of computational models of aneurysm hemodynamics. *Ieee Transactions on Medical Imaging* 2005;24:1586-1592
132. Acevedo-Bolton G, Jou LD, Dispensa BP, Lawton MT, Higashida RT, Martin AJ, et al. Estimating the hemodynamic impact of interventional treatments of aneurysms: numerical simulation with experimental validation: technical case report. *Neurosurgery* 2006;59:E429-430; author reply E429-430
133. Ford MD, Nikolov HN, Milner JS, Lownie SP, Demont EM, Kalata W, et al. PIV-measured versus CFD-predicted flow dynamics in anatomically realistic cerebral aneurysm models. *J Biomech Eng* 2008;130:021015
134. Yim PJ, Cebral JR, Weaver A, Lutz RJ, Soto O, Vasbinder GB, et al. Estimation of the differential pressure at renal artery stenoses. *Magn Reson Med* 2004;51:969-977
135. Imai Y, Sato K, Ishikawa T, Yamaguchi T. Inflow into saccular cerebral aneurysms at arterial bends. *Annals of Biomedical Engineering* 2008;36:1489-1495
136. Maier SE, Scheidegger MB, Liu K, Schneider E, Bollinger A, Boesiger P. Renal artery velocity mapping with MR imaging. *J Magn Reson Imaging* 1995;5:669-676
137. Yamamoto T, Ogasawara Y, Kimura A, Tanaka H, Hiramatsu O, Tsujioka K, et al. Blood velocity profiles in the human renal artery by Doppler ultrasound and their relationship to atherosclerosis. *Arterioscler Thromb Vasc Biol* 1996;16:172-177
138. Konoura C, Yagi T, Nakamura M, Iwasaki K, Qian Y, Okuda S, et al. Numerical analysis of blood flow distribution in 4- and 3-branch vascular grafts. *J Artif Organs* 2013
139. White CJ. Management of renal artery stenosis: the case for intervention, defending current

guidelines, and screening (drive-by) renal angiography at the time of catheterization. *Prog Cardiovasc Dis* 2009;52:229-237

140. Hirsch AT, Haskal ZJ, Hertzer NR, Bakal CW, Creager MA, Halperin JL, et al. ACC/AHA 2005 guidelines for the management of patients with peripheral arterial disease (lower extremity, renal, mesenteric, and abdominal aortic): executive summary a collaborative report from the American Association for Vascular Surgery/Society for Vascular Surgery, Society for Cardiovascular Angiography and Interventions, Society for Vascular Medicine and Biology, Society of Interventional Radiology, and the ACC/AHA Task Force on Practice Guidelines (Writing Committee to Develop Guidelines for the Management of Patients With Peripheral Arterial Disease) endorsed by the American Association of Cardiovascular and Pulmonary Rehabilitation; National Heart, Lung, and Blood Institute; Society for Vascular Nursing; TransAtlantic Inter-Society Consensus; and Vascular Disease Foundation. *J Am Coll Cardiol* 2006;47:1239-1312
141. Textor SC, Lerman L, McKusick M. The uncertain value of renal artery interventions: where are we now? *JACC Cardiovasc Interv* 2009;2:175-182
142. Piccinelli M, Vergara C, Antiga L, Forzenigo L, Biondetti P, Domanin M. Impact of hemodynamics on lumen boundary displacements in abdominal aortic aneurysms by means of dynamic computed tomography and computational fluid dynamics. *Biomech Model Mechanobiol* 2013;12:1263-1276
143. Leesar MA, Varma J, Shapira A, Fahsah I, Raza ST, Elghoul Z, et al. Prediction of hypertension improvement after stenting of renal artery stenosis: comparative accuracy of translesional pressure gradients, intravascular ultrasound, and angiography. *J Am Coll Cardiol* 2009;53:2363-2371
144. Katritsis D, Kaiktsis L, Chaniotis A, Pantos J, Efstathopoulos EP, Marmarelis V. Wall shear stress: Theoretical considerations and methods of measurement. *Progress in Cardiovascular Diseases* 2007;49:307-329
145. Penn DL, Komotar RJ, Sander Connolly E. Hemodynamic mechanisms underlying cerebral aneurysm pathogenesis. *J Clin Neurosci* 2011;18:1435-1438
146. Milnor WR. *Hemodynamics*. Baltimore, London: Williams & Wilkins, 1982
147. Kamiya A, Ando J, Shibata M, Masuda H. Roles of fluid shear stress in physiological regulation of vascular structure and function. *Biorheology* 1988;25:271-278
148. Sforza DM, Putman CM, Cebral JR. Hemodynamics of Cerebral Aneurysms. *Annu Rev Fluid Mech* 2009;41:91-107
149. Guzman RJ, Abe K, Zarins CK. Flow-induced arterial enlargement is inhibited by suppression of nitric oxide synthase activity in vivo. *Surgery* 1997;122:273-279
150. Chatziprodromou I, Tricoli A, Poulikakos D, Ventikos Y. Haemodynamics and wall remodelling of a growing cerebral aneurysm: a computational model. *J Biomech* 2007;40:412-426
151. Sonesson B, Hansen F, Lanne T. Abdominal aortic aneurysm: a general defect in the vasculature with focal manifestations in the abdominal aorta? *J Vasc Surg* 1997;26:247-254
152. Griffith TM. Modulation of Blood-Flow and Tissue Perfusion by Endothelium-Derived Relaxing Factor. *Experimental Physiology* 1994;79:873-913
153. Crompton MR. Mechanism of growth and rupture in cerebral berry aneurysms. *Br Med J* 1966;1:1138-1142
154. Ujiie H, Tachibana H, Hiramatsu O, Hazel AL, Matsumoto T, Ogasawara Y, et al. Effects of size and shape (aspect ratio) on the hemodynamics of saccular aneurysms: A possible index for surgical treatment of intracranial aneurysms. *Neurosurgery* 1999;45:119-129
155. Zuleger DI, Poulikakos D, Valavanis A, Kollias SS. Combining magnetic resonance measurements with numerical simulations - Extracting blood flow physiology information relevant to the

investigation of intracranial aneurysms in the circle of Willis. *International Journal of Heat and Fluid Flow* 2010;31:1032-1039

156. Sforza DM, Putman CM, Scrivano E, Lylyk P, Cebral JR. Blood-flow characteristics in a terminal basilar tip aneurysm prior to its fatal rupture. *AJNR Am J Neuroradiol* 2010;31:1127-1131
157. Feng YX, Wada S, Tsubota K, Yamaguchi T. Growth of intracranial aneurysms arised from curved vessels under the influence of elevated wall shear stress - A computer simulation study. *Jsme International Journal Series C-Mechanical Systems Machine Elements and Manufacturing* 2004;47:1035-1042
158. Lu G, Huang L, Zhang XL, Wang SZ, Hong Y, Hu Z, et al. Influence of Hemodynamic Factors on Rupture of Intracranial Aneurysms: Patient-Specific 3D Mirror Aneurysms Model Computational Fluid Dynamics Simulation. *American Journal of Neuroradiology* 2011;32:1255-1261
159. Jou LD, Lee DH, Morsi H, Mawad ME. Wall Shear Stress on Ruptured and Unruptured Intracranial Aneurysms at the Internal Carotid Artery. *American Journal of Neuroradiology* 2008;29:1761-1767
160. Boussel L, Rayz V, McCulloch C, Martin A, Acevedo-Bolton G, Lawton M, et al. Aneurysm Growth Occurs at Region of Low Wall Shear Stress Patient-Specific Correlation of Hemodynamics and Growth in a Longitudinal Study. *Stroke* 2008;39:2997-3002
161. Malek AM, Alper SL, Izumo S. Hemodynamic shear stress and its role in atherosclerosis. *JAMA* 1999;282:2035-2042
162. Kaatee R, Beek FJ, Verschuyl EJ, vd Ven PJ, Beutler JJ, van Schaik JP, et al. Atherosclerotic renal artery stenosis: ostial or truncal? *Radiology* 1996;199:637-640
163. Dean RH, Kieffer RW, Smith BM, Oates JA, Nadeau JH, Hollifield JW, et al. Renovascular hypertension: anatomic and renal function changes during drug therapy. *Arch Surg* 1981;116:1408-1415
164. Tollefson DF, Ernst CB. Natural history of atherosclerotic renal artery stenosis associated with aortic disease. *J Vasc Surg* 1991;14:327-331
165. Wollenweber J, Sheps SG, Davis GD. Clinical course of atherosclerotic renovascular disease. *Am J Cardiol* 1968;21:60-71
166. Harding MB, Smith LR, Himmelstein SI, Harrison K, Phillips HR, Schwab SJ, et al. Renal artery stenosis: prevalence and associated risk factors in patients undergoing routine cardiac catheterization. *J Am Soc Nephrol* 1992;2:1608-1616
167. Grenier N, Hauger O, Cimpean A, Perot V. Update of renal imaging. *Semin Nucl Med* 2006;36:3-15
168. Henke PK, Cardneau JD, Welling TH, 3rd, Upchurch GR, Jr., Wakefield TW, Jacobs LA, et al. Renal artery aneurysms: a 35-year clinical experience with 252 aneurysms in 168 patients. *Ann Surg* 2001;234:454-462; discussion 462-453
169. Nosher JL, Chung J, Brevetti LS, Graham AM, Siegel RL. Visceral and renal artery aneurysms: a pictorial essay on endovascular therapy. *Radiographics* 2006;26:1687-1704; quiz 1687